DOT/FAA/AR-03/74
Office of Aviation Research
Washington, D.C. 20591

Bonded Repair of Aircraft Composite Sandwich Structures

February 2004

Final Report

U.S. Department of Transportation
Federal Aviation Administration

NOTICE

Technical Report Documentation Page

1. Report No.
DOT/FAA/AR-03/74

2. Government Accession No.

3. Recipient's Catalog No.

4. Title and Subtitle
BONDED REPAIR OF AIRCRAFT COMPOSITE SANDWICH STRUCTURES

5. Report Date
February 2004

6. Performing Organization Code

7. Author(s)
John S. Tomblin[1], Lamia Salah[1], John M. Welch[2], and Michael D. Borgman[2]

8. Performing Organization Report No.

9. Performing Organization Name and Address
[1] National Institute for Aviation Research
Wichita State University
1845 Fairmount
Wichita, KS 67260-0093

[2] The Boeing Company
Wichita Commercial Division
Wichita, KS 67277

10. Work Unit No. (TRAIS)

11. Contract or Grant No.

12. Sponsoring Agency Name and Address
U.S. Department of Transportation
Federal Aviation Administration
Office of Aviation Research
Washington, DC 20591

13. Type of Report and Period Covered
Final Report

14. Sponsoring Agency Code
ANM-120

15. Supplementary Notes
The Technical Monitor for the FAA William J. Hughes Technical Center was Mr. Peter Shyprykevich.

16. Abstract

With the increasing use of fiber-reinforced composite sandwich structures in aircraft components, it has become necessary to develop repair methods that will restore the component's original design strength without compromising its structural integrity. One of the main concerns is whether large repairs are always necessary to restore strength or whether smaller, less intrusive repairs can be implemented instead. Cure temperature can also become an issue if the repair patch requires curing at 350°F. Residual thermal stresses due to the bonding of the patch to the parent structure may induce further damage to the component. With these concerns in mind, the main objective of this study was to evaluate the effectiveness of scarf repairs applied to sandwich structures, given several bonding repair variables. The overall program was divided into three tasks. The first task investigated the performance of different airline depots in repairing picture frame shear elements using two different repair methods: SAE's Commercial Aircraft Composite Repair Committee-developed wet lay-up procedure and a Boeing, i.e., original equipment manufacturer, prepreg procedure. Each method had different cure temperatures and used different materials. The second task performed in this investigation examined the effect of different repair variables on repair performance. The variables considered included three different scarf overlaps and two different core cell sizes (1/8 and 3/8 inch) and impact damage inflicted on the repair. The third task provided a comparison between several existing analytical models and available experimental results. This report summarizes the experimental and analytical results of the investigation, addresses the limitations of the experimental and analytical efforts, and provides recommendations for future research.

17. Key Words
Composite materials, Repair, Sandwich structures, Damage

18. Distribution Statement
This document is available to the public through the National Technical Information Service (NTIS), Springfield, Virginia 22161.

19. Security Classif. (of this report)
Unclassified

20. Security Classif. (of this page)
Unclassified

21. No. of Pages
121

22. Price

Form DOT F1700.7 (8-72)

Reproduction of completed page authorized

TABLE OF CONTENTS

LIST OF FIGURES

LIST OF TABLES

EXECUTIVE SUMMARY

With the increasing use of fiber-reinforced composite sandwich structures in aircraft components, it has become necessary to develop repair methods that will restore the component's original design strength without compromising its structural integrity. One of the main concerns is whether large repairs are always necessary to restore strength or whether smaller, less intrusive repairs can be implemented instead. Cure temperature can also become an issue if the repair patch requires curing at 350°F. Residual thermal stresses due to the bonding of the patch to the parent structure may induce further damage to the component. With these concerns in mind, the main objective of this study was to evaluate the effectiveness of scarf repairs applied to sandwich structures, given several bonding repair variables. The overall program was divided into three major tasks.

The first task investigated the performance of different airline repair depots in repairing picture frame shear elements using two different repair methods: SAE's Commercial Aircraft Composite Repair Committee (CACRC) developed wet lay-up procedure and a Boeing, i.e., original equipment manufacturer (OEM), prepreg procedure. Each method had different cure temperatures and used different materials. Furthermore, the wet lay-up method required an extra ply while the OEM method did not. Another difference between the two methods involved the scarf overlap: the wet lay-up method used the conventional 0.5-inch scarf overlap, while the OEM method used a steeper 0.25-inch scarf overlap. All the repaired coupons achieved at least 92% of the average pristine strength regardless of the repair method, except those coupons from one airline repair depot that appeared to have been poorly bonded.

A nondestructive inspection was also performed as part of this task to compare the capabilities of different methods used in the field to detect flaws. Five inspection methods were used: a manual tap test using the Airbus tap hammer, an automated tap test using the Mitsui Woodpecker device, a mechanical impedance analysis using the V-95 device, a low-frequency bond test using the MAUS C-Scan device, and a through-transmission ultrasonic inspection using the Ultrapac system. All the methods available for the four lay-up configurations considerably underpredicted the size of the damage, with the airbus tap hammer being the most inaccurate. According to this study, the mechanical impedance analysis method, capable of detecting 88 percent of the actual size for the thinnest laminate and 64 percent for the thickest laminate, yielded the best estimates.

The second task examined the effect of different repair variables on repair performance. The variables considered included three different scarf overlaps and two different core cell sizes (1/8 and 3/8 inch) and impact damage inflicted on the repair. An experimental test program was performed using various coupon geometries and loading modes. The results were used in conducting comparisons with various publicly available analytical models for analyzing composite repairs.

The third task consisted of comparing several publicly available analytical models and comparing the data generated with the experimental results. Models were chosen as a function of the failure modes of the coupons. Laminate models were used for coupons that failed in the

repair or parent facesheets. Adhesive models were used for coupons that failed in the adhesive bondline.

This project demonstrated the influence of several factors on the performance of sandwich structure repairs. The most prominent conclusion that could be deduced from this study was the major impact that core properties, more specifically the core cell size, have on the performance of a sandwich structure with the same parent and repair materials. The results showed a superior strain and strength capacity of the 1/8-inch core coupons compared to the 3/8-inch core coupons, regardless of the repair size. The 1/8-inch core coupons offered a larger bond interface area than the 3/8-inch core coupons and, therefore, a higher strain capacity, assuming the same facesheet materials were used.

The research performed as part of this investigation validates the use of the CACRC repair procedures that are documented in numerous SAE publications and establishes the optimum scarf length for repair of facesheets of composite sandwich structures.

1. INTRODUCTION.

1.1 PURPOSE.

With the increasing use of composite sandwich structures in aircraft components, it is crucial to develop repair methods that restore the original strength of the part without compromising its structural integrity. In bonded repairs, the repair plies are overlapped to evenly distribute the load from the present structure to the repair patch. In the repair shown in figure 1, the ply overlap shown is 0.25 in. One of the main concerns when repairing a structural part is the size of the repair. For example, using a 0.50-inch overlap causes the repair to become so large that it can cause additional deterioration to the part while trying to restore its original structural capacity. Therefore, the purpose of this research was to investigate the effectiveness of scarf repairs applied to sandwich structures, as shown in figure 1, given several bonded repair variables.

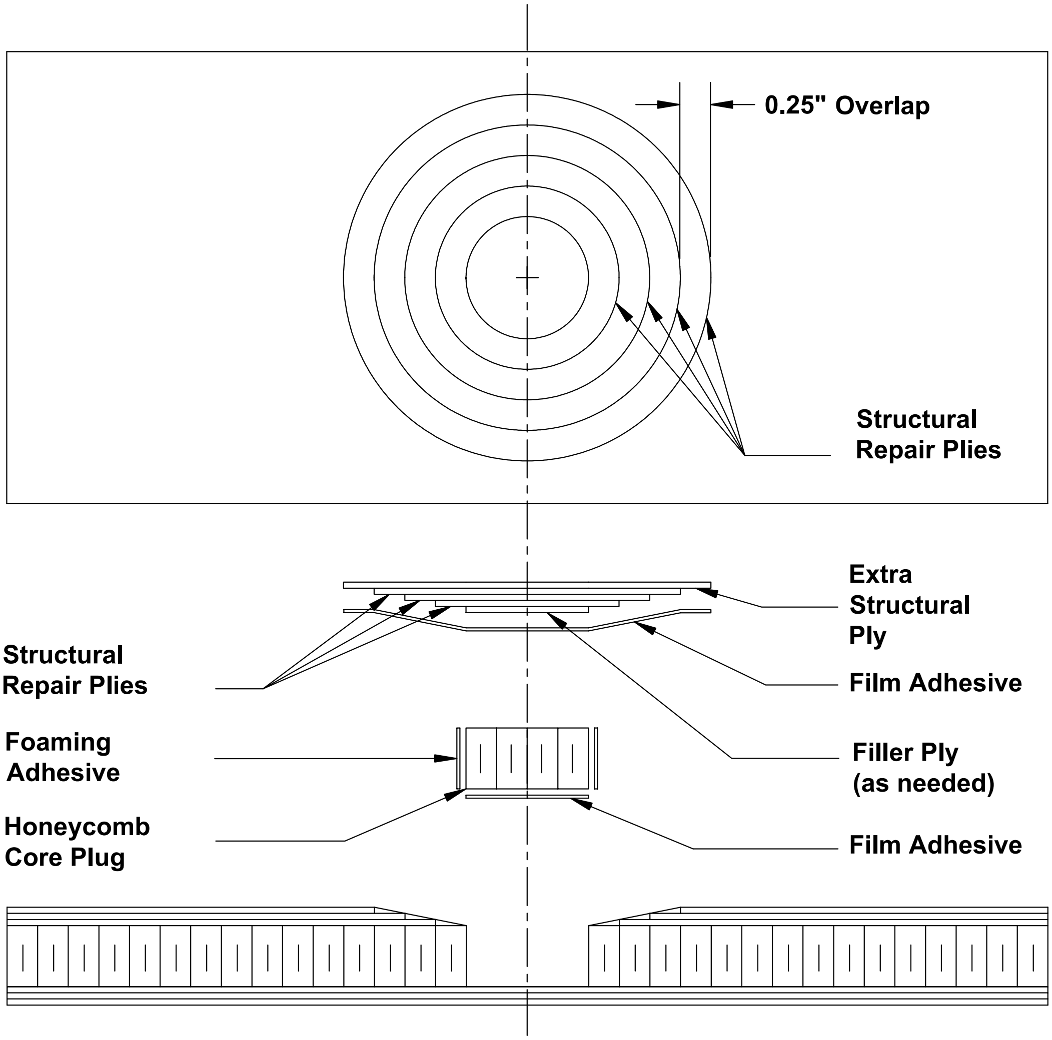

FIGURE 1. SCHEMATIC OF A SCARF REPAIR APPLIED TO A SANDWICH COMPONENT

This project was subdivided into three main tasks:

- Repair Procedures: To evaluate performance of the Commercial Aircraft Composite Repair Committee (CACRC) and the Original Equipment Manufacturer (OEM) methods of repair, i.e., the repair procedures of The Boeing Company versus field station repairs. The ancillary objective was to evaluate the capabilities of the different nondestructive inspection (NDI) field methods used to detect flaws.

- Repair Variable Investigation: To investigate the effects of different variables on the performance of the repair. These variables included different repair configurations, scarf overlaps, core cell sizes, repair materials, cure temperatures, and impact damage.

- Repair Analysis Capability: To perform a detailed literature review of all the available scarf repair analytical models and to evaluate some of the analytical methods using static data generated from the mechanical tests.

This report summarizes the experimental and analytical efforts undertaken for the completion of this project.

1.2 BACKGROUND.

The use of composite materials in aircraft structural components has increased in the past few decades as a result of the many advantages they offer compared to metals. Composite airframe structures, unlike traditional metal structures, have high strength and stiffness to weight ratios, have a good fatigue resistance, and are less prone to deterioration caused by corrosion and cracking. Nevertheless, they are more sensitive to other types of damage, mainly impact damage that can cause disbonding, delamination, and internal crushing. Therefore, to improve the performance of composite aircraft structures in the long run and take advantage of their many benefits, one should first ensure that these structures are durable, repairable, and maintainable [1].

Composite structures are primarily damaged by lightning strikes, tool drops, service vehicle collisions, hail, runway debris, and birds. Other sources of damage include erosion, abrasion, manufacturing defects, excess heat exposure, and fluid infiltration. Therefore, the extent of the damage determines whether the component needs to be repaired or replaced. In most cases, replacing the entire part is not economically feasible; thus, repairing it is the only viable solution. Furthermore, since the time constraint is an issue, repairs must be performed as quickly as possible so that the aircraft can be returned to service as soon as possible.

When designing a composite repair, several factors must be considered to ensure the repair's effectiveness and structural integrity. These factors include stiffness, strength, stability, operating temperature, durability, and aerodynamic smoothness [2].

The stiffness of the repair should match, as close as possible, the stiffness of the parent structure. A repair that is stiffer than the parent structure would attract more load to the repaired region, possibly causing it to exceed its allowable strength. On the other hand, a repair with a lower stiffness than the parent structure would divert the load from the repair, possibly causing it to overstress the parent structure.

When considering the strength of a composite repair, one should try to match the strength and stiffness of the parent structure. However, this is not always possible unless the same materials and processes are used. In most cases, a different repair material is used. Therefore, while ensuring that the stiffnesses are matched, a positive strength margin of safety should be achieved [2].

The operating temperature of the repaired region should be one of the determining factors in the repair material selection: the repair operating temperature should not exceed the maximum operating temperature of the resin system.

Another major factor in repair design is durability. The repair should be permanent, i.e., lasting the lifetime of the aircraft. In this case, if the repair material is different from the parent material, it should at least have the same operational environment capabilities [2].

Nevertheless, the most crucial element in designing a repair is the adhesive joint: one should ensure that the adhesive does not become the weak link and that joint failure occurs as a result of bulk failure of the adherends [3]. The joint should always be designed so that its strength exceeds the strength of the parent structure by at least 50%. This margin of safety accounts for the damage susceptibility of the adhesive.

Adhesively bonded joints can be strong in shear but weak in peel; therefore, the repair design should aim to maintain the adhesive in a state of shear or compression and to minimize any direct or induced peel stresses [4]. In bonded joints, loads are transferred mainly by shear on the surfaces of the elements.

Joints are classified into two main categories: single-load paths and multiple-load paths. Failure in single-load path joints would result in a catastrophic loss of structural capability, whereas failure in multiple-load path joints would result in the load being redistributed and carried by other components. The most common joint types used in the aircraft industry are the following: double lap, single lap, scarf, and stepped lap, all of which have different characteristics and capabilities.

Single lap joints have the lowest strength joint capability due to the eccentricity of the load path that induces bending of the adherends and a significant increase in peel stresses causing premature failure.

Double lap joints have lower peel stresses due to the reduction of the load path eccentricity and thus have a higher strain capacity compared to single lap joints.

Scarf joints, with virtually no eccentricity of the load and minimal peel stresses, are the most efficient joints [3] for the following reasons: They are very effective in restoring the original strength of the composite structure, and they preserve the structure's clearance and aerodynamic smoothness. Nevertheless, scarf joints require the removal of large amounts of undamaged material to preserve a shallow scarf angle, which may cause further damage to the parent laminate and thereby can compromise its structural integrity.

2. REPAIR PROCEDURES.

2.1 PURPOSE.

The purpose of the repair procedure investigation was to evaluate the performance of the OEM versus field station repairs using shear elements representative of structures used in commercial airplanes.

2.2 ELEMENT CONFIGURATION.

All specimens used in this investigation were picture frame shear elements manufactured by the OEM, as shown in figure 2.

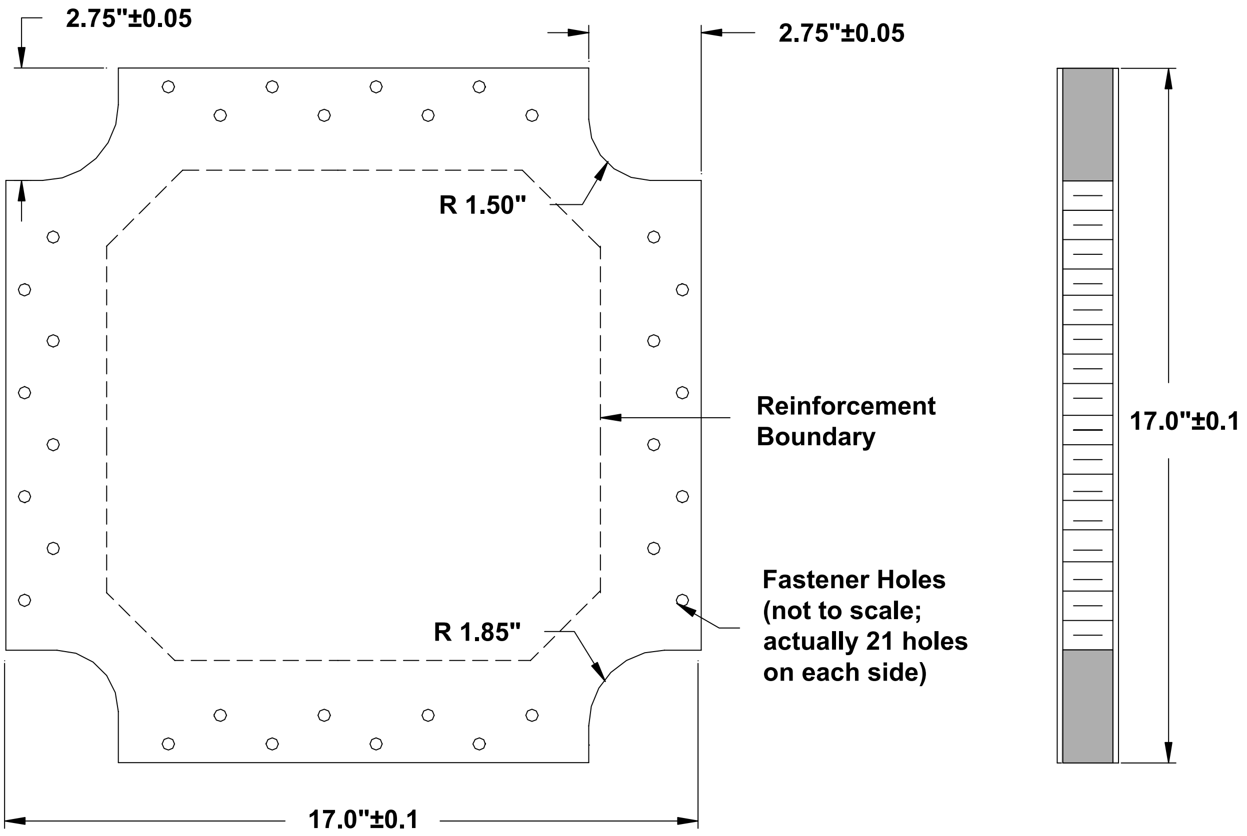

FIGURE 2. SCHEMATIC OF A PICTURE FRAME SHEAR ELEMENT

These picture frame shear elements were sandwich plates comprised of three-ply graphite epoxy facesheets, bonded to a 3/8-inch cell honeycomb core using film adhesive. The lay-up schedule for the facesheets was (45,0/90,0/90) for the tool side and (0/90,0/90,45) for the bag side. A total of 84 mounting holes was drilled in the panels prior to testing. The perforated picture frame shear elements were mounted on a steel fixture with 1/4-inch-diameter fasteners to transfer the load to the coupons. To avoid core or skin crushing, all four edges were reinforced using synspand, a foaming adhesive, through the thickness of the core and nine extra plies in the facesheets. The boundary of the reinforced region is shown in figure 2.

2.3 TEST MATRIX.

The OEM supplied a total of 51 picture frame shear elements. Table 1 shows the different element damage and repair configurations considered and the corresponding number of picture frame shear elements for each configuration.

TABLE 1. COMMERCIAL AIRCRAFT COMPOSITE REPAIR COMMITTEE REPAIR TEST MATRIX

Shear Element Configuration	Repair Station	Number of Elements
Undamaged	N/A	3
Damaged (Barely Visible Impact Damage)	N/A	3
Damaged (4-inch-diameter center hole)	N/A	3
OEM Prepreg Repairs, 350°F Cure T300/934 3K-70-PW Prepreg With FM 377S Adhesive	Boeing	3
OEM Wet Lay-Up Repairs, 250°F Cure	Boeing	6
OEM Prepreg Repair 2250°F Cure Loctite EA9396-C2 Prepreg With EA9696 Adhesive	Boeing	3
OEM Prepreg Repair 3250°F Cure Fibercote E765 Prepreg With SIA 895-2 Adhesive	Boeing	3
Boeing Proprietary	Boeing	3
CACRC Wet Lay-Up Repairs, 250°F Cure Tenex Fibers/Epocast 52A/B	4 Airline Depots	12
OEM Prepreg Repairs, 350°F Cure T300/934 3K-70-PW Prepreg With FM 377S Adhesive	4 Airline Depots	12

As shown, a total of 24 picture frame shear elements was sent to four different airline depots. Each airline received six picture frame shear elements: an undamaged element and five other elements damaged with five different energy levels. These elements were to be inspected and subsequently repaired.

2.4 IMPACT TESTING.

Twenty-five picture frame shear elements supplied by the OEM were impacted using five different energy levels with increasing intensities.

2.4.1 Experimental Setup.

As shown in figure 3 [5], a custom-made drop tower was used to impact the picture frame shear elements. Impact loads were measured using a piezoelectric load cell with a capacity of up to 10,000 lbf. Details of the impact events were recorded using a high-speed data acquisition system. The following is a description of the main components of the impact test apparatus.

- Two support columns that hold the top crosshead and the base platen.
- Two cylindrical shafts that guide the impactor assembly as it drops.
- A base platen where the impact fixtures and sensors are mounted.
- Several test fixtures to constrain the specimen during the impact event.
- Two main impactor assemblies: a low-mass assembly and a high-mass assembly to accommodate weights ranging between 4.5 and 50 lbf, which can be adjusted depending on the energy level to be achieved.
- A pneumatic apparatus that catches the impactor assembly as soon as it hits the specimen.

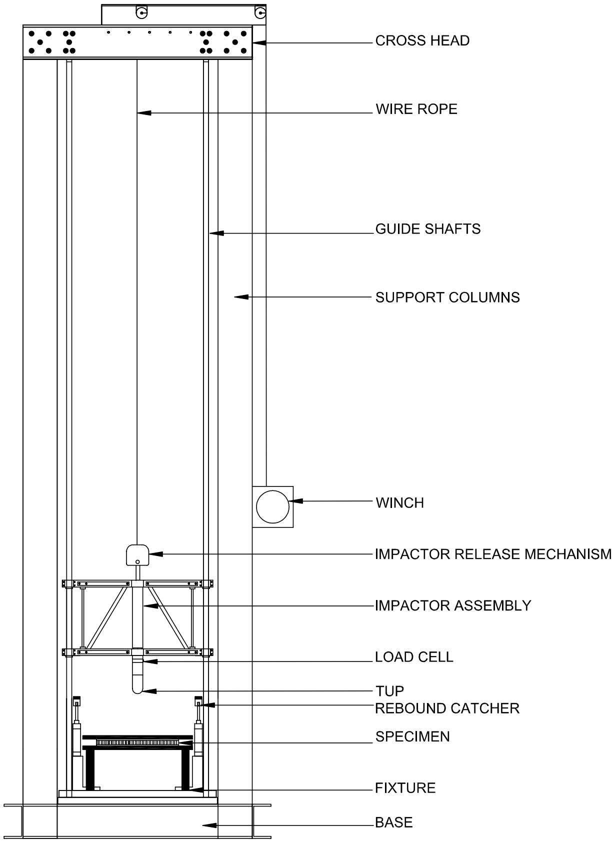

FIGURE 3. IMPACTOR ASSEMBLY

A high-speed data acquisition system was used to record the force-time history of the impact test. The raw data were stored in a text file and consisted of impactor velocity flag voltage and corresponding force. The reduced data contained details of the impact test, including time histories of impact force, impactor velocity, and displacement and impact energy.

2.4.2 Procedure.

Twenty picture frame shear elements were impacted using five different energy levels that generated damage states varying from barely visible to severe. All impact tests were inflicted at the geometric center of the shear elements, using a 3-inch-diameter steel impactor, as shown in figure 4.

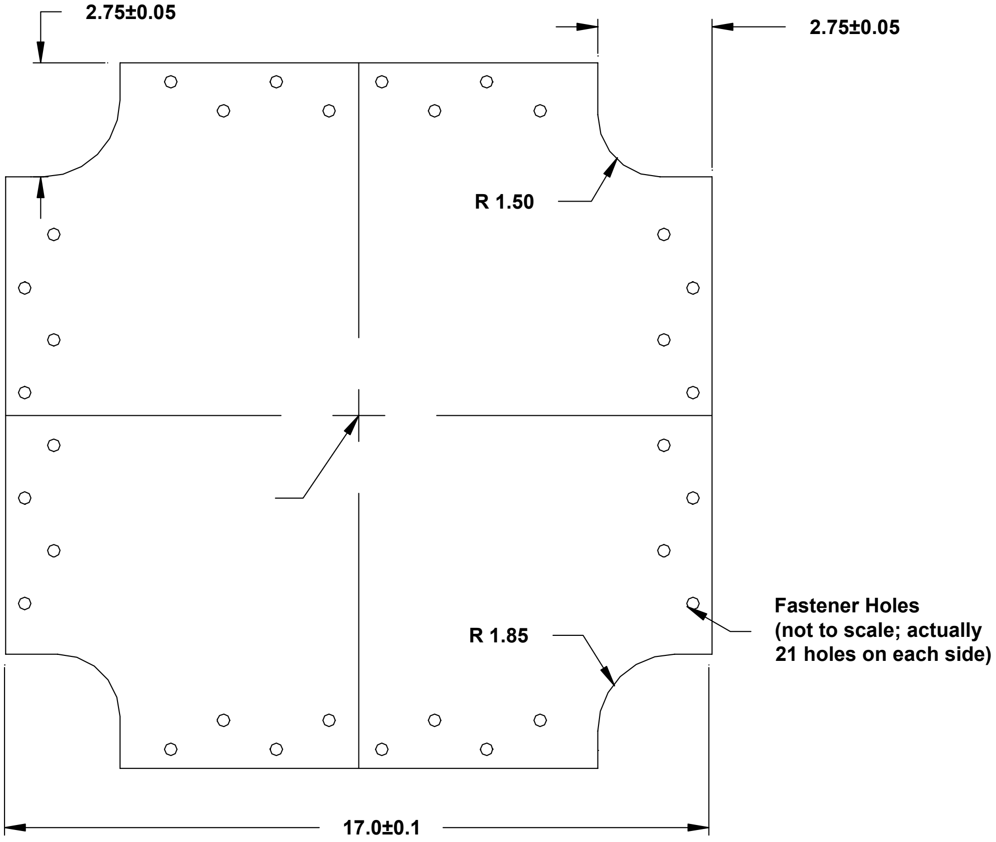

FIGURE 4. IMPACT LOCATION FOR PICTURE FRAME SHEAR ELEMENTS

Elements were clamped along two parallel edges during impact testing. Force and velocity flag voltage data were recorded and subsequently reduced to obtain the impactor velocity and force, impactor displacement, and energy as a function of time. Measured energy and velocity are usually less than target values because of friction losses that occur during impact events. This is shown in figure 5 [5].

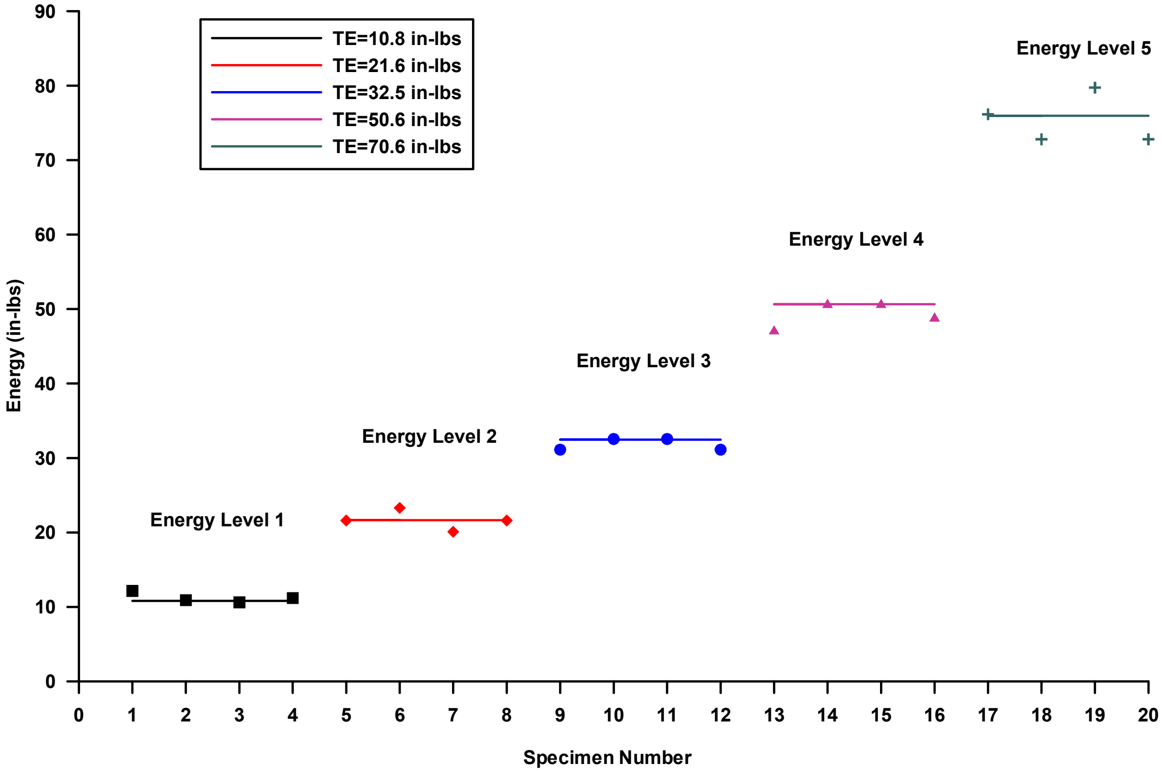

FIGURE 5. COMPARISON BETWEEN TARGET ENERGY LEVELS AND ACTUAL ENERGIES OBTAINED FOR EACH SPECIMEN IMPACTED

2.5 NONDESTRUCTIVE INSPECTION.

The impacted shear elements were subjected to an NDI inspection using different methods with varying levels of accuracy to determine the extent of damage caused by the impacts.

2.5.1 Purpose.

The purpose of this task was to evaluate the accuracy of different NDI methods used in the field to detect flaws in sandwich structures. Twenty picture frame shear elements were impacted with various energy levels to generate damage states ranging from Barely Visible Impact Damage (BVID) to severe. The intent was to evaluate the extent of damage that could realistically be detected in the field. Thus, the coupons that were sent to the various airline repair stations were randomized prior to being sent; each airline repair station had coupons with five different energy levels.

2.5.2 Nondestructive Inspection Methods.

Five different NDI methods were used to inspect the coupons and quantify the damage after impact. The first inspection method was performed at Wichita State University, while the remaining four were performed at the Sandia National Laboratories, Albuquerque, New Mexico. Reference standards were manufactured per SAE International Aerospace Repair Procedure 5606 in order to calibrate the different NDI instruments. These standards contained several embedded flaws of known diameters. These flawed areas consisted of pillow inserts, a machined core, a potted core, and a core splice using a foaming adhesive, as shown in figure 6.

- Pillow inserts were used to simulate interply delaminations. These inserts were made out of four plies of thick tissue paper held together with two layers of heat-resistant polyamide film tape.

- Machined core areas were used to replicate skin-to-honeycomb disbonds. A router was used to produce a flat-bottomed, 1-inch-diameter hole with a depth of 0.25 inch.

- Potted core areas were used to produce areas with lower attenuation than unflawed regions.

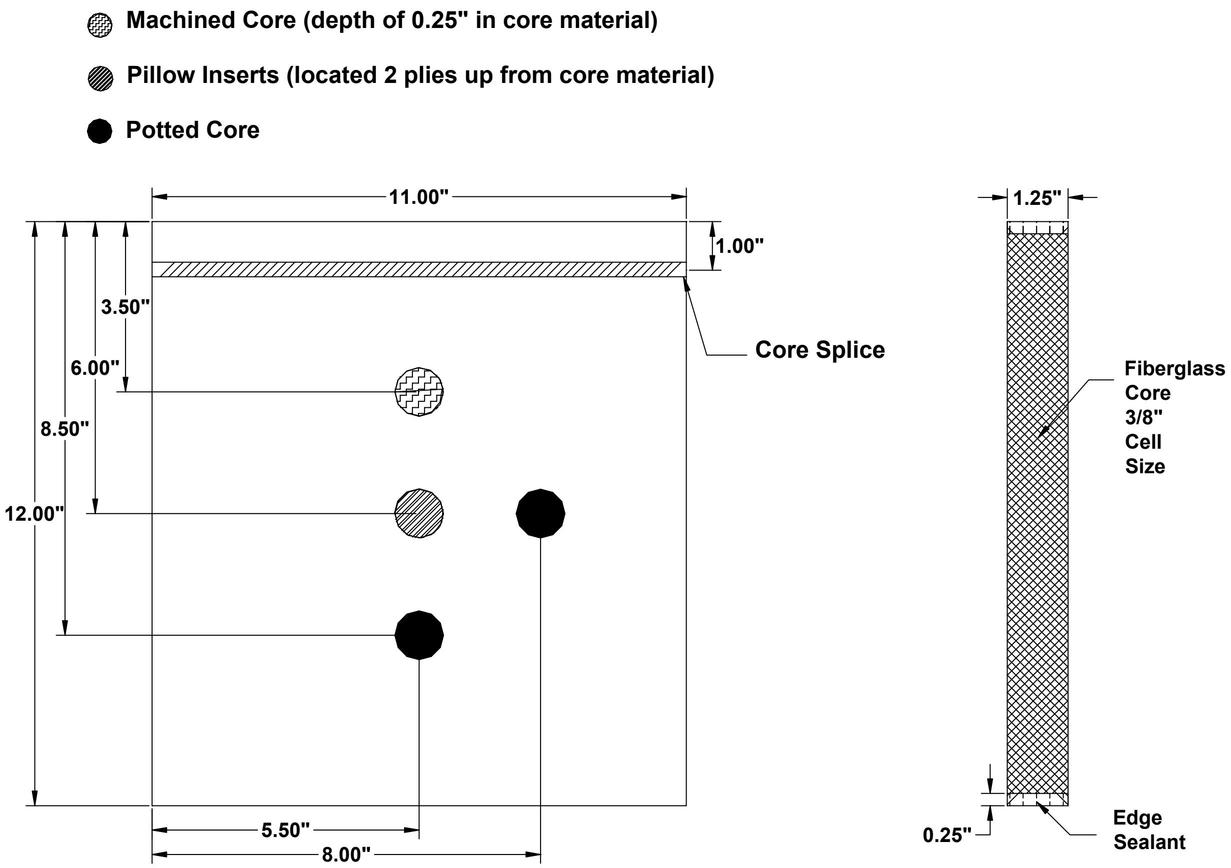

FIGURE 6. SCHEMATIC OF A REFERENCE STANDARD USED FOR NDI INSPECTION

NDI methods used for the purpose of this investigation are described as follows:

- Through-Transmission Ultrasonic (TTU) C-Scan: During this test, two water jets, precisely aligned with each other, are used to transmit ultrasonic waves through the thickness of the inspected structure. The alignment is maintained at all times while the component is being scanned. Two transducers are used, one acting as a transmitter and the other as a receiver of the sound energy waves. A reduction or a loss of the signal generated by the transmitter indicates the existence of a flaw. The key parameter in this test is the gain value, which is used to adjust the resolution of the C-scan. A C-scan is generated as the component is being inspected. A C-scan is a two-dimensional map or a grayscale image that shows damage distribution in terms of levels of attenuation. The TTU C-scan device is shown in figure 7.

FIGURE 7. WICHITA STATE UNIVERSITY ULTRAPAC SCANNER (C-SCAN)

- Manual Tap Test (Airbus Tap Hammer Device): This test is usually performed using a small diameter rod or hammer. The surface of the structure is tapped, and the audible response is monitored by the human ear. The audible response resonating from the structure reflects the stiffness of the area being tapped. Flaws can be detected when a change in the audible response occurs as the structure is tapped. Typically, a dead sound is a clear indication of damage in the sandwich structure [6]. The tap hammer used in this investigation is shown in figure 8.

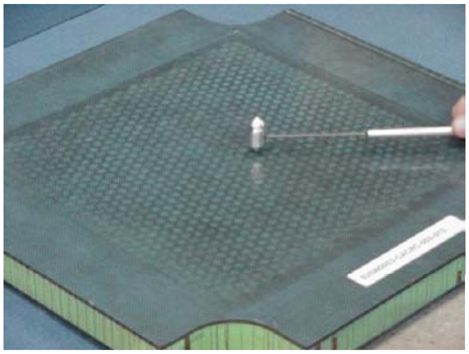

FIGURE 8. MANUAL TAP HAMMER

- Automated Tap Test: This test is very similar to the manual tap test except that a solenoid is used instead of a hammer. The solenoid produces multiple impacts in a single area. The tip of the impactor has a transducer that records the force versus time signal of the impactor. The magnitude of the force depends on the impactor, the impact energy, and the mechanical properties of the structure. The impact duration (period) is not sensitive to the magnitude of the impact force; however, this duration changes as the stiffness of the structure is altered. Therefore, the signal from an unflawed region is used for calibration, and any deviation from this unflawed signal (period) indicates the existence of damage. The Mitsui Woodpecker device was used to perform the automated tap tests for this investigation and is shown in figure 9.

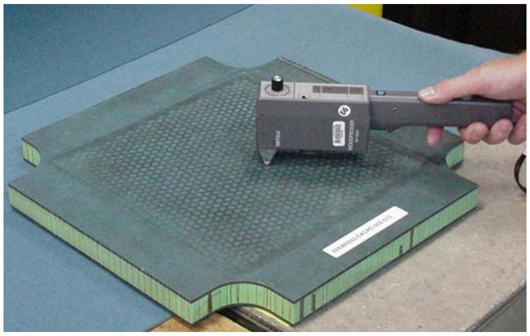

FIGURE 9. MITSUI WOODPECKER

- Mechanical Impedance Analysis (MIA) (V-95 Device): This device measures the mechanical impedance, or stiffness, of a structure. Sonic vibrations are input into the structure using a probe with a driver and receiver crystal in series. The driver generates the sonic vibrations, and the receiver converts the sonic response to an electrical signal that is analyzed by the instrument. The returned signal is proportional to the stiffness of the structure. An unflawed region is used to calibrate the instrument. A loss of or decrease in signal from this calibration corresponds to a loss in stiffness, therefore, the existence of a flaw [6]. A picture of this device is shown in figure 10.

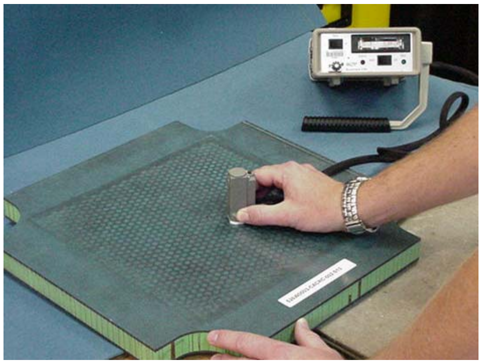

FIGURE 10. MECHANICAL IMPEDANCE DEVICE

- Low-Frequency Bond Tests (MAUS C-Scan Device): This device introduces a pressure wave into the specimen and detects the transmitted or reflected wave [6]. A complex wave front is generated internally in the material as a result of velocity characteristics, acoustical impedance, and thickness of the structure. This instrument processes the received signal and displays it on an amplitude/phase indicator. Any damage or flaws in the structure affect the time of wave travel and the amount of energy received. Phase and amplitude displays are used to detect flaws in an A-scan signal. This information can be color-coded into a two-dimensional map (C-scan) to highlight the variations in phase and amplitude that indicate the existence of a flaw. The MAUS C-scan device used for this investigation is shown in figure 11.

FIGURE 11. MAUS C-SCAN DEVICE

2.5.3 Performance of Different NDI Methods.

The main objective of the NDI investigation was to evaluate the effectiveness of different inspection methods used for flaw detection and sizing. A plot summarizing the results of the investigation is shown in figure 12. Elements in this study had three-ply facesheets. Data corresponding to two-, four- and six-ply facesheets were obtained from a previous study [7]. A 3-inch-diameter impactor was used to inflict damage on the picture frame shear elements.

Damage radii obtained from the different NDI methods used for inspection were compared to the radii obtained from the TTU C-scan method. A prior study [5] showed a good correlation between the actual damage size and the size predicted by the TTU C-scan. Flaw sizes illustrated in figure 12 are shown as a fraction of the value obtained using the TTU C-scan.

The results from the study can be summarized as follows: The more sophisticated the method, the more accurate it was in determining the size of the damage. Furthermore, as the thickness of the facesheet increased, the accuracy of detection decreased. This plot shows that all methods of inspection, with the exception of the TTU scan used by Delta Air Lines, underpredicted the size of the damage, with the airbus tap hammer being the least accurate. As expected, the TTU instrument described the largest damage for the three-ply facesheet sandwich shear elements. Data from this instrument was not available for the two-, four-, and six-ply facesheet structures.

Comparing the methods available for all the facesheet lay-up configurations, it was found that the mechanical impedance method yielded the most accurate results, with a capability of flaw detection of 88% of the actual size for the two-ply facesheet structure and 64% of the actual flaw size for the six-ply facesheet structure.

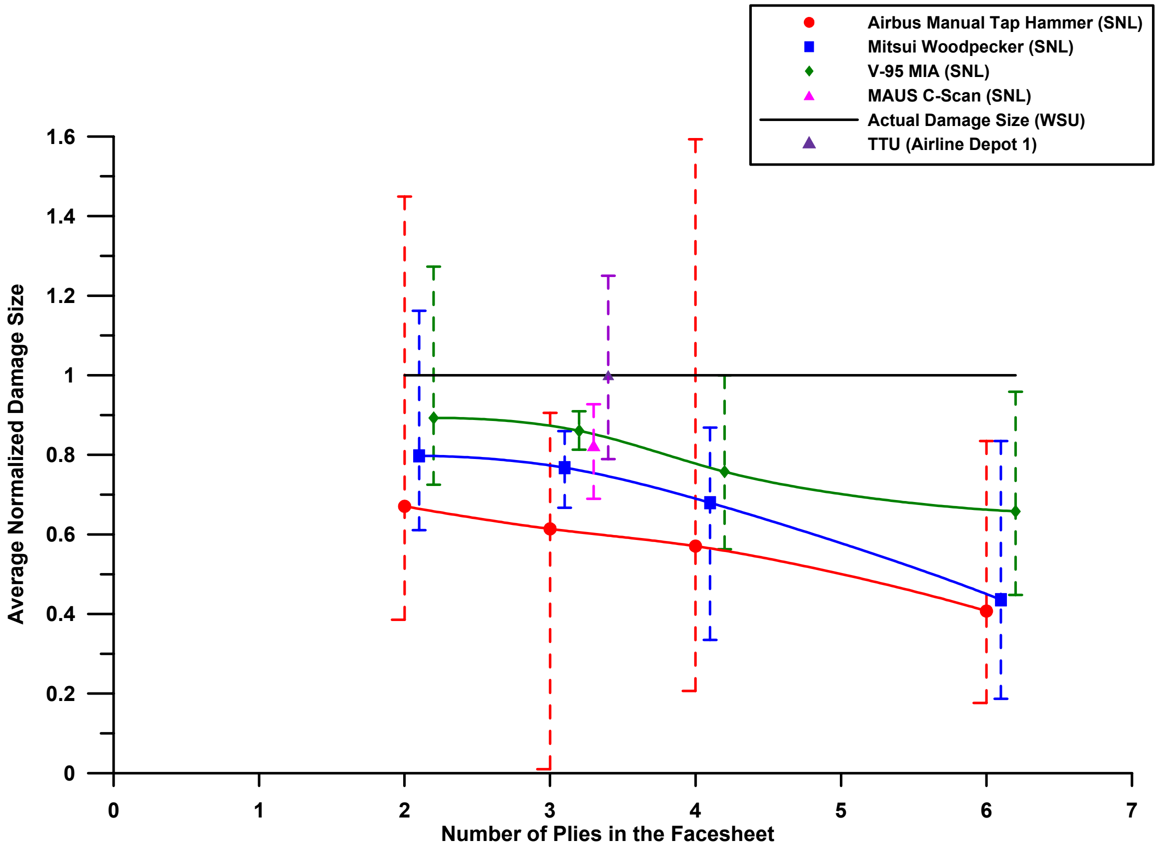

FIGURE 12. PERFORMANCE OF DIFFERENT NDI METHODS IN DETECTING DAMAGE FOR SANDWICH PANELS WITH DIFFERENT FACESHEET LAY-UPS

2.6 STRUCTURAL REPAIR.

To obtain consistent results among the airline repair depots, each repair station was asked to repair a 4-inch-diameter hole in the facesheet, which was routed at the impact location through one facesheet only. The bottom facesheet remained intact. This 4-inch-diameter hole was larger than any amount of damage that may have been caused by the impacts investigated in the previous section.

Two structural repair methods were chosen for the purpose of this study: a CACRC-developed wet lay-up repair procedure with an extra repair ply and a 0.50-inch scarf overlap, enumerated in appendix A, and an OEM-approved prepreg repair procedure with no extra ply and a 0.25-inch scarf overlap. Drawings of the repaired picture frame shear elements are shown in figures 13 and 14. Pictures of the steps followed to perform the repairs are shown in figures 15 and 16.

The wet lay-up repair system used was TENEX HTA5131200TEXF3000 fibers with Epocast 52 A/B laminating resin. The resin was used to impregnate the plies and to bond the core plug to the existing core. The repair was cured at 200°F, unlike the parent material that was cured at 350°F. The repair patch used had a scarf overlap of 0.5 inch and an extra structural ply.

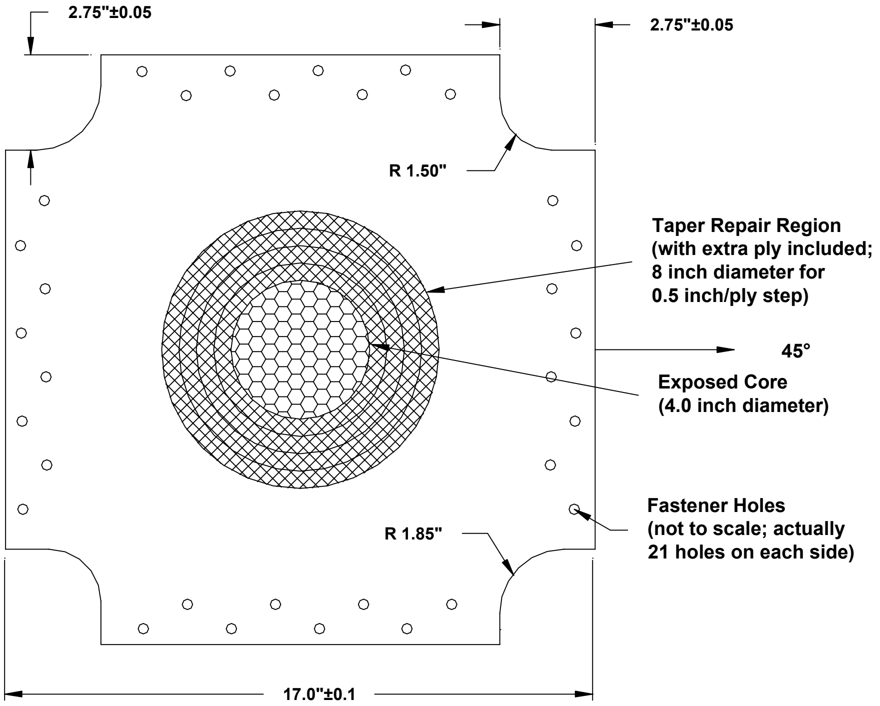

FIGURE 13. PICTURE FRAME SHEAR ELEMENT REPAIRED USING THE CACRC-DEVELOPED METHOD

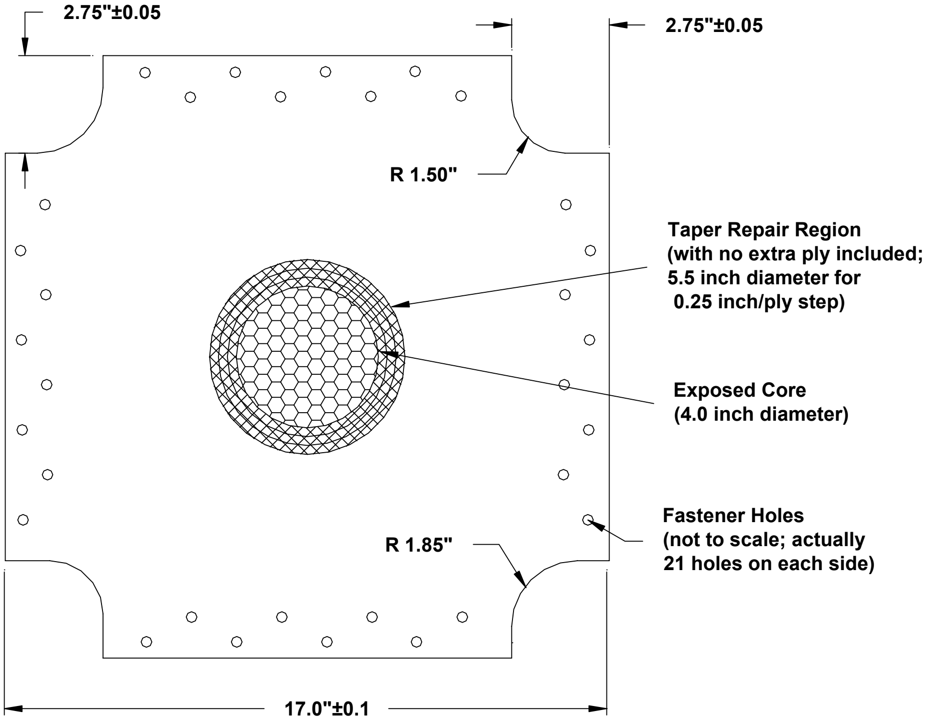

FIGURE 14. PICTURE FRAME SHEAR ELEMENT REPAIRED USING THE OEM METHOD

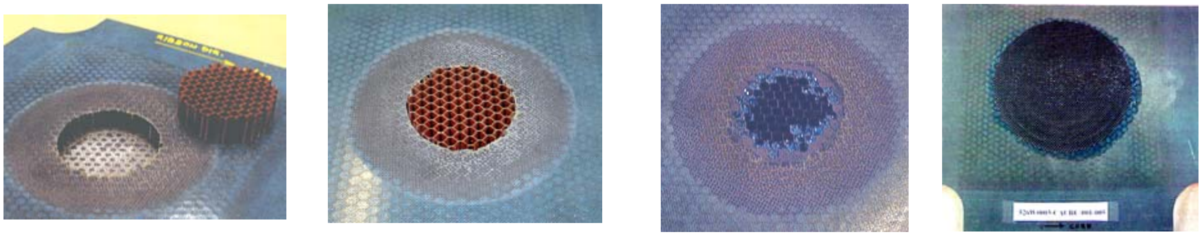

FIGURE 15. WET LAY-UP (CACRC) REPAIR METHOD

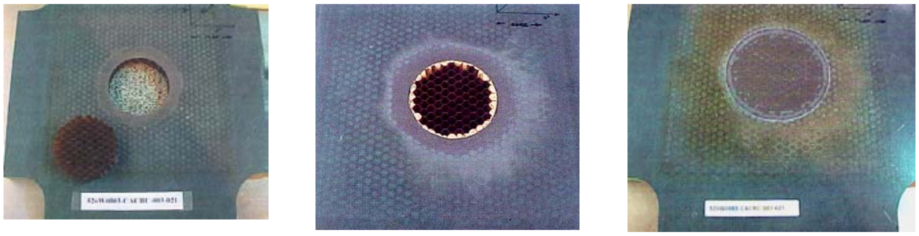

FIGURE 16. ORIGINAL EQUIPMENT MANUFACTURER PREPREG REPAIR METHOD

The repair system used by the OEM was T300/934 3K-70-PW prepreg with FM 377S adhesive. The core plug was attached to the existing core using a film adhesive, and the repair was cured at 350°F, similar to the parent structure. Unlike the CACRC-developed method, no extra ply was used.

As shown in figures 13 through 16 for the same damage size, the OEM method used a much smaller repair (5.5 inch diameter) than the CACRC-developed method (8 inch diameter).

Figures 15 and 16 emphasize the differences between the two methods considered. The taper repair area was much larger for the wet lay-up repair than it was for the prepreg repair. For the wet lay-up repair, the same resin used to impregnate the plies was used to bond the core plug to the exiting core. For the OEM repair, a core-splicing adhesive was used to bond the core plug to the existing core. The final repairs were different in terms of materials and cure temperatures but also in terms of their respective lengths.

2.7 NONDESTRUCTIVE INSPECTION OF REPAIRED PICTURE FRAME SHEAR ELEMENTS.

To assess the quality of the bonded repairs, 25% of the coupons were inspected for possible defects at the Sandia National Laboratories using some of the methods previously mentioned. The MAUS C-scan was used in MIA and resonance modes. As previously mentioned, the mechanical impedance analysis is a method of inspection used widely for bond testing. A probe, directly in contact with the part to be inspected, compares the difference in mechanical impedance, or stiffness, of the various areas in the structure. A disbond or a flaw causes a decrease in the impedance and therefore a reduction of the amplitude of the displayed signal.

Resonance testing is a method of high-frequency bond testing that uses, similar to a TTU inspection, transducers coupled to the part to be tested using a coupling agent. Transducers transmit an acoustic wave through the material, which in turn changes the transducer's bandwidth and resonance frequency [6]. A change in the acoustic impedance (stiffness) of the material indicates the existence of a flaw and therefore modifies the electrical signal received by the transducer, which is displayed as a change in the amplitude or phase of the output information. Results of the inspections are shown in figures 17 and 18. No flaws were found in the repairs; however, it should be noted that the color of the repairs, though constant throughout the repairs, is different from the color in the parent structure, which is due to the difference in mechanical and acoustical impedance between the repair material and the parent material. This discrepancy is due to the use of a different material and an extra ply for the wet lay-up repair. It could also be due to residual thermal stresses for the prepreg repair, which would change the attenuation response of the structure.

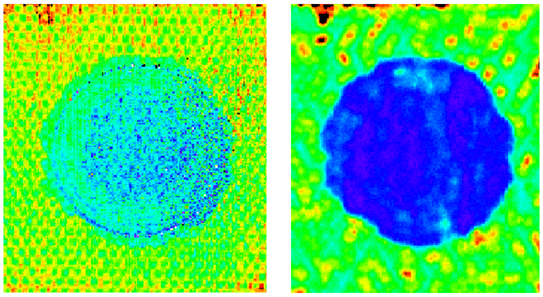

FIGURE 17. MAUS C-SCAN OF A PREPREG REPAIR USING THE MIA AND RESONANCE MODES

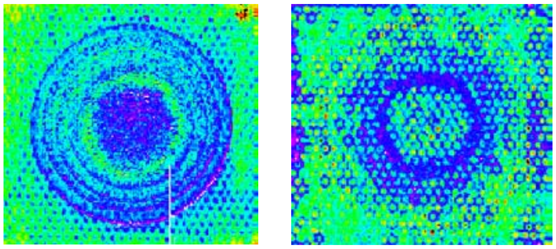

FIGURE 18. MAUS C-SCAN OF A WET LAY-UP REPAIR USING THE MIA AND RESONANCE MODES

2.8 STRUCTURAL TESTING.

The ultimate goal of this investigation was to assess the structural integrity of repairs to fiber-reinforced composite sandwich structures, i.e., evaluate their effectiveness in restoring the strength of the original shear elements. The second goal was to compare the two repair methods used to repair damage.

2.8.1 Test Setup.

A 100-kip servohydraulic actuator mounted on a 150 kip MTS load frame was used for loading (see figure 19). The MTS test equipment was calibrated and verified according to the ASTM E 4 standard to ensure the accuracy of the load and displacement readings. A Boeing test fixture was used to perform the picture frame shear tests. Two clevises were bolted to the load frame and were used to attach the fixture to the test machine using cylindrical pins. The coupons were mounted to the fixture using 1/4-inch-diameter fasteners tightened with the same amount of torque.

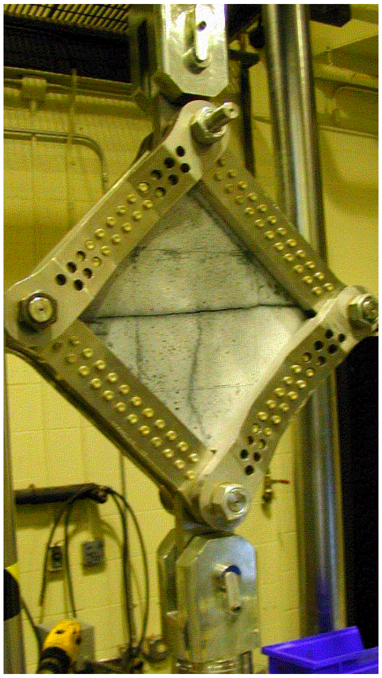

FIGURE 19. PICTURE FRAME SHEAR ELEMENT TEST SETUP

The shear elements were loaded at a rate of 0.03 in/min. The actuator was controlled with the MTS Flextest II system, and the MTS Basic Testware software was used to program the parameters for controlling the test and acquiring data. Recorded data included time, actuator displacement, force, and strain gage readings. The MTS Flextest II system has the capability of acquiring analog data on up to 24 channels.

2.8.2 ARAMIS System.

To characterize the strain distribution in the undamaged/repaired panels and possibly detect regions of high-stress concentrations, a deformation measurement system, ARAMIS, was used [8].

2.8.2.1 Description.

The ARAMIS system consists of a pair of high-resolution (HR) cameras arranged to form an angle of 20° to 60°, with respect to the object of interest. Two different sets of cameras can be used, depending on the depth of view and the size of the object of interest. For larger objects that require more depth of view, the standard ARAMIS setup is used. The corresponding camera resolution for this setup is 768 x 572 pixels, and the strain measuring range is between 0.05% and 100%. For smaller objects that require high resolution, the ARAMIS HR system is used.

The corresponding camera resolution for this setup is 1280 x 1024 pixels, and the strain measuring range is between 0.02% and 100%. Pictures of these two different setups are shown in figures 20 and 21.

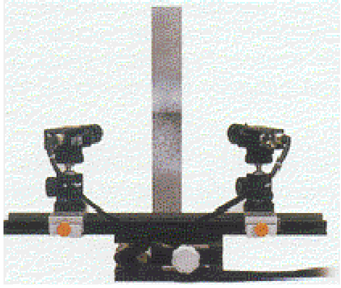

FIGURE 20. ARAMIS STANDARD SETUP

FIGURE 21. ARAMIS HR SETUP

A random pattern is applied to the surface of the structure prior to loading. This pattern consists of a combination of light and dark areas with a 50:50 ratio. The pattern should show a distinct contrast with respect to the surface so that the matching of the pixels in the image can be performed correctly. The size of the pattern should be small enough to allow the use of a fine grid of facets but large enough to solve the project in a reasonable amount of time.

Furthermore, the sensor must be calibrated before taking measurements. Different calibration panels with varying sizes from 10 x 8 mm^2 to 1200 x 960 mm^2 are available. Different parameters defining the size and type of lenses, and the size of the calibration panel, are entered prior to the calibration process. The calibration object is then positioned the same distance from both cameras such that the angle formed at the intersection of the calibration panel is between 20° and 60°. First, a picture of the calibration object is taken at different angles and distances from the cameras, then the software analyzes the views from both cameras and ensures that every point in the left view is found in the right view, within a certain tolerance. If the software fails to match points from one camera to the other, an error message is displayed, and the calibration cannot proceed until the object is repositioned. When the calibration is completed, the program generates accuracy measurements of the calibration. Based on these numbers, the operator decides whether to use that calibration or to perform another one to obtain better accuracy values.

Once the calibration is completed, the structural test is ready to be carried out. The test coupon is placed the exact same distance as the calibration panel. A reference picture is taken prior to loading. The ARAMIS system assigns reference coordinates to every pixel in the image. Pictures of the structure are recorded at different load levels. The ARAMIS system compares every picture to the previous one and registers any changes in the displacement and rotation. Given the displacement and rotation values, strains can be calculated. ARAMIS provides a variety of ways for postprocessing the data: two-dimensional or three-dimensional maps of the displacements or strains and stresses displayed as a function of spatial position. Section plots can also be obtained showing the distribution of displacements, stresses, or strains in a particular section of the test coupon. Therefore, regions with high-stress concentrations can be identified and thoroughly characterized.

Figure 22 shows the y strain distribution, or strain in the direction of the load, in a repaired picture frame shear coupon at different load levels. It also shows high-stress concentrations at the taper repair area where the failure was initiated.

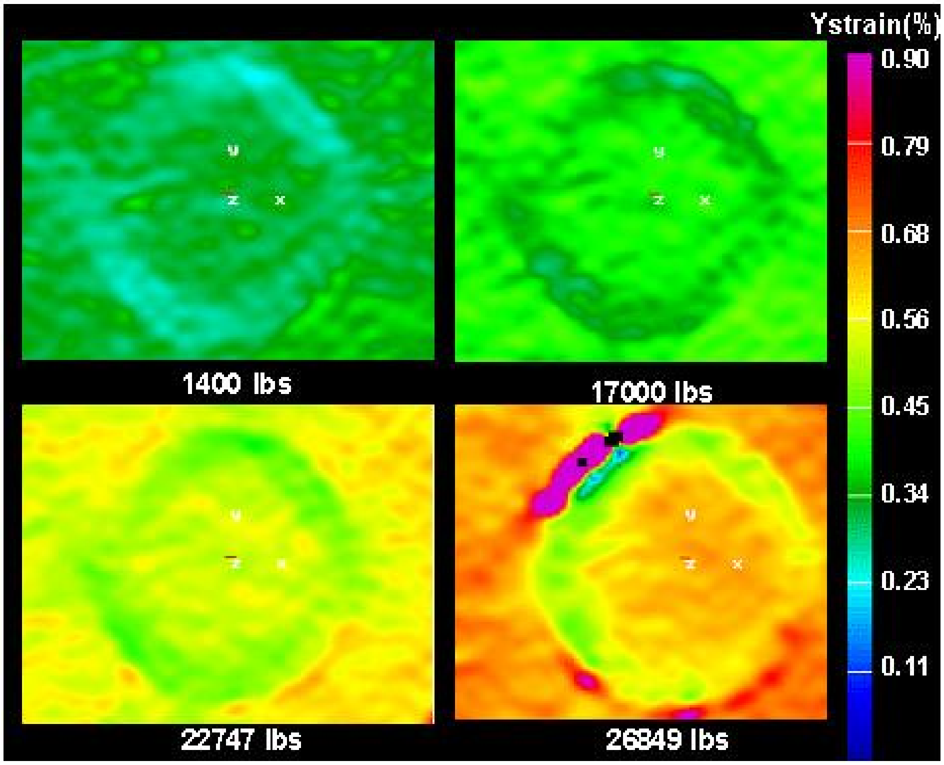

FIGURE 22. Y STRAIN DISTRIBUTION AT DIFFERENT LOAD LEVELS FOR A PICTURE FRAME SHEAR ELEMENT REPAIRED WITH THE OEM METHOD

As shown in figure 23, the taper repair area appears to be the region with the concentration of stresses leading to failure. Peak tensile strains in the order of 9000 microstrain were achieved just before failure initiated in the taper repair area. In the middle of the patch, a quasi-constant tensile strain in the order of 6500 microstrain was recorded. Strain gages were attached at different locations on the picture frame shear elements for comparison purposes. It was found that the strain data, obtained using the ARAMIS, and strain gages correlated very well. This definitely shows the usefulness of such software in characterizing the deformation of a given coupon at every single point. This cannot be achieved using strain gages, which give an average strain value over a given area and not an exact strain value at a specific point.

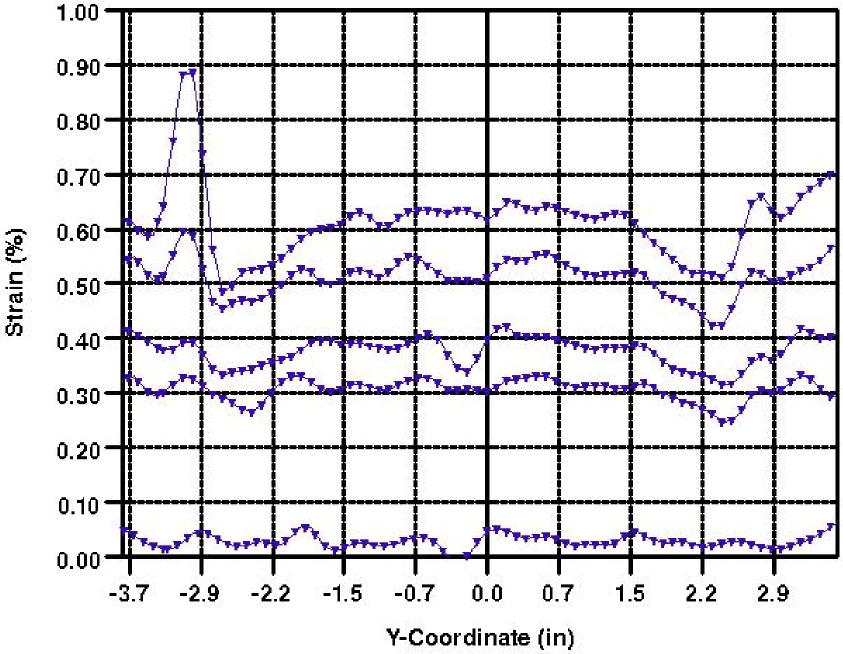

FIGURE 23. Y STRAIN DISTRIBUTION IN A VERTICAL SECTION PASSING THROUGH THE CENTER OF THE REPAIR

2.9 RESULTS.

Figure 24 summarizes the results from the repair procedure investigation. As previously mentioned, the main objective of the investigation was to evaluate the structural performance of picture frame shear elements repaired using two different methods at different airline depots. For comparison purposes, baseline pristine shear elements, as well as elements repaired at the OEM, were also tested. All data presented in figure 24 were normalized with respect to the average of the failure loads obtained for undamaged shear elements.

As was expected, BVID inflicted at the center of the repair patch had no effect on the structural performance of the picture frame shear elements; all three impacted coupons reached at least 99% of the average strength of the undamaged coupons.

As shown in figure 24, the picture frame shear elements repaired by the OEM using a prepreg patch restored the original strength; of all three shear elements loaded to failure, two exceeded the average pristine strength (100%) and one reached 95% of this value. This demonstrates that the OEM prepreg repair, if properly implemented, is capable of restoring the structure's initial strength capacity.

The same repair concept implemented by airline depots 2, 3, and 4 exceeded the average strength of the pristine shear elements, i.e., the 100% value, except one shear element repaired by airline depot 4 only reached 88% of the undamaged strength. However, using the same repair methodology, the strength values obtained from shear elements repaired at airline depot 1 were 25% lower than the average undamaged strength.

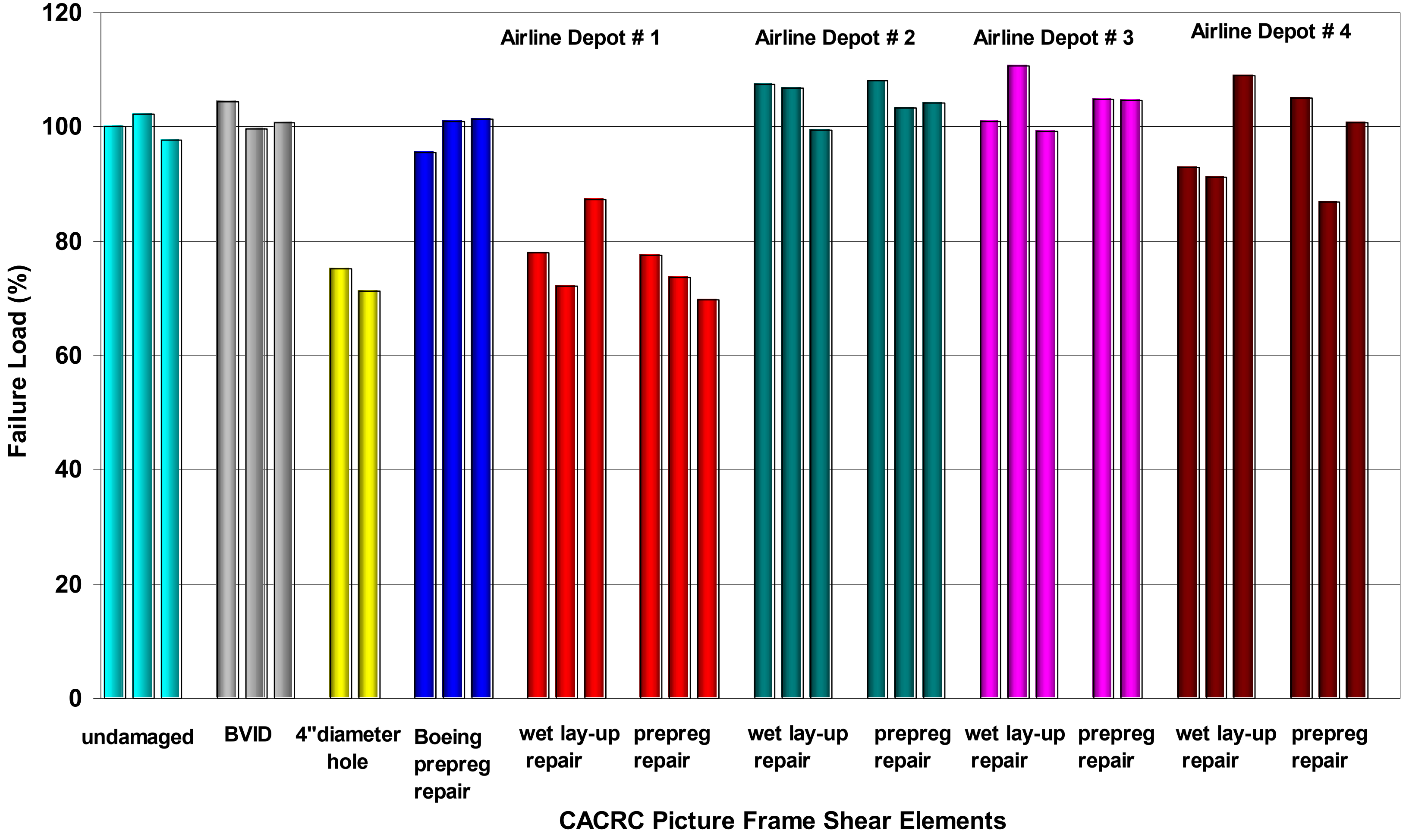

FIGURE 24. PERFORMANCE OF OEM VERSUS FIELD STATION REPAIRS

When assessing the validity of the wet lay-up repair methodology, it was found that shear elements repaired by airline depots 2, 3, and 4 reached at least 92% of the original strength. Of all nine shear elements tested, only two had strength values below 99% of the undamaged strength. However, the wet lay-up repairs carried out at airline depot 1 showed a strength reduction of about 23% with respect to the baseline undamaged strength.

In an attempt to identify what might have caused the premature failure of the picture frame shear elements repaired at airline depot 1, shear elements with a 4-inch-diameter hole routed to the bottom facesheet were loaded to failure. The average strength of these shear elements was 25% lower than the average pristine strength. Furthermore, the failure mode of the shear elements repaired by airline depot 1 was different then that observed for the repair specimens, which failed at loads close to the undamaged strength. Failure of the repair from airline depot 1 initiated at the edge of the repair patch and propagated to the corners, the same mode exhibited by the shear elements tested with a hole routed in the middle. This led to the conclusion that these repair patches were not properly bonded and that a region of high-stress concentration formed around the routed hole causing failure to initiate. The cause of the premature failure of airline depot 1 was attributed to the unskilled personnel making the repair.

As illustrated in figure 25, the repaired picture frame shear coupons exhibited different modes of failure. The dominant failure mode was at the taper repair area, indicative of a shear failure of the adhesive, as shown in figure 25(a). This was the expected failure. Two other failure modes were recorded for some elements that initiated in the vicinity of the gripping fixture or reinforced panel near the panel edges. The failure across the patch through the corners shown in figure 25(b) is indicative that the patch was effective in transferring load. For these elements, the failure initiated at the panel corner edges and propagated to the center. The third failure mode recorded occurred at the interface of the reinforced panel region with the inner nonreinforced structure, as shown in figure 25(c).

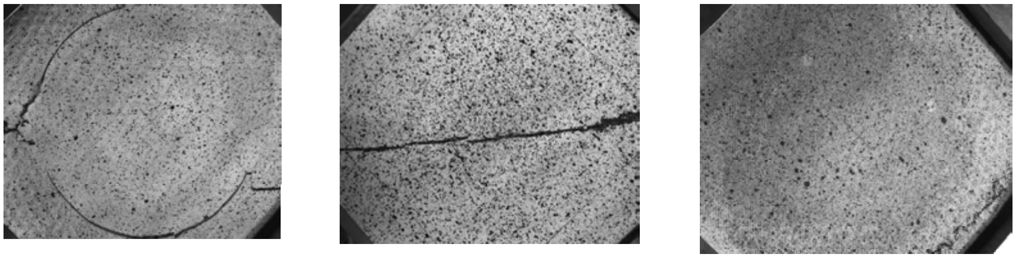

(a) (b) (c)

FIGURE 25. FAILURE MODES OF PICTURE FRAME SHEAR ELEMENTS

3. REPAIR VARIABLE INVESTIGATION.

The main purpose of this task was to investigate the effects of several variables on the performance of bonded scarf repairs on sandwich structures. The variables investigated included the following:

- Three different scarf overlap repair lengths: 0.15, 0.25 and 0.50 inch.

- Two different core cell sizes: 1/8 and 3/8 inch.
- One- and two-dimensional repairs: one-dimensional repairs being rectangular in shape and two-dimensional repairs being circular in shape.
- Different repair materials and cure temperatures: the large beams were repaired with the same material used for the parent structure, cured at 350°F. The small beams and the unidirectional tension coupons were repaired with two different systems; a wet lay-up material system and a prepreg material system, both cured at 250°F.

3.1 EXPERIMENTAL SETUP/COUPON CONFIGURATION.

3.1.1 Large Four-Point Bending Beams.

The different large beam repair configurations tested are shown in figure 26. For all coupons considered, only one facesheet was repaired using a two-dimensional circular repair. The core was not repaired. All the coupons were tested with the repair facesheet in compression. A custom-made, four-point bending fixture, as shown in figure 27, was used to test these coupons. The fixture had two main components: a component fastened to the floor and a component fastened to the load cell. Both components had two steel bearings attached to them to simulate a four-point bending condition. Load was applied using two cylindrical upper steel bearings positioned 18 inches apart. These bearings made contact with the upper facesheet of the coupon so that the load applied was uniformly distributed along the areas of contact of the steel bearings with the specimens. The lower steel bearings acted as simple supports for the coupons. To avoid localized core crushing at the loading points, a foaming adhesive was used to reinforce those areas. The four-point bending fixture used a 55-kip servohydraulic actuator for loading. The upper component of the fixture was fastened to the actuator, and the weight of the fixture was cancelled before loading. The test machine was calibrated periodically, according to the ASTM E4 standard, to ensure the accuracy of load and displacement readings.

A servovalve was used to control the amount of load applied by the actuator, which in turn was controlled using the MTS Flextest II system. Data acquisition was performed using the MTS Basic Testware software. The data acquired corresponded to actuator load, displacement, deflectometer, and four strain gage readings. The coupon alignment was checked prior to testing. Specimens were then loaded to about 500 microstrain and brass shims of different thicknesses were used to correct any misalignment. Structural tests were conducted when all strain gage readings were within 10%. All tests were performed under displacement control at a rate of 0.1in/min to reach the maximum load in 3 to 6 minutes. A deflectometer was used to monitor the bending deformation at the centerline of the coupons.

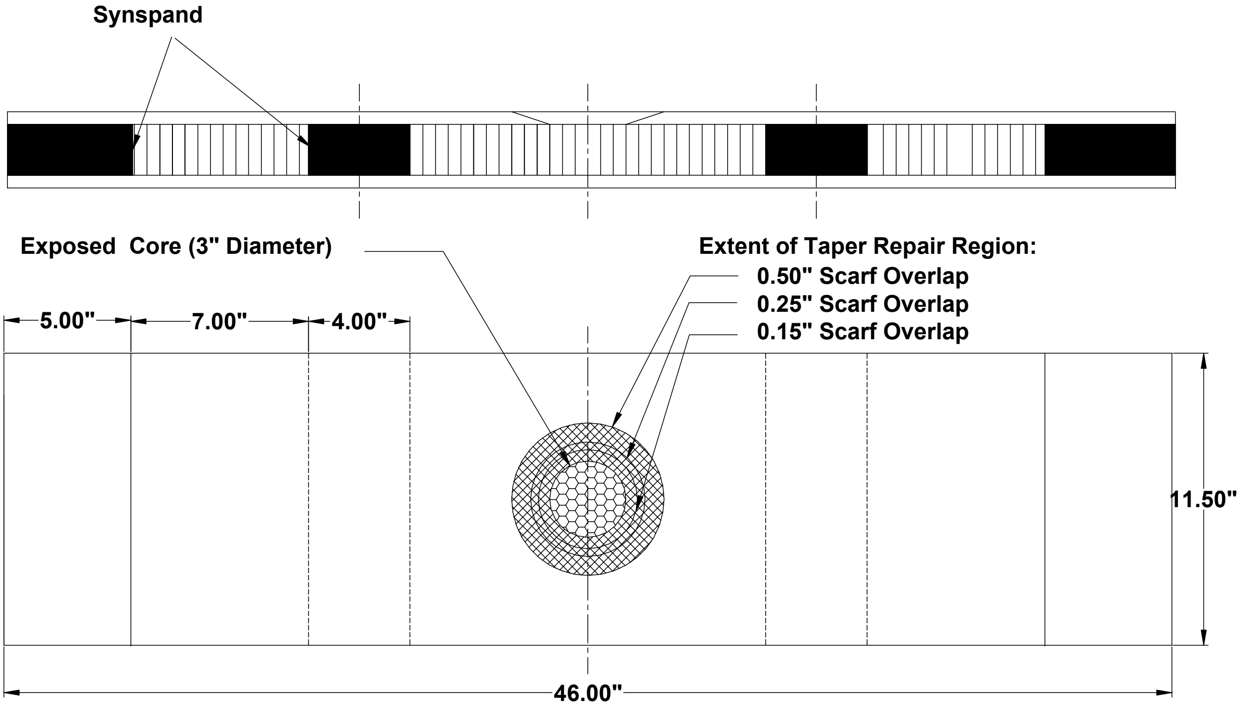

FIGURE 26. LARGE FOUR-POINT BENDING BEAM REPAIR CONFIGURATIONS

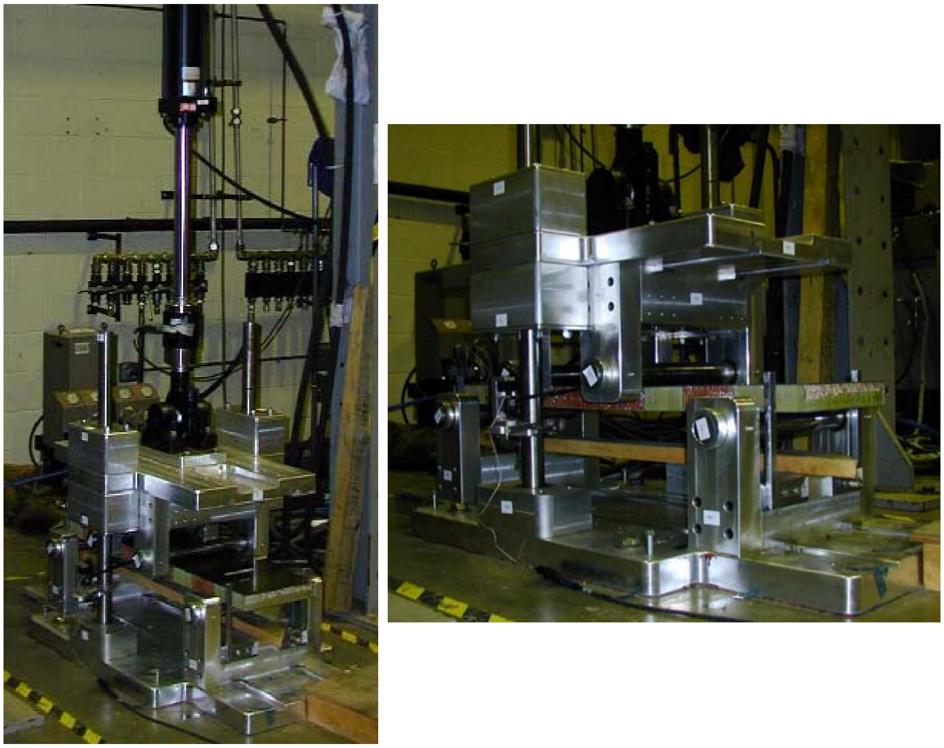

FIGURE 27. LARGE FOUR-POINT BENDING BEAM TEST SETUP

3.1.2 Small Four-Point Bending Beams.

The different small beam repair configurations tested are shown in figure 28. These repairs were one-dimensional, i.e., rectangular in shape. Only one facesheet was repaired, the other facesheet remained intact, and the core was not repaired. All coupons were tested with the repair facesheet in compression. It should be noted that the 0.50-inch step repair was very close to the loading region.

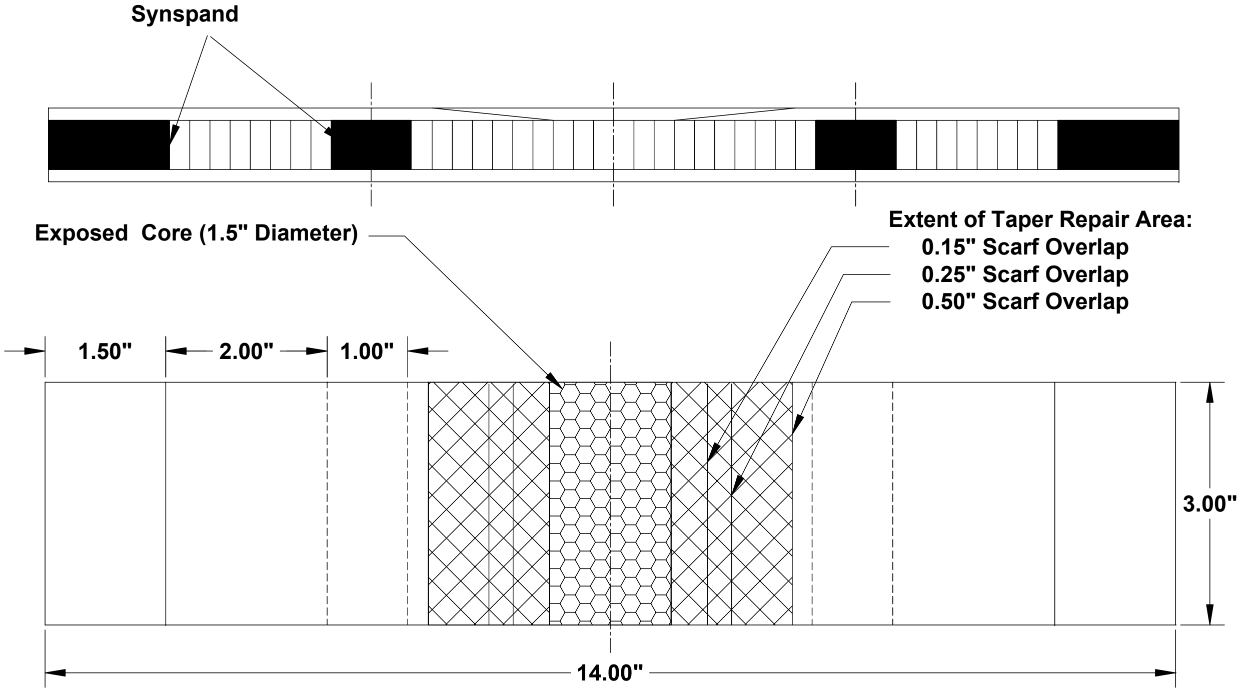

FIGURE 28. SMALL FOUR-POINT BENDING BEAM REPAIR CONFIGURATIONS

A custom-made, four-point bending fixture, as shown in figure 29, was used for testing. To avoid crushing the core at the loading points, a foaming adhesive was used to reinforce those areas. The fixture, mounted on an MTS load frame, used a 22-kip servohydraulic actuator for loading. The MTS test machine was calibrated according to ASTM E4 standard to ensure that load and displacement readings were accurate.

MTS Testworks 4.0 software was used to acquire data and to program the different parameters used to control the test. MTS-Testar II hardware controlled the actuator. The load rate was 0.05 in/min. A deflectometer monitored the bending deformation at the centerline of the coupons, and strain gages monitored center-beam strains and far-field strains to ensure the uniformity of the load applied.

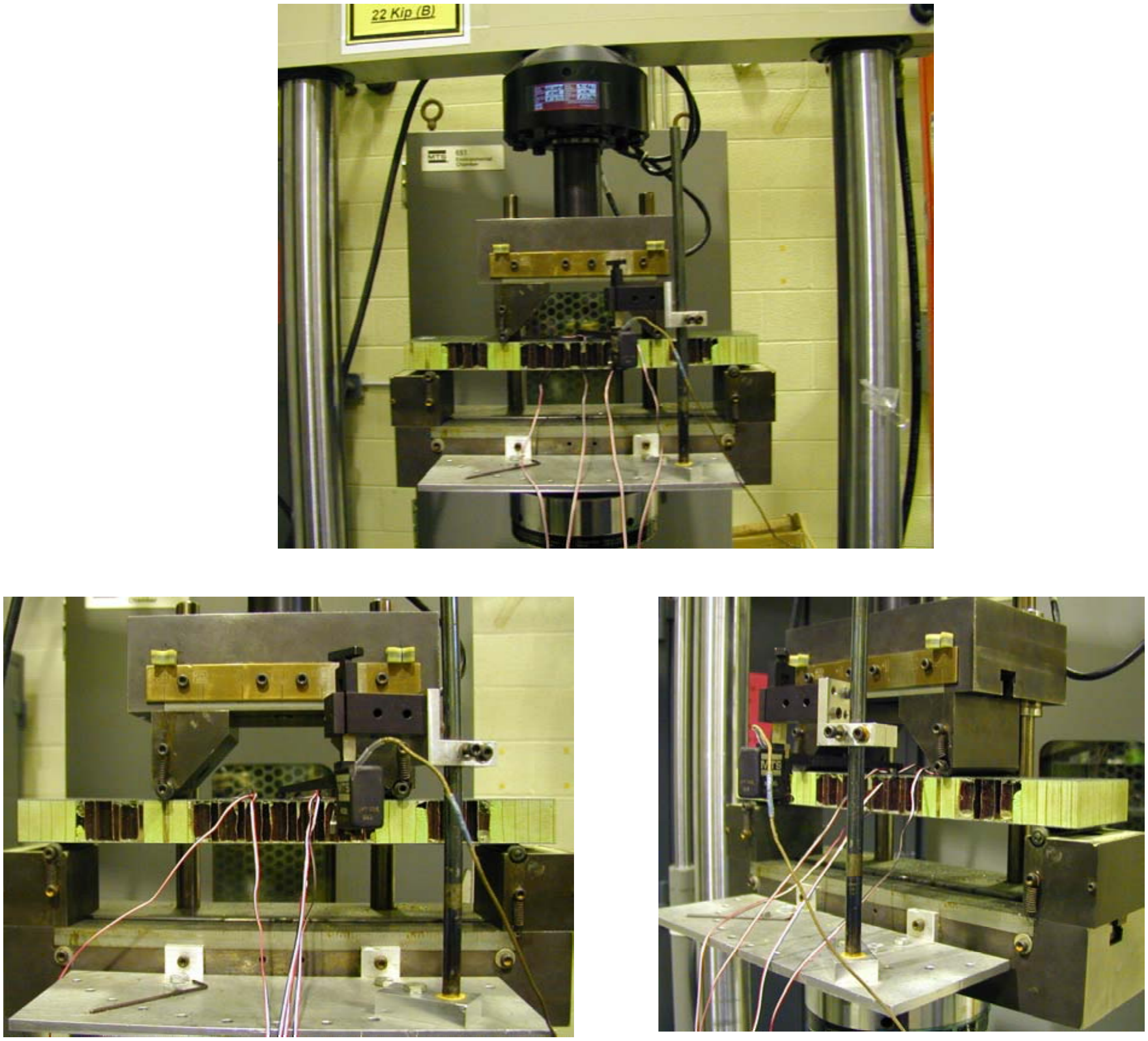

FIGURE 29. SMALL FOUR-POINT BENDING BEAM TEST SETUP

3.1.3 Unidirectional Tension Coupons.

The different unidirectional tension repair configurations tested are shown in figure 30. As for all other coupons previously mentioned, only one facesheet was repaired using a one-dimensional rectangular repair, and the core was not repaired. A total of 18 holes were drilled on the coupons to fasten the specimens to the fixture.

A Boeing fixture, shown in figure 31, was used for testing the unidirectional tension coupons. The fixture was mounted on clevises using cylindrical pins. The clevises were bolted to the load frame. The MTS hydraulic test machine used a 110-kip actuator for loading. As previously mentioned, the MTS machines were periodically calibrated according to the ASTM E4 standard so that the measured load was within 1% of the actual load.

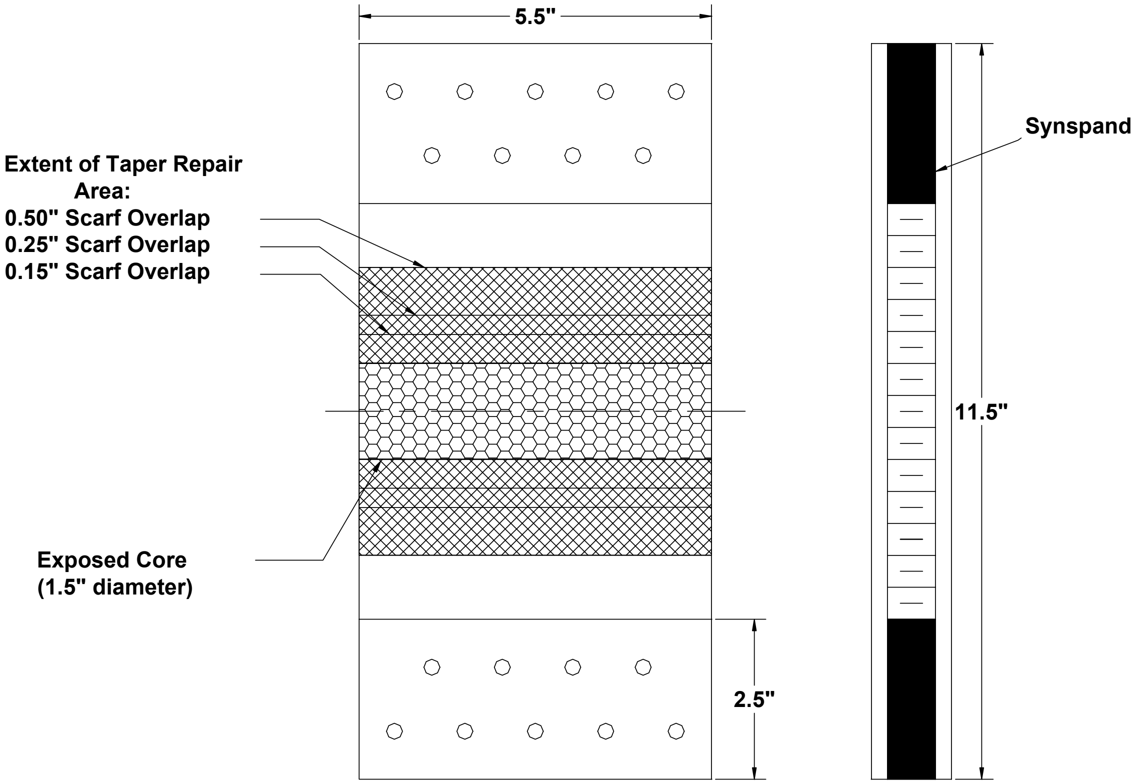

FIGURE 30. UNIDIRECTIONAL TENSION COUPON REPAIR CONFIGURATIONS

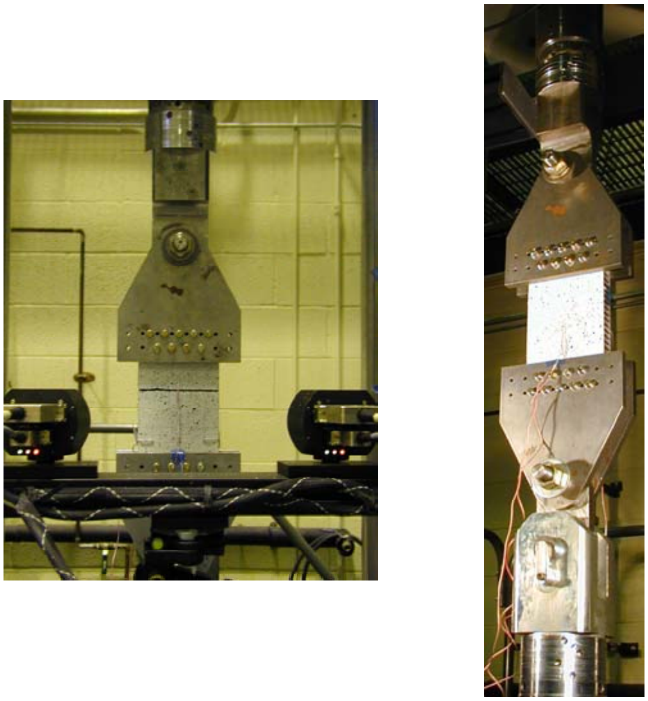

FIGURE 31. UNIDIRECTIONAL TENSION COUPON TEST SETUP

A servovalve was used to control the amount of load applied by the actuator, which in turn was controlled with the MTS Flextest II system. All data acquisition was performed using the Basic Testware software. Data acquired corresponded to actuator load, displacement, deflectometer readings, and four strain gage readings. All tests were conducted under displacement control at a rate of 0.02 in/min to reach the ultimate load in 3 to 6 minutes.

3.2 TEST MATRIX.

The following is a summary of all the test matrices used for the repair variable investigation.

3.2.1 Large Four-Point Bending Beams.

Table 2 shows the test matrix used for the large four-point bending beams. As indicated, 60 large four-point bending beams were used for the repair variable investigation. These beams were repaired using a two-dimensional repair, with three different scarf overlaps and two different core cell sizes. As shown in the table, half of these coupons were impacted to determine the effects of BVID on the strength of the coupons. Damage was inflicted at the center of the taper repair area of the coupons with a 1.2-inch-diameter steel impactor using an energy level of 17 in-lbf to produce a BVID.

TABLE 2. LARGE FOUR-POINT BENDING BEAM TEST MATRIX

Repair Configuration	Repair Material (350°F Cure) (Same as Parent Material)	Scarf Overlap (in)	1/8-inch Core	3/8-inch Core	1/8-inch Core Impacted	3/8-inch Core Impacted
Two-Dimensional Compression	T300/934 3K-70-PW Prepreg With FM 377S Adhesive	0.15	5	5	5	5
		0.25	5	5	5	5
		0.50	5	5	5	5
Total Sandwich Beams		60				

3.2.2 Small Four-Point Bending Beams.

Table 3 shows the test matrix used for the small four-point bending beams. As indicated, 36 small beams were used in the repair variable investigation. These beams were repaired using a one-dimensional repair, with two different repair materials, three different scarf overlaps, and two different core cell sizes. The main objective was to investigate the performance of 250°F cure repairs on a 350°F parent structure, given all the variables listed in table 3.

TABLE 3. SMALL FOUR-POINT BENDING BEAM TEST MATRIX

Repair Configuration	Repair Material (250°F Cure)	Scarf Overlap (in)	1/8-inch Core	3/8-inch Core
One-Dimensional Compression	M1: Fibercote E765 Prepreg With SIA 795-1 Adhesive	0.15	0	3
		0.25	0	3
		0.50	0	3
	M2: Cytec BMS9-8, 3K-70-PW Cloth With EA9696 Adhesive	0.15	6	3
		0.25	6	3
		0.50	6	3
Total Sandwich Beams		36		

3.2.3 Unidirectional Tension Coupons.

Table 4 shows the test matrix used for the unidirectional tension coupons. As indicated, 40 unidirectional tension specimens were used in the repair variable investigation. These coupons were repaired using a one-dimensional repair, with two different repair materials, three different scarf overlaps, and two different core cell sizes. The main objective was to investigate the performance of 250°F cure repairs on a 350°F parent structure, given all the variables listed in table 4.

TABLE 4. UNIDIRECTIONAL TENSION COUPON TEST MATRIX

Repair Configuration	Repair Material (250°F Cure)	Scarf Overlap (in)	1/8-inch Core	3/8-inch Core
One-Dimensional Tension	M1: Fibercote E765 Prepreg With SIA 795-1 Adhesive	0.15	3	0
		0.25	6	3
		0.50	3	3
	M2: Cytec BMS9-8, 3K-70-PW Cloth With EA9696 Adhesive	unrepaired	0	4
		0.15	3	0
		0.25	6	3
		0.50	3	3
Total Sandwich Plates			40	

3.3 RESULTS.

3.3.1 Large Four-Point Bending Beams.

Figures 32 and 33 show the effects of BVID on the strength and strain capacities of the large four-point bending beams with a 1/8-inch core cell size. For the undamaged beams, based on the average values, it can be seen that the strength or strain capacity did not change as a function of scarf overlap, that is, the size of the repair did not affect the structural performance of the undamaged coupons.

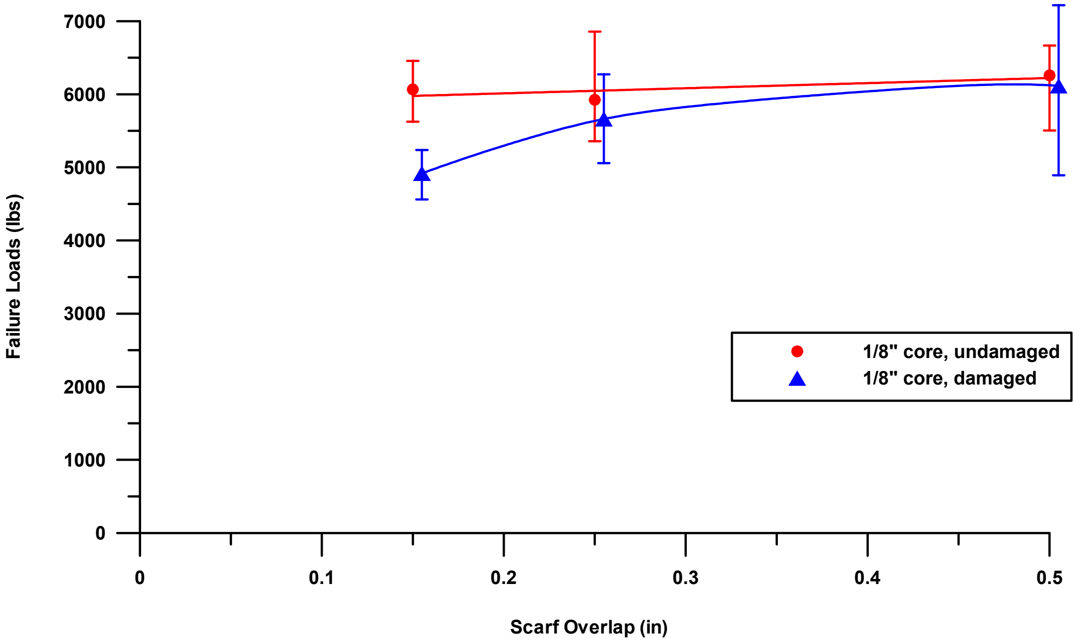

FIGURE 32. EFFECTS OF DAMAGE ON THE FAILURE LOADS OF 1/8-inch CORE LARGE FOUR-POINT BENDING BEAMS

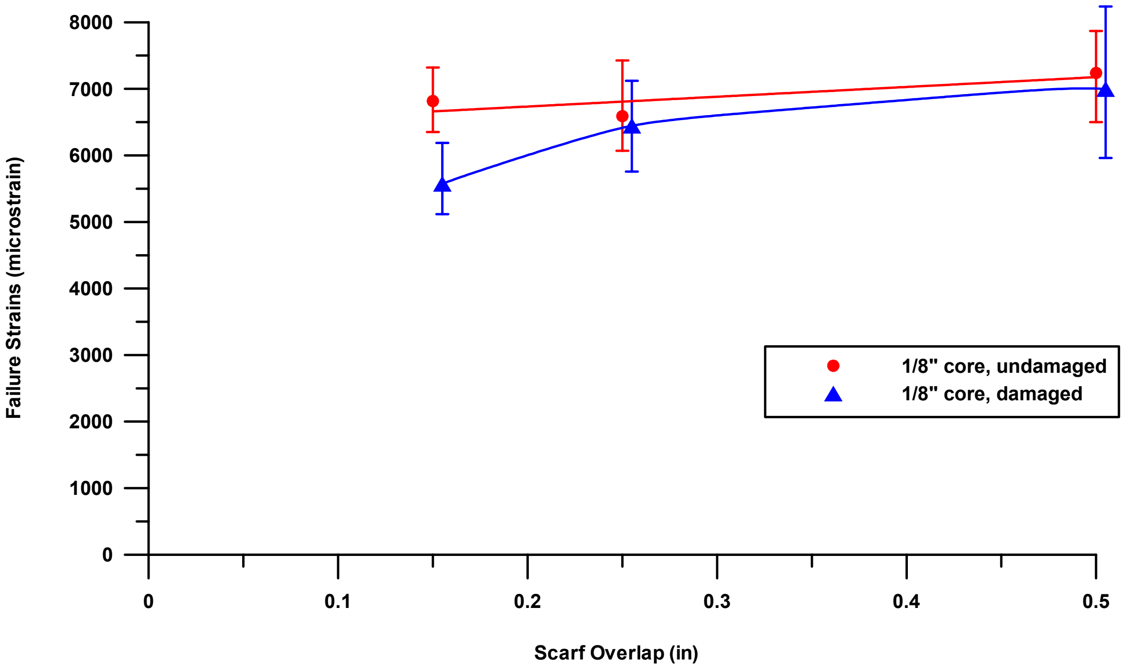

FIGURE 33. EFFECTS OF DAMAGE ON THE FAILURE STRAINS OF 1/8-inch CORE LARGE FOUR-POINT BENDING BEAMS

Nevertheless, the damaged coupons exhibited an overall decrease in strength and strain capacities with respect to the undamaged coupons. As previously mentioned, the damage was inflicted at the taper sand area of the coupons with an energy level of 17 in-lbs to produce a

BVID. The scarf ratio had a noticeable effect on the structural degradation, i.e., the steeper the scarf, the greater the strength and strain reduction. For the 0.15-inch scarf coupons, the drop in strength was about 20%, corresponding to an 18% strain reduction, as measured from the center of the repair. For the 0.25- and 0.50-inch scarf coupons, the strain reduction was less than 5%.

Figure 34 shows the effect of BVID on the strength of the 3/8-inch core, large four-point bending beams. Based on average values, it can be seen that the strength of the undamaged beams changed as a function of scarf overlap. Instead of the expected increase in strength as a function of increasing scarf overlap, as would be the case for a laminate, the opposite was found. For the 0.15- and 0.25-inch scarf ratios, no significant change in failure load was noticed. For the 0.50-inch scarf coupons, there was a significant drop in strength on the order of 30% with respect to the 0.15- and 0.25-inch scarf coupons.

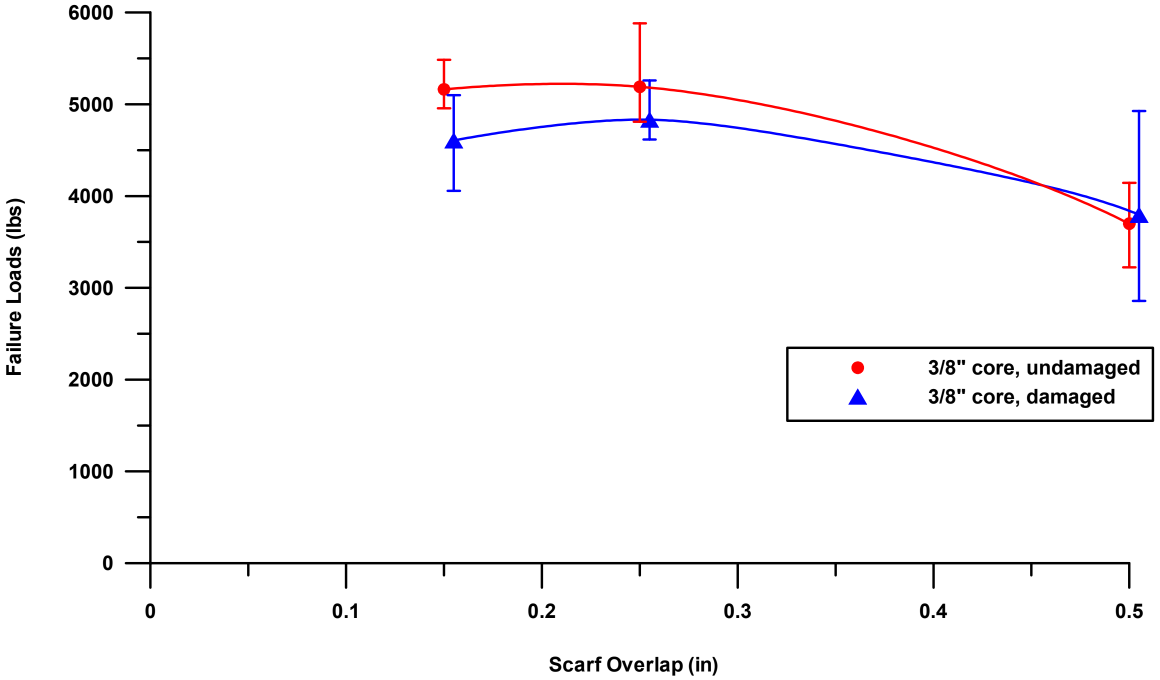

FIGURE 34. EFFECTS OF DAMAGE ON THE FAILURE LOADS OF 3/8-inch CORE LARGE FOUR-POINT BENDING BEAMS

Damaged coupons exhibited the same trend, i.e., for increasing scarf overlaps, there was a decrease in strength of the repaired beams. Based on average values, there was not a significant difference between the strength of 0.15- and 0.25-inch scarf coupons. However, the failure loads of the 0.50-inch scarf beams were 21% lower than the failure loads of the 0.15- and 0.25-inch scarf coupons.

Comparing damaged and undamaged coupons, it can be seen that for the larger scarf overlaps (0.50 inch), there was no significant change in strength based on average values. For the 0.25- and 0.15-inch scarf coupons, respectively, the effects of damage translated as a loss of strength of about 5% and 10%, respectively.

Figure 35 shows the effect of BVID on the strain capacity of the large four-point bending beams with a 3/8-inch core cell size. Based on average values, it can be seen that the strain values for the undamaged beams decreased as a function of increasing scarf overlaps. The recorded failure strains were 6500, 5800, and 4250 microstrain, respectively, for the 0.15-, 0.25-, and 0.50-inch scarf overlaps.

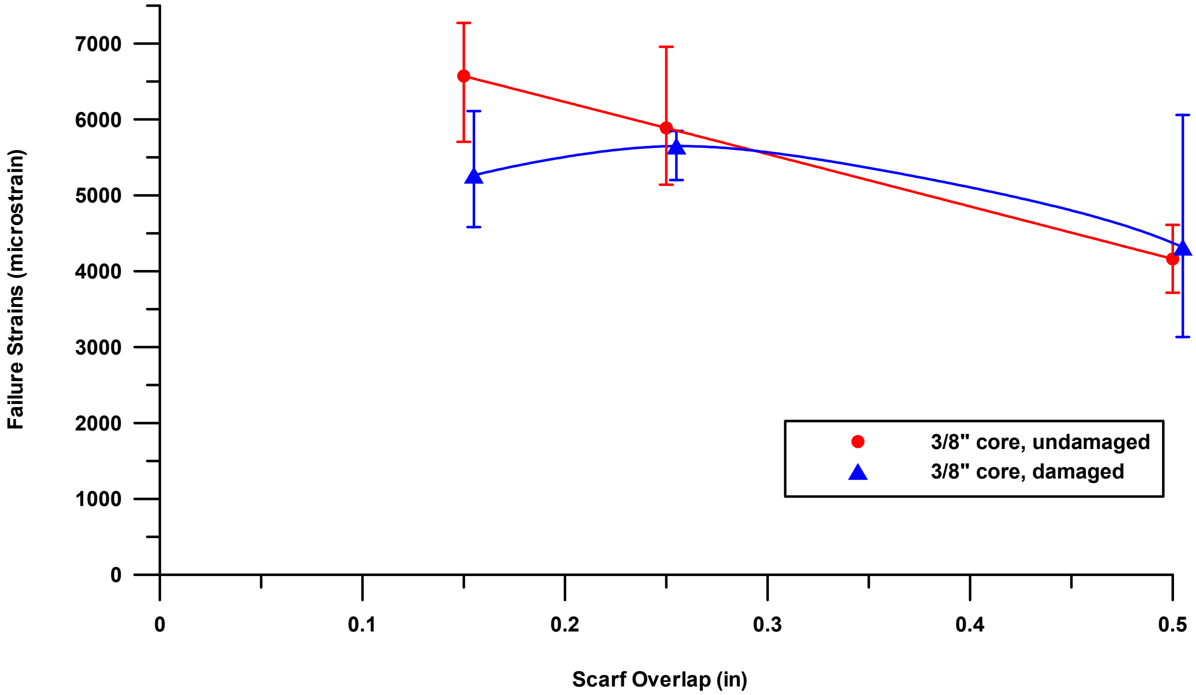

FIGURE 35. EFFECTS OF DAMAGE ON THE FAILURE STRAINS OF 3/8-inch CORE LARGE FOUR-POINT BENDING BEAMS

For the damaged coupons, the highest failure strains were recorded for the 0.25-inch scarf coupons with an average value of 5500 microstrain, followed by the failure strains of the 0.15-inch scarf coupons with a value of 5000 microstrain, and finally, the 0.50-inch scarf coupons with an average value of 4250 microstrain.

Comparing the damaged and undamaged coupons, it was found that damage definitely affected the strain capacity of the coupons: the steeper the scarf, the higher the strain reduction. The damaged 0.15-inch scarf coupons showed a reduction in strain capacity of about 23% with respect to the undamaged coupons, while the strain reduction for the 0.25- and 0.50-inch coupons did not exceed 5%. All of these percent differences are based on average values.

Comparing the effects of core cell size on the strength of the beams, figure 36 shows that the failure loads of the 1/8-inch core coupons were significantly higher than the failure loads of the 3/8-inch core coupons. For the smaller repairs (0.15- and 0.25-inch scarf overlaps), the failure loads of the 3/8-inch core coupons were about 17% lower than the failure loads of the 1/8-inch core coupons. However, for the largest repairs, the strength of the 3/8-inch core coupons was about 40% lower than the strength of the 1/8-inch core coupons. It should be stressed that the only difference between the 1/8- and 3/8-inch core coupons is the core itself; the same materials and processes were used to manufacture the parent and repair structures. This definitely shows the impact of core properties on the performance of a repaired sandwich structure in bending. Under this specific loading mode, a smaller core cell seemed to increase the strength capacity of the repaired structure regardless of the size of the repair.

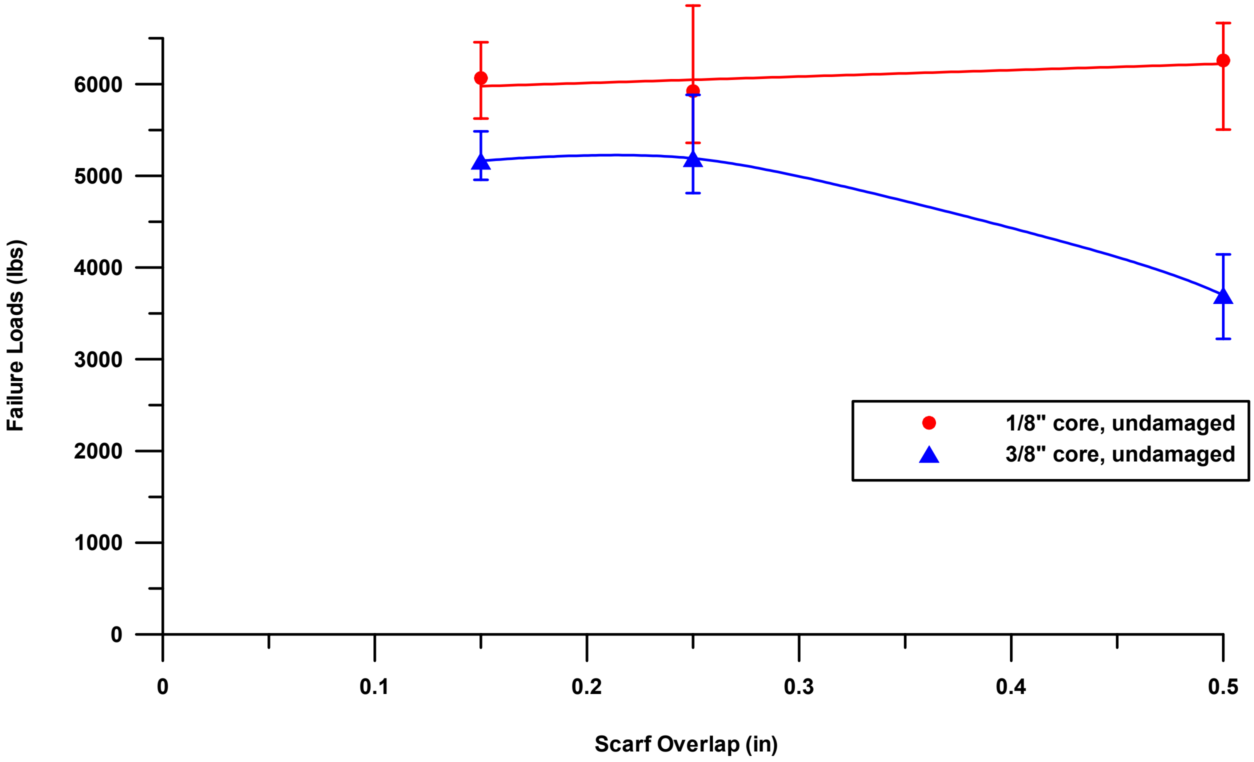

FIGURE 36. EFFECT OF CORE CELL SIZE ON THE FAILURE LOADS OF UNDAMAGED LARGE FOUR-POINT BENDING BEAMS

Comparing the effects of core cell size on the strain capacity of the beams, figure 37 shows that the 1/8-inch core coupons had an overall higher strain capacity than the 3/8-inch core coupons. A slight increase in the strain capacity was recorded for the 1/8-inch core coupons as a function of increasing repair length. A significant reduction in the strain capacity was found for the 3/8-inch core coupons as a function of increasing scarf overlap. In summary, it was found that the larger the repair, the higher the difference in the strain capacity of the 1/8-inch core and the 3/8-inch core coupons. For the 0.15-inch scarf repairs, based on average values, the failure strain was almost the same (about 6500 microstrain). For the 0.25-inch scarf repairs, the failure strains were 6500 and 5750, respectively, for the 1/8- and 3/8-inch cores. Finally, for the largest repair, failure strains were 7000 and 4000, respectively, for the 1/8- and 3/8-inch core coupons.

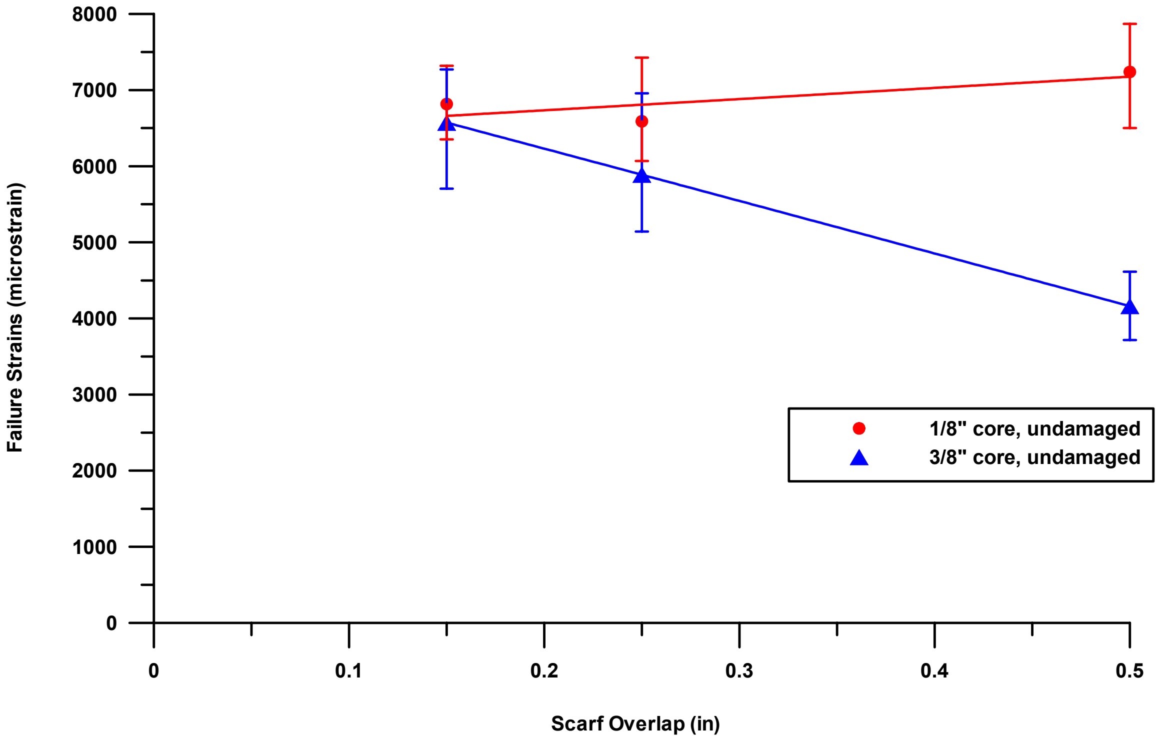

FIGURE 37. EFFECT OF CORE CELL SIZE ON THE FAILURE STRAINS OF UNDAMAGED LARGE FOUR-POINT BENDING BEAMS

Figures 38 and 39 show the effect of core cell size on the strength and strain capacities of the impacted large four-point bending beams. Similar to the results obtained for the undamaged beams, the 1/8-inch core impacted beams had a greater strength and strain capability compared to the 3/8-inch core impacted beams, regardless of the size of the repair used. Furthermore, it was found that the larger the repair, the larger the percent difference in the structural capacity. For the 0.15-inch scarf impacted repairs, it was found that the strain capacity of the 3/8-inch coupons was 9% lower than the strain capacity of the 1/8-inch core coupons. For the 0.50-inch scarf impacted repairs, the strain capacity of the 3/8-inch core coupons was 43% lower than the failure strain of the 1/8-inch core scarf repairs. These percent differences are based on average values.

In addition, an 18% increase in the strength capacity was recorded for the 1/8-inch core impacted beams, as the repair size was increased from a 0.15-inch scarf overlap to a 0.50-inch scarf overlap. This corresponded to a 21% increase in the strain capability between the smallest and the largest repair sizes considered. For the 3/8-inch core beams, a slight increase in strength and strain capability was achieved by using a 0.25-inch scarf overlap repair instead of a 0.15-inch scarf repair. However, a further increase in the size of the repair (0.50-inch scarf overlap) resulted in a dramatic loss in strength and strain capability. The 0.50-inch scarf coupons exhibited a loss of strength of about 22% relative to the strength of the 0.25-inch coupons. The corresponding loss in strain was about 24%.

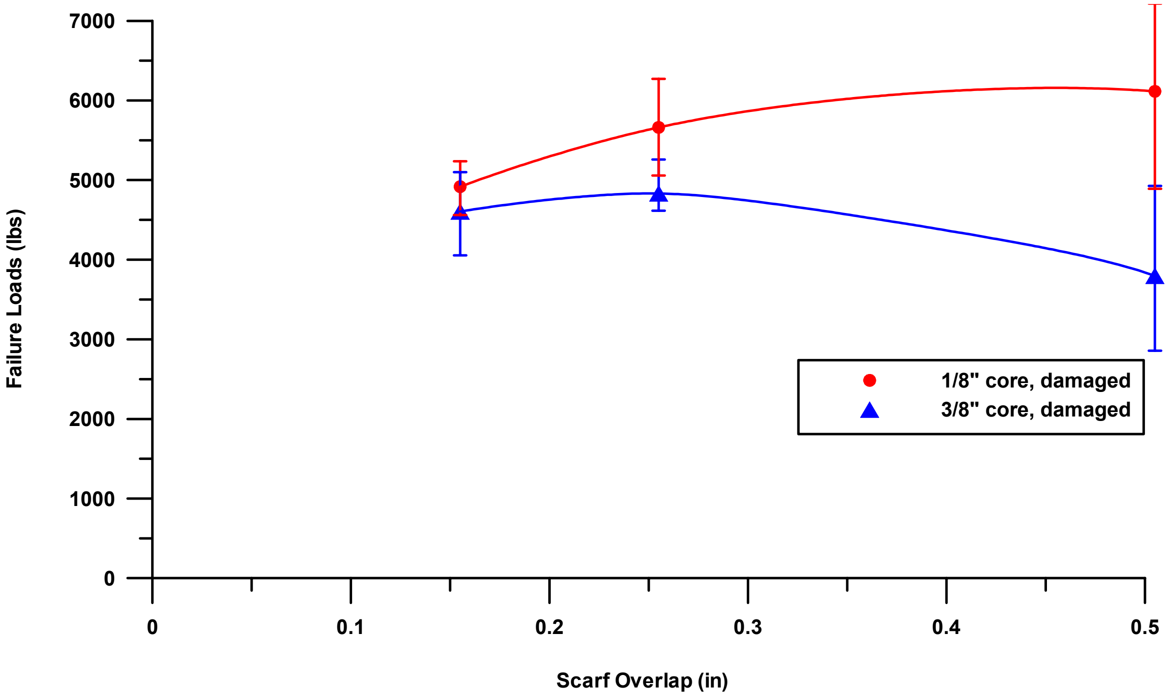

FIGURE 38. EFFECT OF CORE CELL SIZE ON THE FAILURE LOADS OF DAMAGED LARGE FOUR-POINT BENDING BEAMS

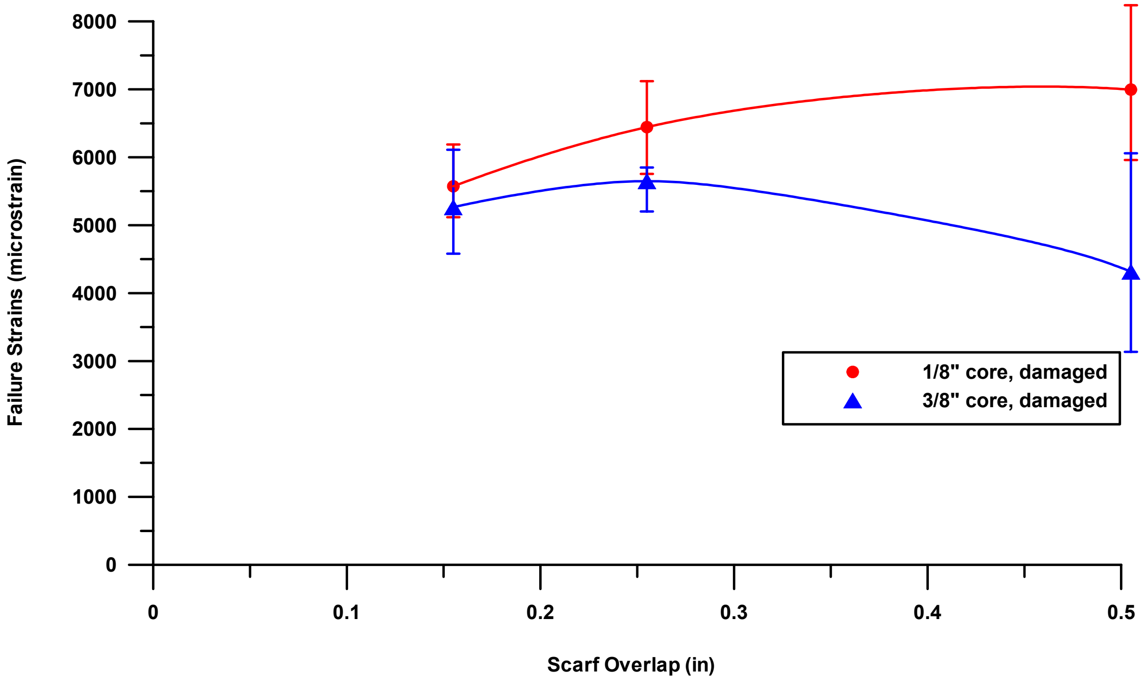

FIGURE 39. EFFECT OF CORE CELL SIZE ON THE FAILURE STRAINS OF DAMAGED LARGE FOUR-POINT BENDING BEAMS

As shown in figure 40, different failure modes were recorded for the large four-point bending beams, depending on the size of the core cell and the damage configuration. For the 3/8-inch core undamaged large four-point bending beams, the main failure mode was at the taper repair area, indicative of a shear failure of the adhesive. All the 3/8-inch core damaged coupons failed through the impact site in the repair laminate.

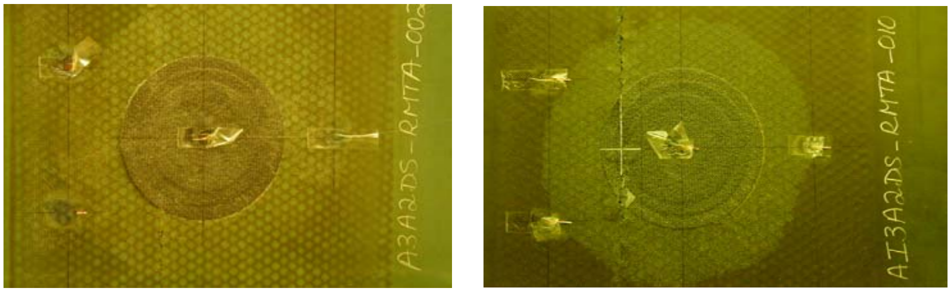

FIGURE 40. FAILURE MODES FOR THE 3/8-inch CORE LARGE FOUR-POINT BENDING BEAMS

For the 1/8-inch core undamaged beams, 50% of the coupons failed in the repair, while the remaining 50% failed outside the repair. For the impacted 1/8-inch core coupons, half of the coupons failed through the impact, while the other half failed outside the repair, as shown in figures 41 and 42.

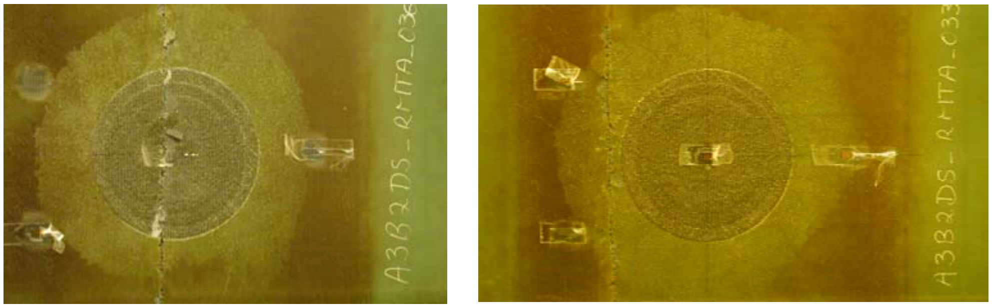

FIGURE 41. FAILURE MODES FOR THE 1/8-inch UNDAMAGED LARGE FOUR-POINT BENDING BEAMS

FIGURE 42. FAILURE MODES FOR THE 1/8-inch CORE IMPACTED LARGE FOUR-POINT BENDING BEAMS

3.3.2 Small Four-Point Bending Beams.

Figures 43 and 44 show the failure loads and strains for the small repaired four-point bending beams with a 3/8-inch core cell size. The repair material used for this case was the Fibercote E765 carbon prepreg, using SIA 795-1 film adhesive (M1 from table 4). The repair material, unlike the material used for the parent structure, was cured at 250°F. It can be seen in figure 43 that regardless of the repair length, i.e., scarf ratio, the average failure load remained the same with a very small scatter in the data. Figure 44 shows that the failure strain at the center of the repair patch increased as the size of the repair scarf overlap was increased. For the 0.15-inch scarf coupons, the strain capacity in the repair was 5000 microstrain. For the 0.25- and 0.50-inch coupons, the strain capacity was 5500 microstrain. Furthermore, regardless of the repair length, the failure strain of the parent structure (i.e., center of the unrepaired facesheet) was about 6000 microstrain.

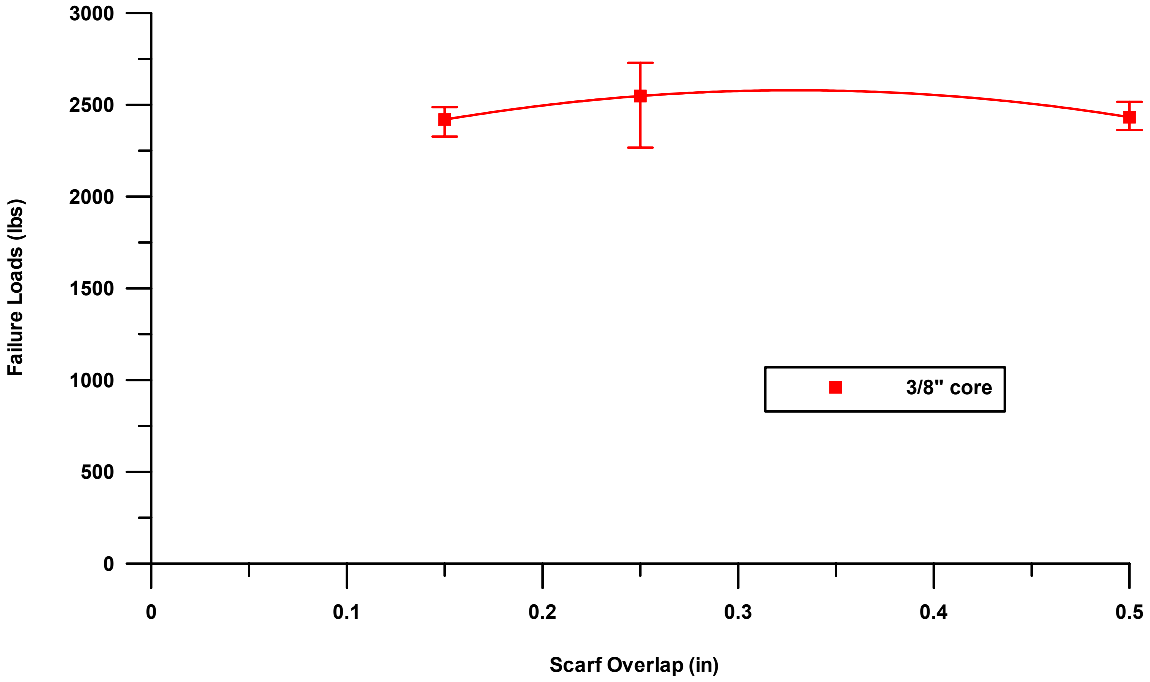

FIGURE 43. FAILURE LOADS FOR THE REPAIRED SMALL FOUR-POINT BENDING BEAMS (M1)

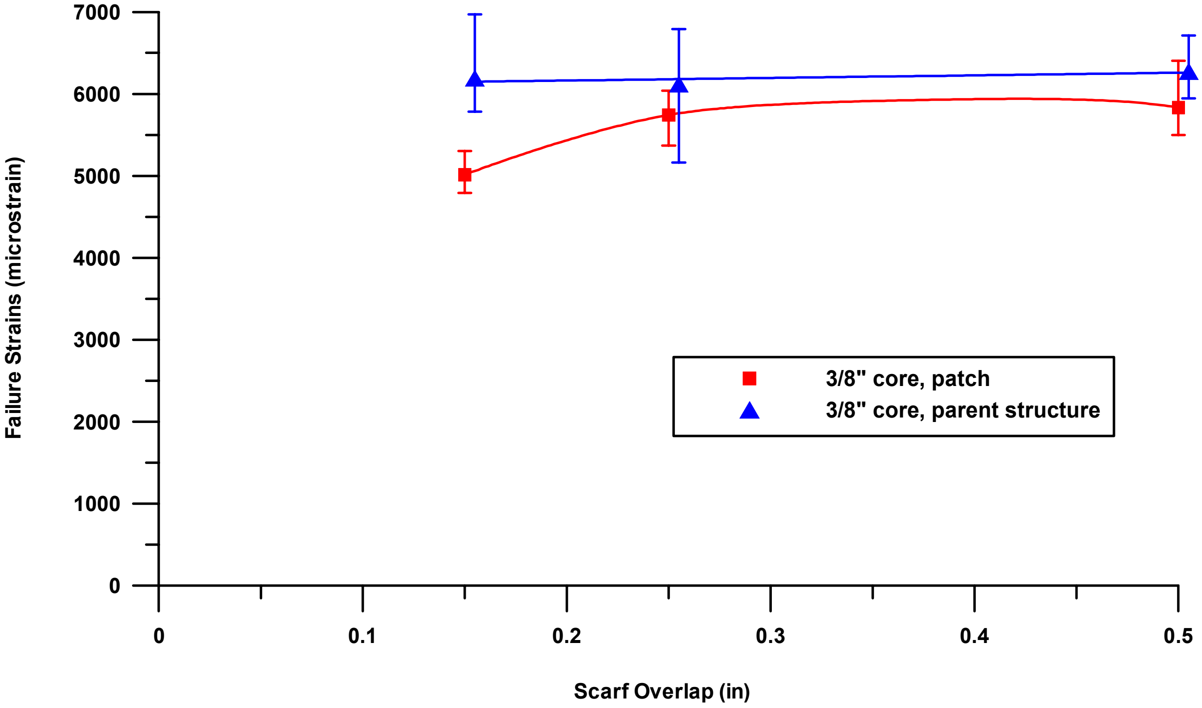

FIGURE 44. FAILURE STRAIN DISTRIBUTION IN THE PATCH AND THE PARENT STRUCTURE FOR SMALL FOUR-POINT BENDING BEAMS (M1)

Figure 45 shows the effects of core cell size on the failure loads of the small four-point bending beams repaired using Cytec BMS9-8, 3K-70-PW cloth with EA9696 adhesive (M2 from table 4) and cured at 250°F. This figure shows that regardless of scarf ratio and core cell size, the ultimate average load for these coupons remained the same. Similar to the trend exhibited by the failure loads, the failure strains remained constant regardless of repair length. However, as shown in figure 46, for the 1/8-inch core coupons, the failure strains in the repair patch reached 10,000 microstrain, whereas for the 3/8-inch core coupons, the failure strains in the repair only reached 8,000 microstrain. These strains were measured at the center of the repair patch. Furthermore, as shown in figure 47, the ultimate strain in the parent structure (center of the unrepaired facesheet) was the same regardless of the repair or core size.

These results show the definite effect of the core cell size on the strain capacity of the laminate. As illustrated in figure 46, the repair laminate can reach strain levels of up to 10,000 microstrain, if a small core cell size is used. With a larger cell, even if the strain capacity of the laminate is very high, the failure strain may not be reached because of the core effects.

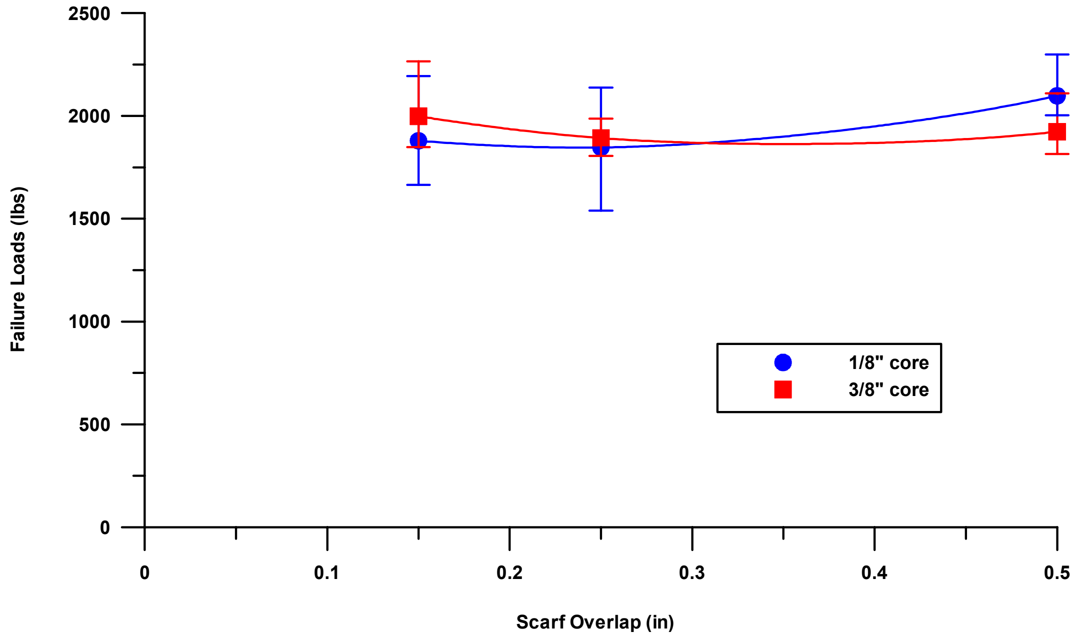

FIGURE 45. FAILURE LOADS FOR REPAIRED SMALL FOUR-POINT BENDING BEAMS (M2)

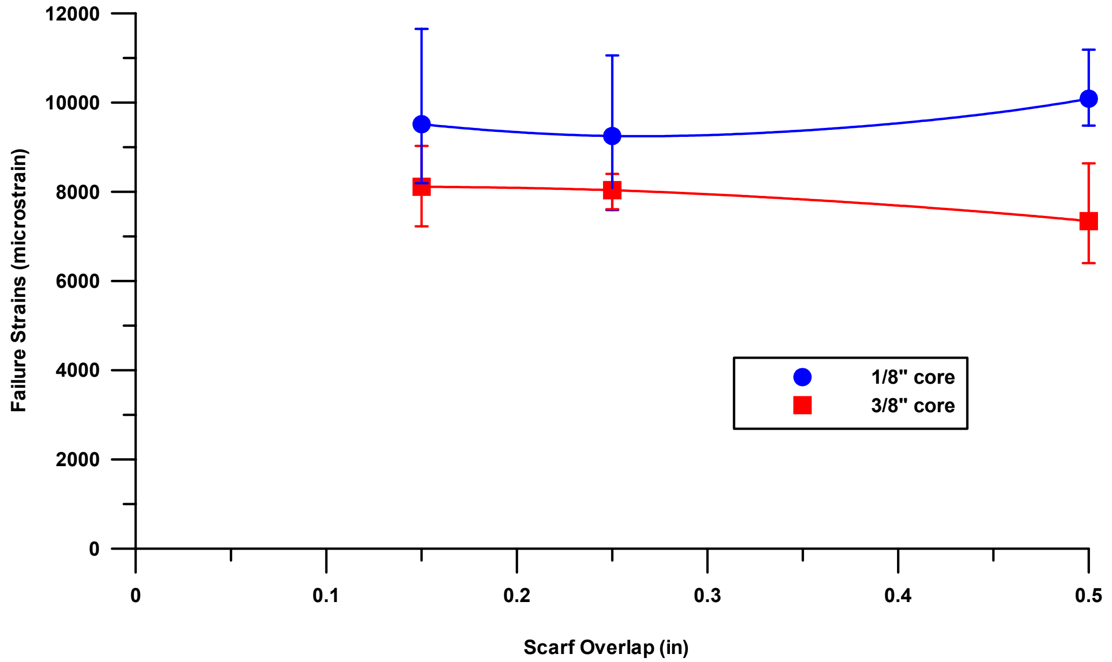

FIGURE 46. FAILURE STRAINS AT THE CENTER OF THE REPAIR FOR SMALL FOUR-POINT BENDING BEAMS (M2)

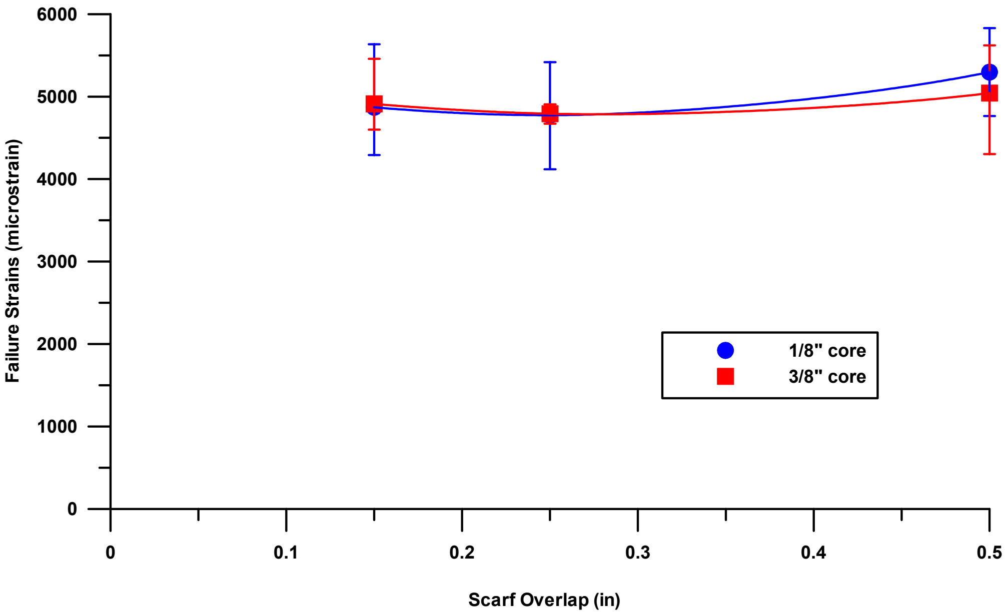

FIGURE 47. FAILURE STRAINS AT THE CENTER OF THE PARENT STRUCTURE FOR REPAIRED SMALL FOUR-POINT BENDING BEAMS (M2)

From the small four-point bending tests performed, two main failure modes were recorded, depending on the repair material system used. All the coupons repaired with the prepreg material system failed in the core, as shown in figure 48. All the small beams repaired with the wet lay-up material system failed in the repair facesheet, as illustrated in this same figure.

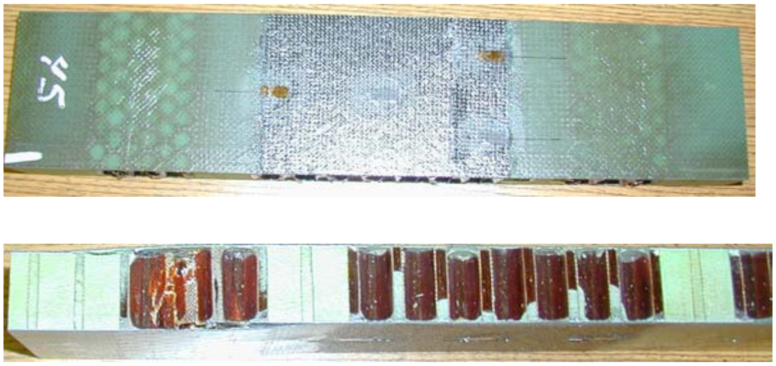

FIGURE 48. SMALL FOUR-POINT BENDING BEAM FAILURE MODES

3.3.3 Unidirectional Tension Coupons.

Figures 49 and 50 show the effects of core cell size on the failure loads and strains of the unidirectional tension coupons repaired with Fibercote E765 carbon prepreg using SIA 795-1 film adhesive. For the 1/8-inch core coupons, results showed an increase in the strength and strain capacity as the repair scarf overlap was increased from 0.15 to 0.25 inch. Using a larger size repair did not provide an increase in the structural capability. The strengths and strains were the same for the 0.25- and 0.50-inch scarf repairs.

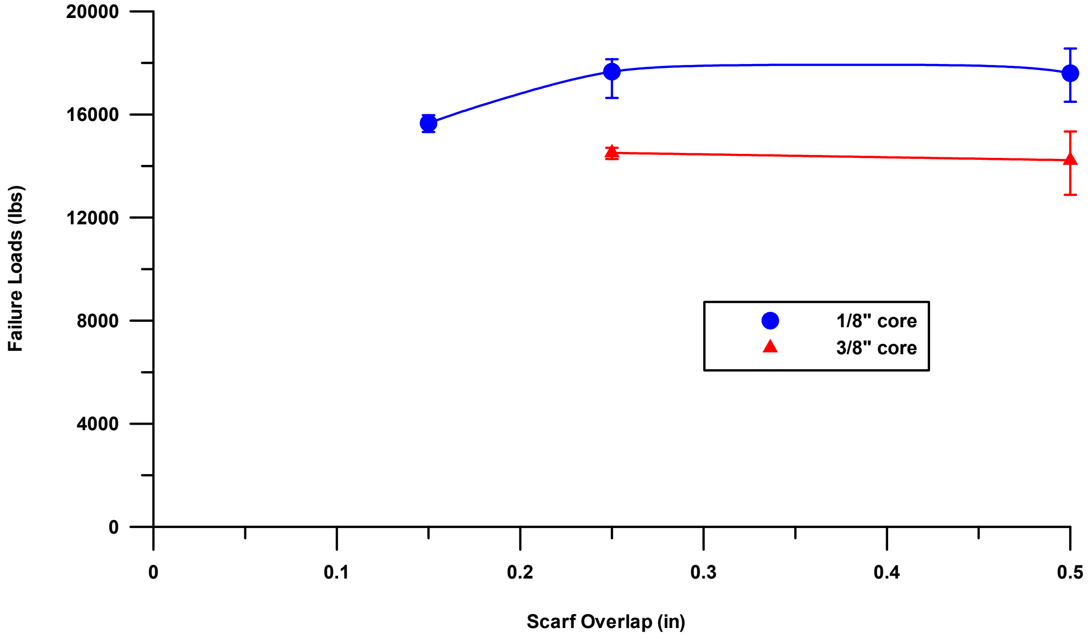

FIGURE 49. EFFECTS OF CORE CELL SIZE ON THE FAILURE LOADS OF REPAIRED UNIDIRECTIONAL TENSION COUPONS (M1)

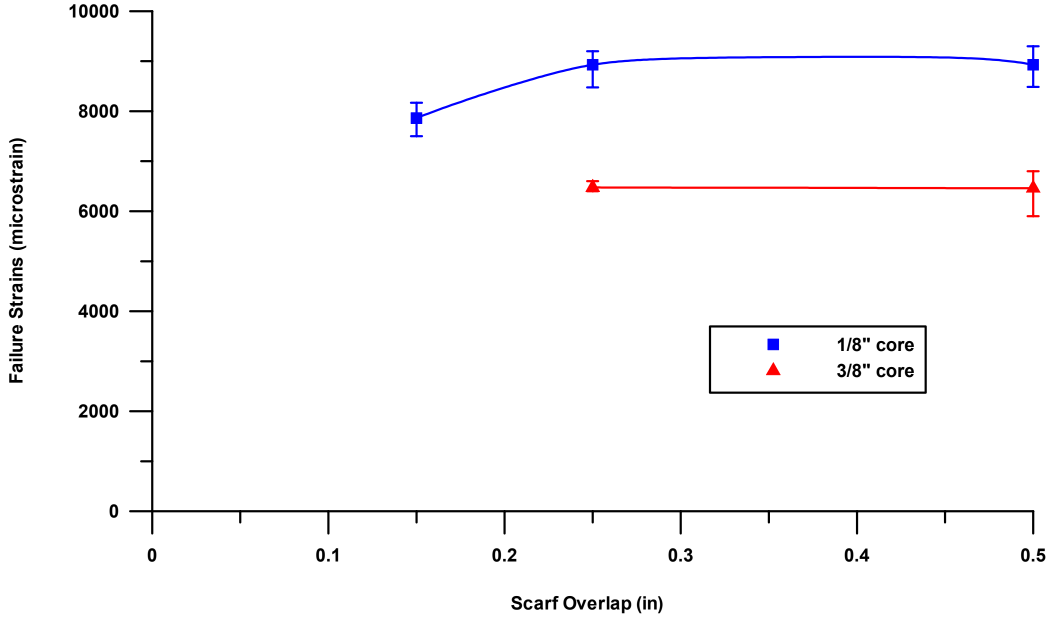

FIGURE 50. EFFECTS OF CORE CELL SIZE ON THE FAILURE STRAINS OF REPAIRED UNIDIRECTIONAL TENSION COUPONS (M1)

For the 3/8-inch core coupons, data was not available for the steepest scarf angle (0.15-inch scarf overlap). However, data for the 0.25- and 0.50-inch scarf overlaps showed no structural improvement or deterioration, i.e., the failure loads and strains remained constant regardless of the size of the repair.

Comparing the performance of the 1/8-inch core unidirectional tension coupons to the 3/8-inch core coupons, it was found that the 1/8-inch core coupons were more structurally capable than the 3/8-inch core coupons. Failure loads and strains of the 1/8-inch core coupons were higher than those of the 3/8-inch core coupons. Strains at failure of the smaller core cell size coupons reached 9000 microstrain, while these strains did not exceed 6500 microstrain for coupons with the larger core cell size. This corresponded to a percent difference of almost 28% with respect to the ultimate strains of the 1/8-inch core coupons. Similarly, the average failure loads for the coupons with the smaller cell size reached 18,000 lbf, whereas coupons with a larger core cell reached ultimate loads of only 14,000 lbf, corresponding to a percent reduction of 22% with respect to the higher loads.

Figure 51 shows the effects of core cell size on the strain distribution in the repaired patch and parent structures. As previously mentioned, it was found that the strain capacity of the 1/8-inch core coupons was larger than the strain capacity of the 3/8-inch core coupons. Furthermore, failure strains in the parent structure (back facesheet) were always higher than strains in the repaired structure. Assuming the load distribution was uniform throughout both facesheets, one can deduce that the repair was slightly stiffer than the parent structure, hence less deformation.

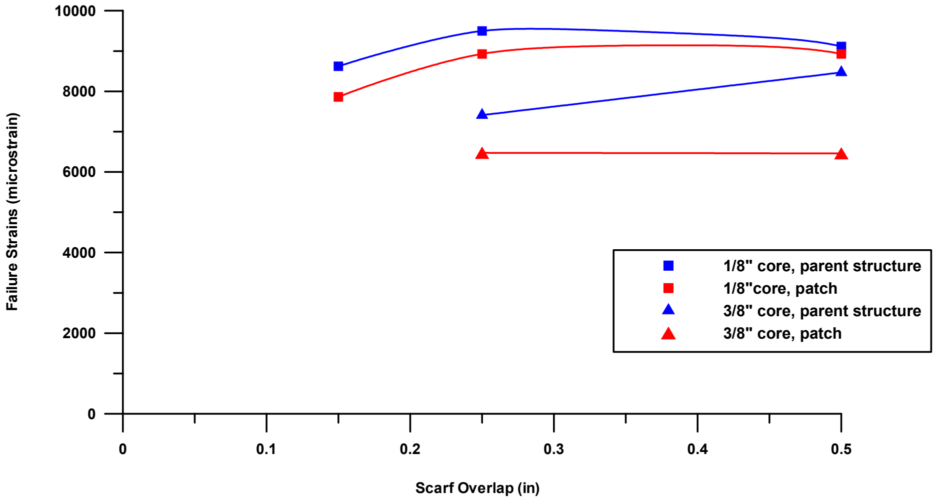

FIGURE 51. EFFECTS OF CORE CELL SIZE ON THE STRAIN DISTRIBUTION IN THE PATCH AND THE PARENT STRUCTURE FOR UNIDIRECTIONAL TENSION COUPONS (M1)

Figure 52 shows the effects of core cell size on the failure loads of the unidirectional tension coupons repaired using Cytec BMS9-8, 3K-70-PW cloth with EA9696 adhesive. For the 1/8-inch core coupons, the 0.15-inch scarf repairs yielded the highest failure loads, whereas the 0.25- and 0.50-inch scarf repairs yielded almost identical average failure loads in the order of 12,000 lbf.

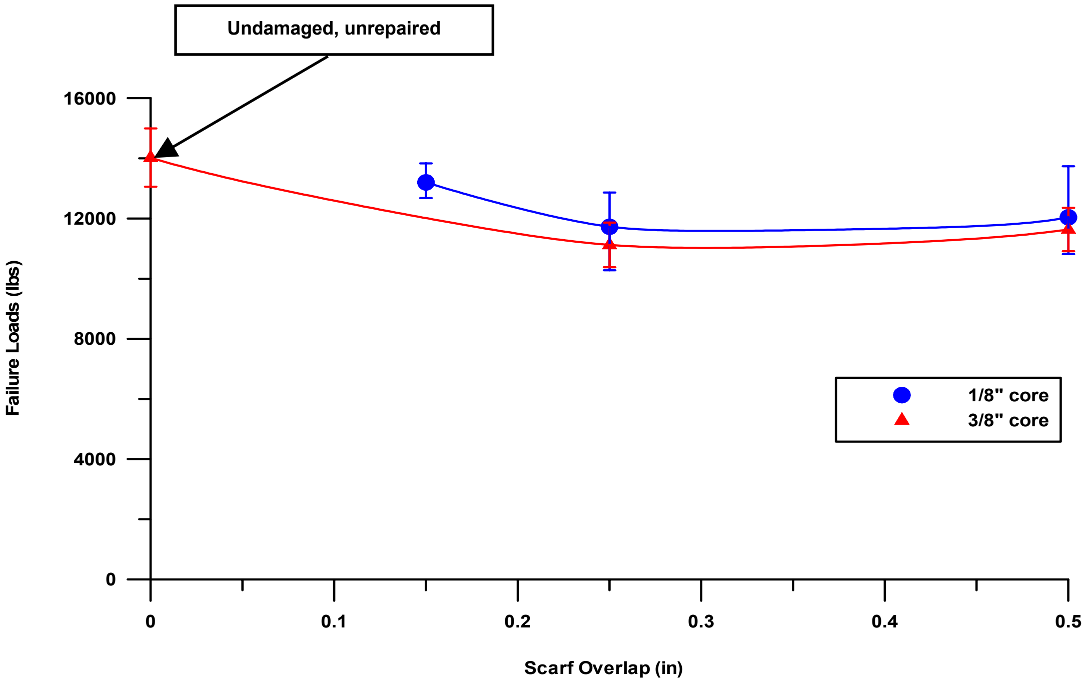

FIGURE 52. EFFECTS OF CORE CELL SIZE ON THE FAILURE LOADS OF REPAIRED UNIDIRECTIONAL TENSION COUPONS (M2)

The 3/8-inch core coupons yielded similar results, with the average failure load of the 0.50-inch scarf coupons being slightly higher than the average failure load of the 0.25-inch scarf coupons. Available data for baseline unrepaired coupons showed that the average undamaged/unrepaired strength was slightly higher than the average repaired strength for both scarf overlaps considered.

Comparing the performance of the 1/8-inch core coupons to the 3/8-inch core coupons, it was found that the 1/8-inch core coupons yielded failure loads slightly higher than those of the 3/8-inch core coupons.

Figure 53 shows the effects of core cell size on the strain capacity of the repaired structure. The strains at failure of the 3/8-inch core coupons remained constant, regardless of the repair configuration. For the 1/8-inch core coupons, the 0.15-inch scarf overlap coupons showed the highest strain capability, whereas the 0.25- and 0.50-inch scarf coupons had almost the same strains at failure. Comparing the performance of the 1/8-inch core versus the 3/8-inch core coupons, those with a smaller core cell size showed a higher strain capability. As illustrated in figure 53, using a 3/8-inch core results in a reduction in the strain capacity of the structure by 25%.

Figure 54 shows a comparison between the strain distribution in the repaired patch (front facesheet) and the parent structure (back facesheet) for the two different core cell sizes considered. For the larger core cell size, failure strains were exactly the same for the patch and the parent. However, for the smaller core cell size, strains at failure in the center of the patch were as much as 45% higher than strains at failure in the center of the parent structure.

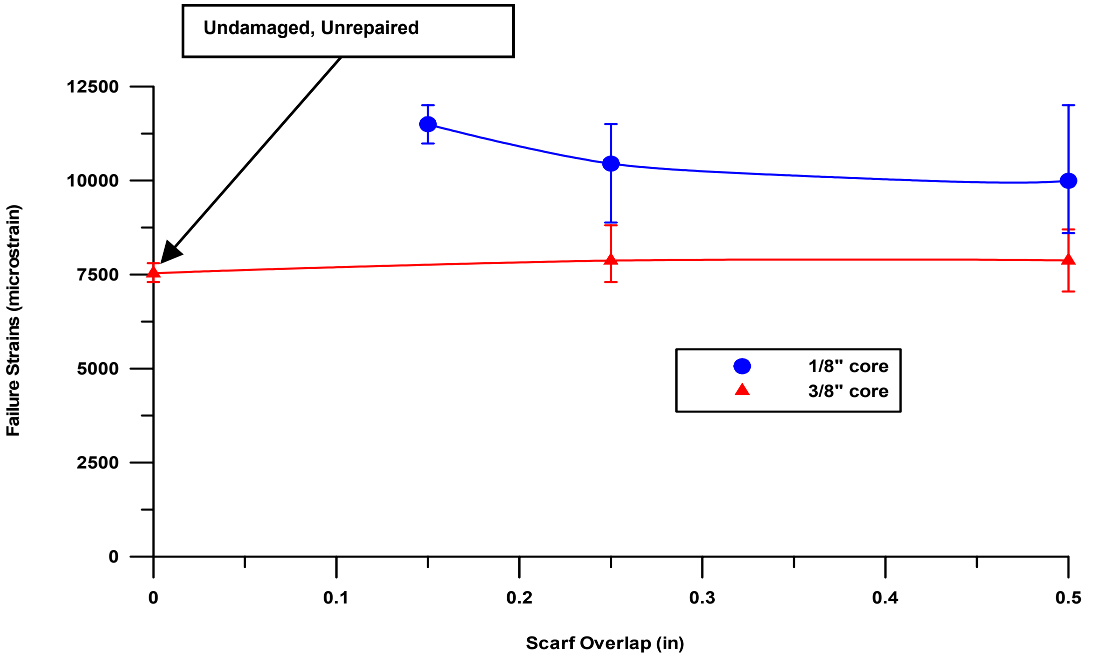

FIGURE 53. EFFECTS OF CORE CELL SIZE ON THE FAILURE STRAINS AT THE CENTER OF THE PATCH FOR UNIDIRECTIONAL TENSION COUPONS (M2)

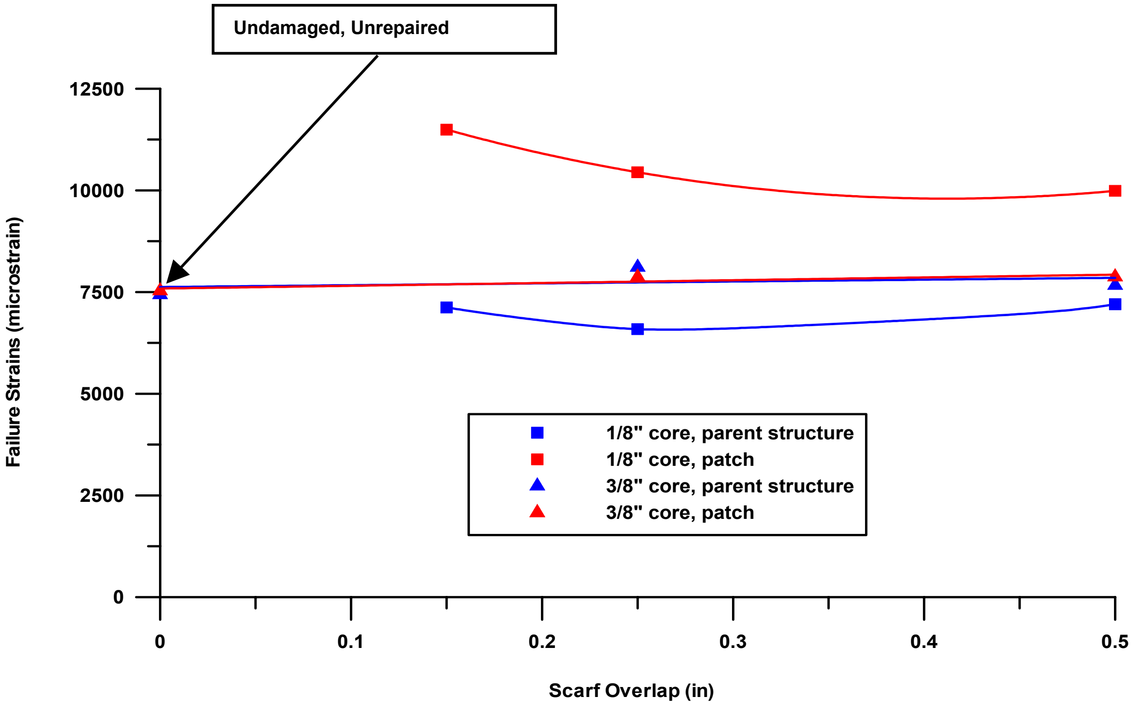

FIGURE 54. EFFECTS OF CORE CELL SIZE ON THE STRAIN DISTRIBUTION IN THE PATCH AND THE PARENT STRUCTURE FOR UNIDIRECTIONAL TENSION COUPONS (M2)

All the tension coupons failed in the repair laminate in the taper repair area, i.e., in the sloped region where the repair meets the parent structure. Example pictures of the failure modes of these coupons are shown in figure 55.

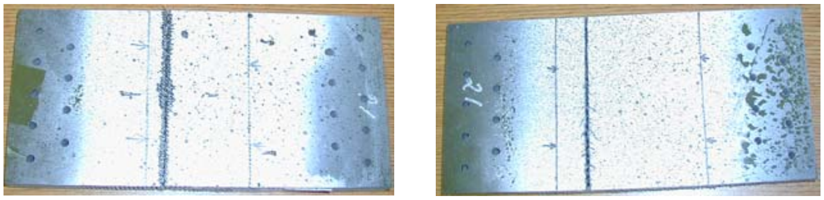

FIGURE 55. UNIDIRECTIONAL TENSION COUPON FAILURE MODES

3.4 DISCUSSION.

The most prominent conclusion that could be deduced from the repair variable investigation was the major impact that the core properties have on the performance of a sandwich structure with the same parent and repair materials, more specifically, the core cell size. From the results obtained, it was found that the 1/8-inch core coupons had a higher strain capacity than the 3/8-inch core coupons. The 1/8-inch core coupons have a larger bond interface area than the 3/8-inch core coupons because the cell sizes are smaller, i.e., the bonded core area is larger, therefore, the smaller the cell, the higher the strain capacity, assuming the same facesheet materials are used [9].

Furthermore, excluding the 3/8-inch core beams, it was found that the 0.25- and 0.50-inch scarf repairs usually had the same strength and strain capacity, with the 0.50-inch scarf repairs having a slightly better performance when the 1/8-inch core was used. Therefore, instead of using the traditional 0.50-inch scarf overlap, one could use a 0.25-inch scarf overlap and achieve comparable results.

The results obtained for the 0.15-inch scarf overlap were not 100% conclusive. In some cases the 0.15-inch scarf repairs performed better than the other repairs. In other cases, however, especially when damage was involved, this particular scarf repair exhibited a substantial decrease in the strength and strain capacity with respect to the other scarf ratios: the steeper the scarf, the higher the stress concentrations in the adhesive bondline, which explains the behavior of the 0.15-inch scarf repairs. With an already highly stressed bondline, damage in the taper repair area further increases stresses in the adhesive for the 0.15-inch scarf repairs, thus causing an acceleration of the failure initiation of these coupons.

4. REPAIR ANALYSIS EVALUATION.

4.1 ADHESIVE CHARACTERIZATION USING ASTM D 5656.

The stress-strain properties of different adhesives used in this study were obtained for the analytical model evaluation. The standard method used for this testing was ASTM D 5656 [10], Thick-Adherend Metal Lap-Shear Joints for Determination of the Stress-Strain Behavior of Adhesives in Shear by Tension Loading. This method used thick adherend lap-shear specimens loaded in tension while the adhesive undergoes shear loading.

Table 5 summarizes the strength and corresponding initial shear modulus values obtained for the two film adhesives used in this study. Examples of stress-strain curves obtained are shown in figures 56 and 58. Figures 57 and 59 show the region of these curves used to calculate the corresponding initial shear modulus of the adhesives.

TABLE 5. ASTM D 5656 THICK-ADHEREND TEST RESULTS

Adhesive	Bondline Thickness (in)	Number of Coupons Tested	Average Shear Strength (psi)	Average Shear Modulus (Msi)	Failure Modes
Cytec FM 377S Film Adhesive	0.005	6	7,506	0.12	at least 85% cohesive
SIA 795-1 Film Adhesive	0.005	3	5,965	0.057	80%-90% cohesive

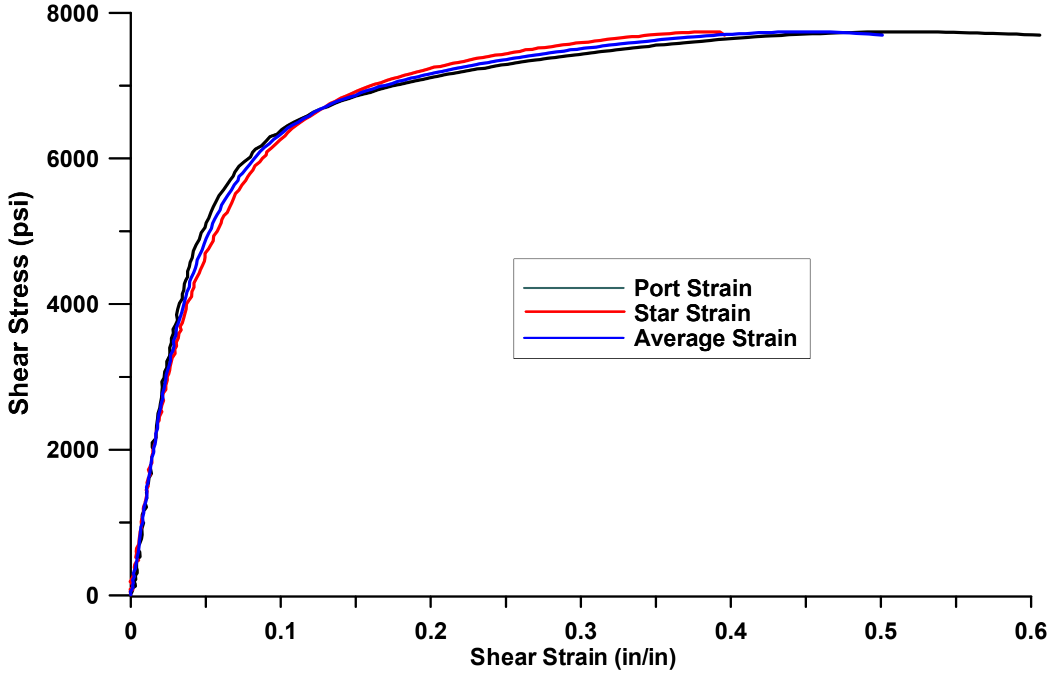

FIGURE 56. SHEAR STRESS-STRAIN CURVES OBTAINED FOR FM 377S ADHESIVE

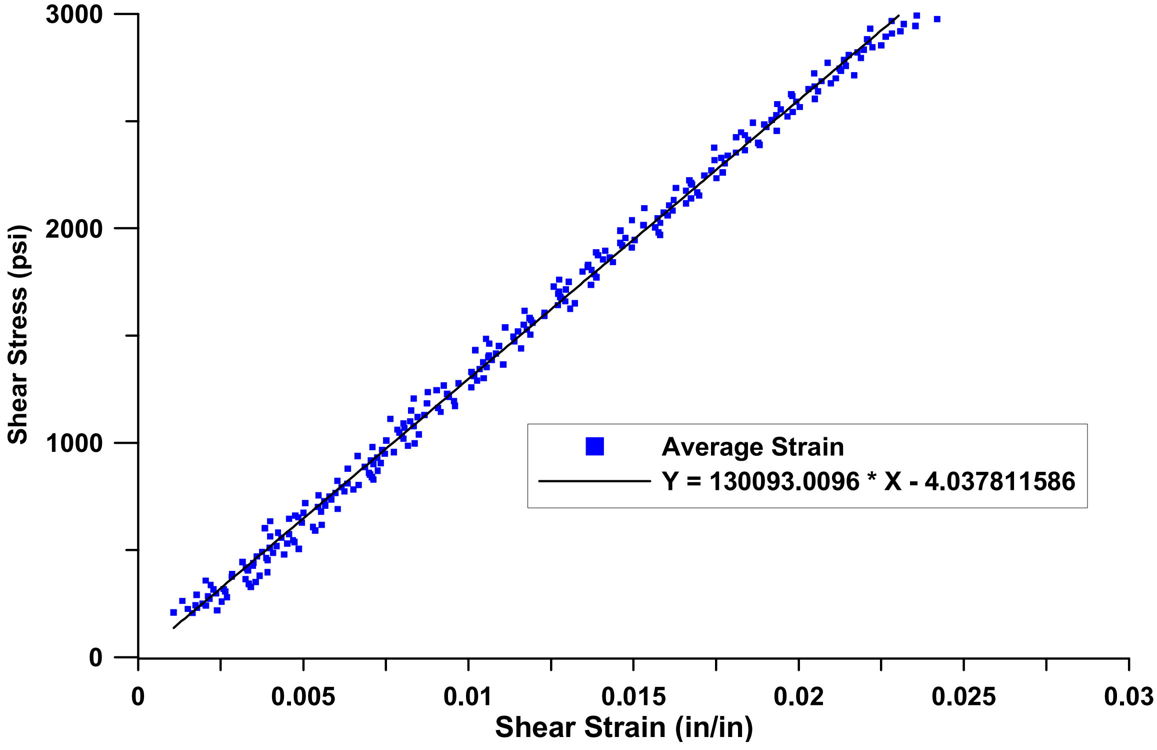

FIGURE 57. SHEAR MODULUS OBTAINED FOR FM 377S ADHESIVE

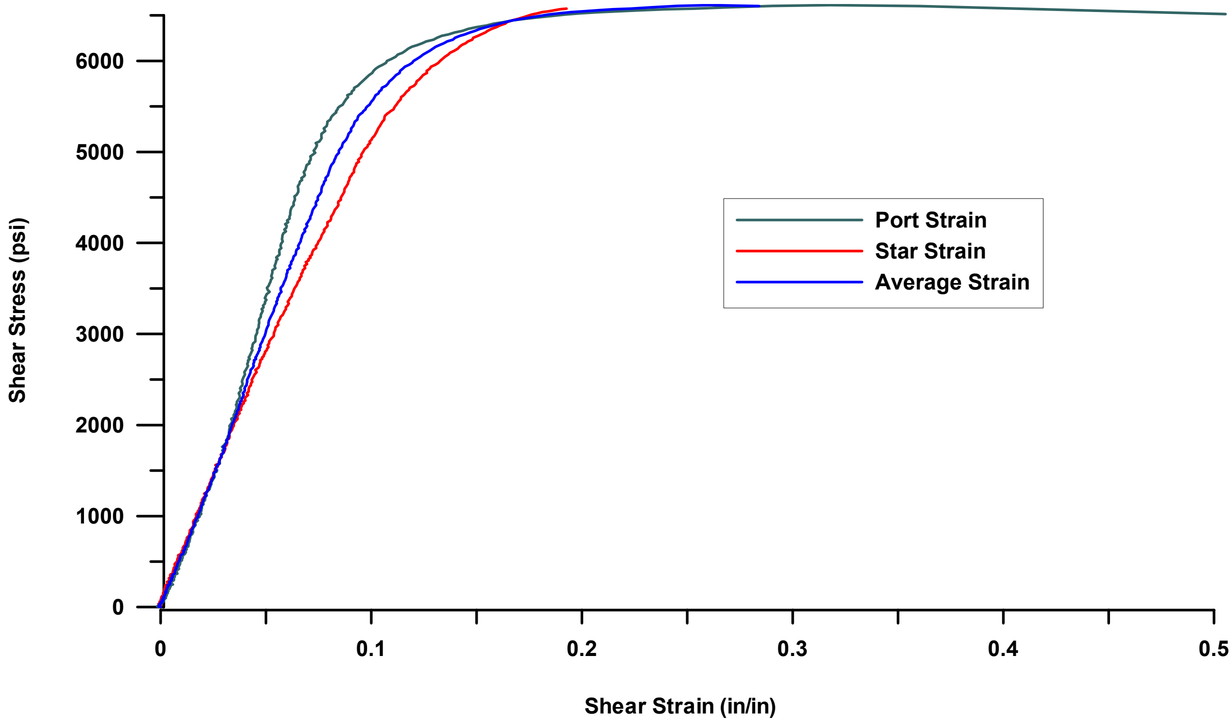

FIGURE 58. SHEAR STRESS-STRAIN CURVES OBTAINED FOR SIA 795-1 ADHESIVE

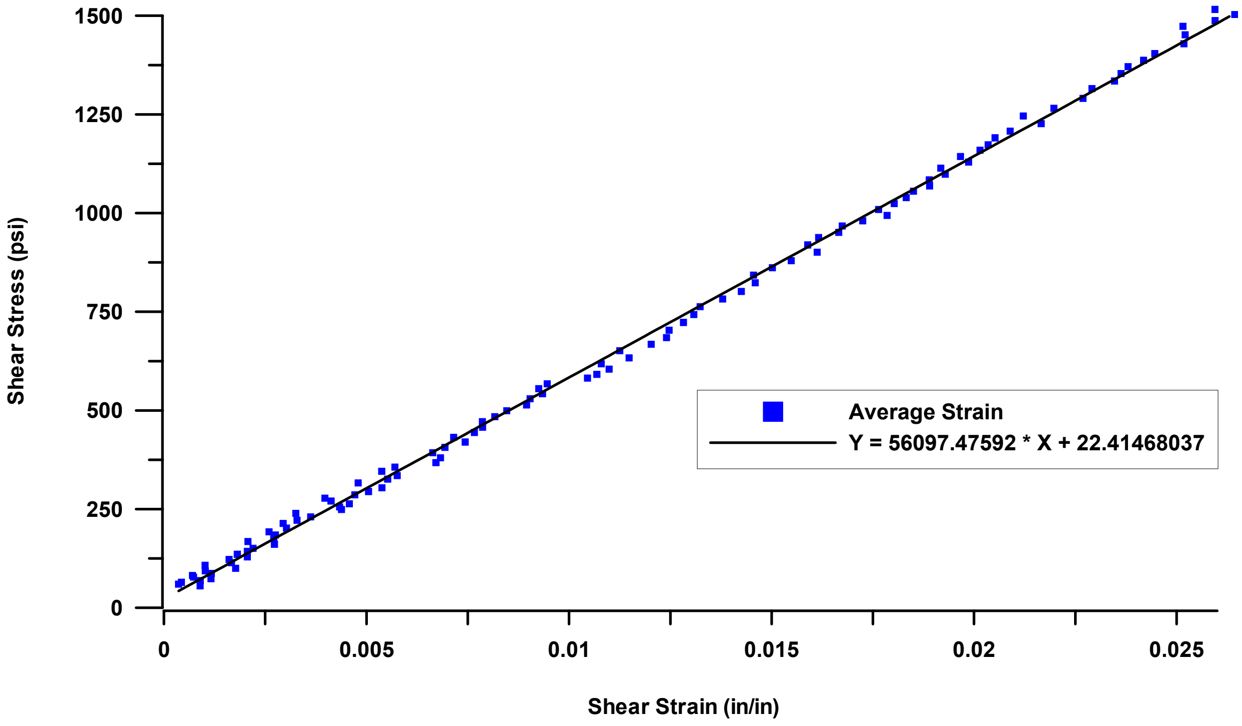

FIGURE 59. SHEAR MODULUS OBTAINED FOR SIA 795-1 ADHESIVE

4.2 ANALYTICAL MODELS.

As previously mentioned, several factors must be considered when designing a repair to an aircraft composite sandwich structure. While it is necessary to implement the repair quickly, it is crucial to have accurate and reliable analysis tools to design the repair and assign proper inspection intervals to the repaired structure.

A large selection of analysis tools to evaluate repairs at the laminate and joint levels is available in the literature. Several computer codes have been developed for that purpose and are currently used at commercial airline depots or United States (U.S.) Air Force Logistic Centers. However, for the repair engineer, not every model is suitable. A survey was conducted at five major U.S. Air Force Logistics Centers, where repair engineers and technicians were asked to establish a set of criteria to evaluate repair analysis tools [11].

In evaluating these tools, the criteria that engineers considered essential for a successful repair design and analysis were

- User-friendliness
- Accurate crack growth and damage growth predictions
- Reliable residual strength values for the repaired component
- Repair moisture absorption and thermal mismatch between adherends accounted for
- Reliable complex geometry analysis

Several repair analysis tools with a description of their usage and capabilities follow.

4.2.1 Advanced Composites Repair Analysis Tool.

The main purpose of the Advanced Composites Repair Analysis Tool (ACRAT) program was to provide reliable tools for U.S. Air Force structural engineers to design and analyze repairs and to improve the maintainability and structural integrity of those repairs. This program was developed by BDM as the main contractor and MSC/PDA as the subcontractor [11].

The ACRAT repair analysis system uses a combination of commercial softwares such as MSC/PDA's M/Vision and P3/Patran to guide the engineer step by step through the analysis process. The M/Vision software provides all the necessary data needed for analysis. This includes a detailed geometry, material properties, design allowables, load, etc. The finite element analysis is then performed using P3/Patran. This program has an extensive database that contains the information necessary to design and analyze a repair.

ACRAT, however, has some limitations. It is not quite user-friendly, and it is more suitable to Unix users. Furthermore, it does not have the capability of predicting crack growth and damage growth rates in the repaired structure. Finally, the system is unable to determine the residual strength and the inspection requirements of the repaired components.

4.2.2 Scarf Joint Analysis Customized System.

This analytical tool was developed by Kawasaki Heavy Industries in conjunction with the CACRC analytical task group. It allows the user to perform a detailed finite element analysis of the bonded repair without requiring a thorough knowledge of the finite element method (FEM). The system guides the user step by step to build an accurate FEM model of the physical problem capable of generating reliable results in a short amount of time [12]. Furthermore, the system is capable of modeling both one- and two-dimensional repairs.

The one-dimensional repair model is based on an American Institute of Aeronautics and Astronautics paper published in 1984 [13], which models a variety of adhesive-bonded joints using a simple affordable FEM. This method predicts the peel and shear stresses in the adhesive bondline and shows a good correlation with the results obtained using classic methods or numerical methods such as Hart-Smith's analysis [14].

A series of spring elements oriented in the shear and peel (normal) directions is used to model the adhesive. The stiffness of each spring element is the actual stiffness of the adhesive volume it represents. Beam elements are used to model the adherends when the load applied is uniaxial, and shell elements are used when the load applied is biaxial [13]. The material properties given to these elements are the values of the actual adherends they represent. The choice of elements is crucial in finite element analysis. Using spring elements for the adhesive and shell or bar elements for the adherends has an advantage over using solid elements. The key in using solid elements is to always keep a reasonable aspect ratio, which can lead to an increased size of the model. Using spring, bar, or shell elements removes this problem.

The input data necessary to run this FEM is shown in figures 60 and 61.

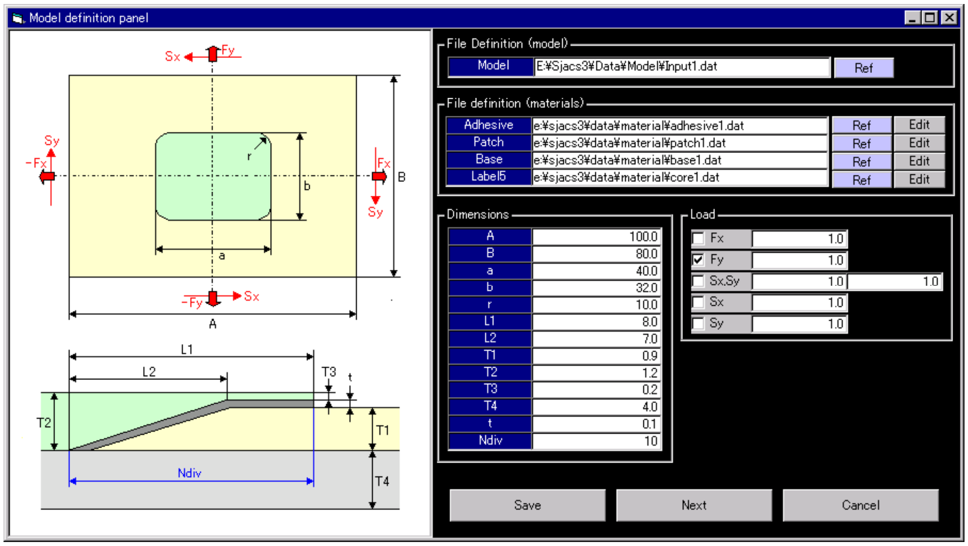

File Definition (model)

Model: E:¥Sjacs3¥Data¥Model¥Input1.dat

File definition (materials)

Adhesive	e:¥sjacs3¥data¥material¥adhesive1.dat
Patch	e:¥sjacs3¥data¥material¥patch1.dat
Base	e:¥sjacs3¥data¥material¥base1.dat
Label5	e:¥sjacs3¥data¥material¥core1.dat

Dimensions

A	100.0
B	80.0
a	40.0
b	32.0
r	10.0
L1	8.0
L2	7.0
T1	0.9
T2	1.2
T3	0.2
T4	4.0
t	0.1
Ndiv	10

Load

☐ Fx	1.0	
☑ Fy	1.0	
☐ Sx,Sy	1.0	1.0
☐ Sx	1.0	
☐ Sy	1.0	

FIGURE 60. INPUT DATA NECESSARY FOR TWO-DIMENSIONAL FEM ANALYSIS
(Courtesy of Kawasaki Industries)

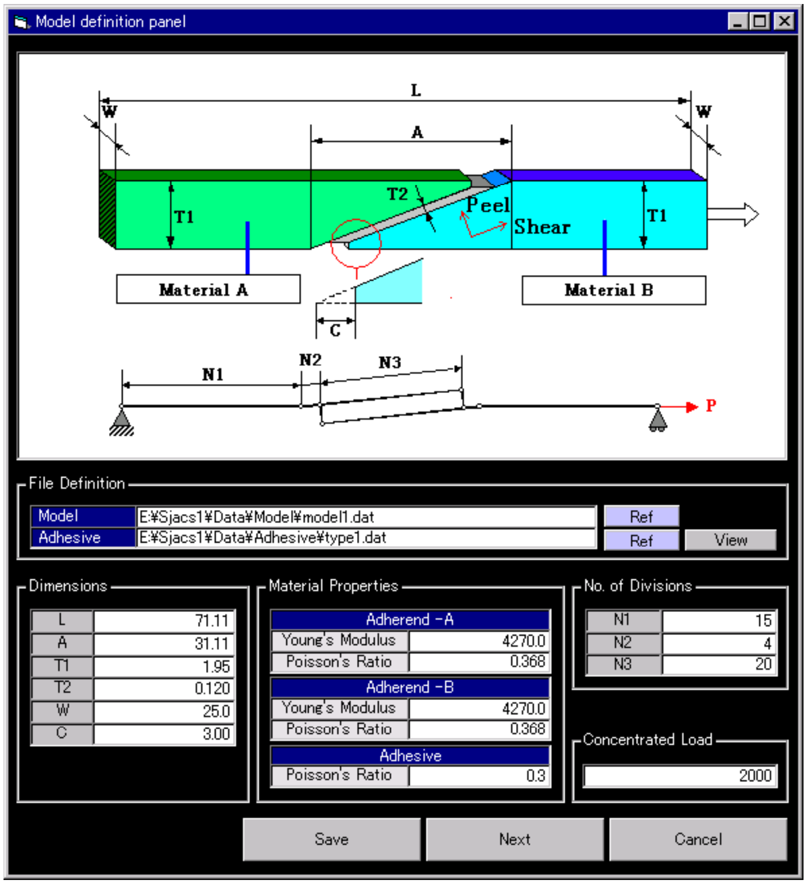

File Definition

Model	E:¥Sjacs1¥Data¥Model¥model1.dat
Adhesive	E:¥Sjacs1¥Data¥Adhesive¥type1.dat

Dimensions

L	71.11
A	31.11
T1	1.95
T2	0.120
W	25.0
C	3.00

Material Properties

Adherend -A	
Young's Modulus	4270.0
Poisson's Ratio	0.368
Adherend -B	
Young's Modulus	4270.0
Poisson's Ratio	0.368
Adhesive	
Poisson's Ratio	0.3

No. of Divisions

N1	15
N2	4
N3	20

Concentrated Load: 2000

FIGURE 61. INPUT DATA NECESSARY FOR ONE-DIMENSIONAL FEM ANALYSIS
(Courtesy of Kawasaki Industries)

4.2.3 Materials Science Corporation SUBLAM Program.

This structural analysis program uses plate theory to predict failure based on the interlaminate stresses in a composite structure. It can only be used for problems with a constant cross section in the x direction. Therefore, modeling in SUBLAM is restricted to two-dimensional problems and can be compared to a two-dimensional finite element model. The choice of elements in SUBLAM, unlike in FEM modeling, is solely driven by the geometry. Furthermore, elements can contain several sublaminates, which in turn will determine the number of nodes of the element. The main assumption in sublaminate analysis is that the displacement field is continuous through the thickness of the sublaminate [15]. A laminate is usually composed of one or several elements, which in turn contain one or a number of sublaminates stacked together with the same boundary conditions between two adjacent plies, i.e., the same displacements and traction forces.

The SUBLAM user first creates an input file describing the model in detail. When this file is executed, a number of output files are generated listing information about the deformed model, which can be visualized using Mathematica. The input file contains all the data necessary to run the analysis. This data consists of material properties, laminate lay-up schedule, element definition, force and displacement boundary conditions, etc. Output files contain tabulated data listing all the details of the deformed model, including values of displacements, stresses, and strains as a function of spatial position. For a stepped or a sloped (scarf) adhesive joint, SUBLAM calculates the average shear and peel stresses in the adhesive that can be used to determine the onset of failure. If failure occurred in the facesheet instead of the adhesive bondline, stresses and strains in the laminate can be plotted to determine the onset of failure.

4.2.4 Classical Laminated Plate Theory.

The Classical Laminated Plate Theory (CLPT) is used to evaluate properties of the repaired composite structure at the laminate level. The parent laminate is analyzed first to determine the structure's original capability. The repair is then evaluated by comparing its stiffness and strength with that of the original structure [16]. As previously mentioned, the stiffness of the repair should be matched as closely as possible to the stiffness of the original structure, and a positive strength margin of safety should be achieved.

To perform this analysis, the number of plies in the laminate as well as their orientation and mechanical properties should be known. The mechanical properties required include modulus of elasticity in the axial and transverse directions for both tensile and compressive loadings (E_{11}, E_{22}, $-E_{11}$, and $-E_{22}$), shear modulus (G_{12}), Poisson's ratio in the axial and transverse directions (υ_{12} and υ_{21}), and material allowable strains for axial, transverse, and shear directions for both tensile and compressive forces (ε_{11}, ε_{22}, γ_{12}, $-\varepsilon_{11}$, $-\varepsilon_{22}$, and $-\gamma_{12}$). If there is a difference in the coefficients of thermal expansion or the moisture coefficients between the repair and the parent structures, these coefficients (CTE_{11}, CTE_{22}, CTM_{11}, and CTM_{22}) will be needed.

For a wet lay-up repair, all the mechanical properties mentioned are needed for both the resin system and the dry fibers independently.

The underlying assumptions behind the CLPT are the following:

- The thickness of the laminate is very small compared to the other dimensions; therefore, shear stresses through the thickness are negligible.
- The plane sections remain plane, and therefore, the in-plane strain distribution through the thickness is linear.
- The laminate is under a state of plane stress where $\sigma_z = 0$.

The generalized Hooke's Law applied to a lamina in local coordinates, shown in figure 62, can be expressed as follows [17].

$$\varepsilon_{11} = \frac{\sigma_{11}}{E_{11}} - \frac{\upsilon_{21}\sigma_{22}}{E_{22}} \tag{1}$$

$$\varepsilon_{22} = -\frac{\upsilon_{12}\sigma_{11}}{E_{11}} + \frac{\sigma_{22}}{E_{22}} \tag{2}$$

$$\gamma_{12} = \frac{\tau_{12}}{G_{12}} \tag{3}$$

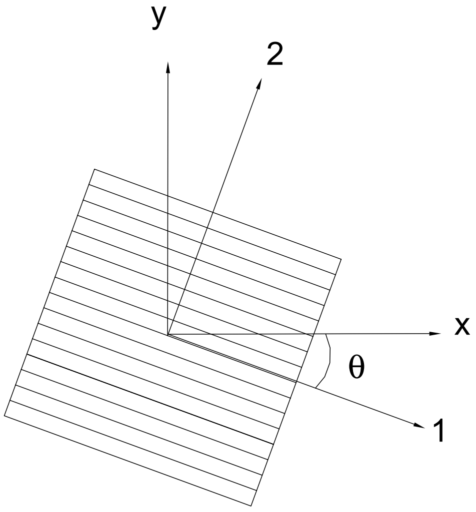

FIGURE 62. LAMINA LOCAL (1-2) AND GLOBAL (x y) COORDINATES

As shown in figure 62, in local coordinates, 1 represents the direction along the fibers, while 2 represents the direction perpendicular to the fibers.

In matrix form, these equations become

$$\begin{bmatrix} \varepsilon_{11} \\ \varepsilon_{22} \\ \gamma_{12} \end{bmatrix} = \left[S_{ij}\right] \begin{bmatrix} \sigma_{11} \\ \sigma_{22} \\ \tau_{12} \end{bmatrix} = \begin{bmatrix} S_{11} & S_{12} & 0 \\ S_{12} & S_{22} & 0 \\ 0 & 0 & S_{66} \end{bmatrix} \begin{bmatrix} \sigma_{11} \\ \sigma_{22} \\ \tau_{12} \end{bmatrix}, \text{ where } \left[S_{ij}\right] = \begin{bmatrix} \dfrac{1}{E_{11}} & \dfrac{-\upsilon_{21}}{E_{22}} & 0 \\ \dfrac{-\upsilon_{12}}{E_{11}} & \dfrac{1}{E_{22}} & 0 \\ 0 & 0 & \dfrac{1}{G_{12}} \end{bmatrix} \tag{4}$$

$[S_{ij}]$ is the compliance matrix.

The reduced stiffness matrix $[Q_{ij}]$ relates the strains in local coordinates to the stresses in local coordinates as follows.

$$\begin{bmatrix} \sigma_{11} \\ \sigma_{22} \\ \tau_{12} \end{bmatrix} = \left[Q_{ij}\right] \begin{bmatrix} \varepsilon_{11} \\ \varepsilon_{22} \\ \gamma_{12} \end{bmatrix} = \begin{bmatrix} Q_{11} & Q_{12} & 0 \\ Q_{12} & Q_{22} & 0 \\ 0 & 0 & Q_{66} \end{bmatrix} \begin{bmatrix} \varepsilon_{11} \\ \varepsilon_{22} \\ \gamma_{12} \end{bmatrix}, \text{ where } \left[Q_{ij}\right] = \begin{bmatrix} \dfrac{E_{11}}{1-\upsilon_{12}\upsilon_{21}} & \dfrac{\upsilon_{21}E_{22}}{1-\upsilon_{12}\upsilon_{21}} & 0 \\ \dfrac{\upsilon_{21}E_{22}}{1-\upsilon_{12}\upsilon_{21}} & \dfrac{1}{E_{22}} & 0 \\ 0 & 0 & G_{12} \end{bmatrix} \tag{5}$$

The following matrices describe the relationships between stresses and strains in local and global coordinates:

$$\begin{bmatrix} \sigma_{11} \\ \sigma_{22} \\ \tau_{12} \end{bmatrix} = \left[T_{ij}\right] \begin{bmatrix} \sigma_{xx} \\ \sigma_{yy} \\ \tau_{xy} \end{bmatrix} = \begin{bmatrix} T_{11} & T_{12} & T_{16} \\ T_{12} & T_{22} & T_{26} \\ T_{61} & T_{62} & T_{66} \end{bmatrix} \begin{bmatrix} \sigma_{xx} \\ \sigma_{yy} \\ \tau_{xy} \end{bmatrix} \tag{6}$$

where

$$\left[T_{ij}\right] = \begin{bmatrix} \cos^2\theta & \sin^2\theta & 2\sin\theta\cos\theta \\ \sin^2\theta & \cos^2\theta & -2\sin\theta\cos\theta \\ -\sin\theta\cos\theta & \sin\theta\cos\theta & \cos^2\theta - \sin^2\theta \end{bmatrix} \tag{7}$$

Similarly

$$\begin{bmatrix} \varepsilon_{11} \\ \varepsilon_{22} \\ \gamma_{12} \end{bmatrix} = \left[\hat{T}_{ij}\right] \begin{bmatrix} \varepsilon_{xx} \\ \varepsilon_{yy} \\ \gamma_{xy} \end{bmatrix} = \begin{bmatrix} \hat{T}_{11} & \hat{T}_{12} & \hat{T}_{16} \\ \hat{T}_{12} & \hat{T}_{22} & \hat{T}_{26} \\ \hat{T}_{61} & \hat{T}_{62} & \hat{T}_{66} \end{bmatrix} \begin{bmatrix} \varepsilon_{xx} \\ \varepsilon_{yy} \\ \gamma_{xy} \end{bmatrix} \tag{8}$$

where

$$[\hat{T}_{ij}] = \begin{bmatrix} 1 & 0 & 0 \\ 0 & 1 & 0 \\ 0 & 0 & 2 \end{bmatrix} [T_{ij}] \begin{bmatrix} 1 & 0 & 0 \\ 0 & 1 & 0 \\ 0 & 0 & \frac{1}{2} \end{bmatrix} = \begin{bmatrix} \cos^2\theta & \sin^2\theta & \sin\theta\cos\theta \\ \sin^2\theta & \cos^2\theta & -\sin\theta\cos\theta \\ -2\sin\theta\cos\theta & 2\sin\theta\cos\theta & \cos^2\theta - \sin^2\theta \end{bmatrix} \tag{9}$$

Finally, the stresses and strains for an orthotropic lamina in global coordinates can be expressed as follows.

$$\begin{bmatrix} \sigma_{xx} \\ \sigma_{yy} \\ \tau_{xy} \end{bmatrix} = [\bar{Q}_{ij}] \begin{bmatrix} \varepsilon_{xx} \\ \varepsilon_{yy} \\ \gamma_{xy} \end{bmatrix} = \begin{bmatrix} \bar{Q}_{11} & \bar{Q}_{12} & \bar{Q}_{16} \\ \bar{Q}_{12} & \bar{Q}_{22} & \bar{Q}_{26} \\ \bar{Q}_{61} & \bar{Q}_{62} & \bar{Q}_{66} \end{bmatrix} \begin{bmatrix} \varepsilon_{xx} \\ \varepsilon_{yy} \\ \gamma_{xy} \end{bmatrix} \tag{10}$$

where $\left[\bar{Q}_{ij}\right] = \left[T_{ij}\right]^{-1}\left[Q_{ij}\right]\left[\hat{T}_{ij}\right]$, $\bar{Q}$ is the global stiffness matrix of the lamina, and θ is its fiber orientation.

$$\bar{Q}_{11} = Q_{11}\cos^4\theta + 2(Q_{12} + 2Q_{66})\sin^2\theta\cos^2\theta + Q_{22}\sin^4\theta \tag{11}$$

$$\bar{Q}_{22} = Q_{11}\sin^4\theta + 2(Q_{12} + 2Q_{66})\sin^2\theta\cos^2\theta + Q_{22}\cos^4\theta \tag{12}$$

$$\bar{Q}_{12} = \bar{Q}_{21} = (Q_{11} + Q_{22} - 4Q_{66})\sin^2\theta\cos^2\theta + Q_{12}(\sin^4\theta + \cos^4\theta) \tag{13}$$

$$\bar{Q}_{66} = (Q_{11} + Q_{22} - 2Q_{12} - 2Q_{66})\sin^2\theta\cos^2\theta + Q_{66}(\sin^4\theta + \cos^4\theta) \tag{14}$$

$$\bar{Q}_{16} = \bar{Q}_{61} = (Q_{11} - Q_{12} - 2Q_{66})\sin\theta\cos^3\theta + (Q_{12} - Q_{22} + 2Q_{66})\sin^3\theta\cos\theta \tag{15}$$

$$\bar{Q}_{26} = \bar{Q}_{62} = (Q_{11} - Q_{12} - 2Q_{66})\sin^3\theta\cos\theta + (Q_{12} - Q_{22} + 2Q_{66})\sin\theta\cos^3\theta \tag{16}$$

Similarly, the global strain-stress relationships can be obtained as follows.

$$\begin{bmatrix} \varepsilon_{xx} \\ \varepsilon_{yy} \\ \gamma_{xy} \end{bmatrix} = [\bar{S}_{ij}] \begin{bmatrix} \sigma_{xx} \\ \sigma_{yy} \\ \tau_{xy} \end{bmatrix} = \begin{bmatrix} \bar{S}_{11} & \bar{S}_{12} & \bar{S}_{16} \\ \bar{S}_{12} & \bar{S}_{22} & \bar{S}_{26} \\ \bar{S}_{61} & \bar{S}_{62} & \bar{S}_{66} \end{bmatrix} \begin{bmatrix} \sigma_{xx} \\ \sigma_{yy} \\ \tau_{xy} \end{bmatrix} \tag{17}$$

where $[\bar{S}_{ij}]$ is the global compliance matrix of the lamina.

$$\overline{S}_{11} = S_{11}\cos^4\theta + (2S_{12} + S_{66})\sin^2\theta\cos^2\theta + S_{22}\sin^4\theta \tag{18}$$

$$\overline{S}_{22} = S_{11}\sin^4\theta + (2S_{12} + S_{66})\sin^2\theta\cos^2\theta + S_{22}\cos^4\theta \tag{19}$$

$$\overline{S}_{12} = S_{12}\left(\sin^4\theta + \cos^4\theta\right) + (S_{11} + S_{22} - S_{66})\sin^2\theta\cos^2\theta \tag{20}$$

$$\overline{S}_{16} = \left(2S_{11} - 2S_{12} - S_{66}\right)\sin\theta\cos^3\theta - (2S_{22} - 2S_{12} - S_{66})\sin^3\theta\cos\theta \tag{21}$$

$$\overline{S}_{26} = \left(2S_{11} - 2S_{12} - S_{66}\right)\sin^3\theta\cos\theta - (2S_{22} - 2S_{12} - S_{66})\sin\theta\cos^3\theta \tag{22}$$

$$\overline{S}_{66} = 2\left(2S_{11} + 2S_{22} - 4S_{12} - S_{66}\right)\sin^2\theta\cos^2\theta + S_{66}(\sin^4\theta + \cos^4\theta) \tag{23}$$

In a laminate, the midplane strains and curvatures are related to the applied forces and moment resultants as follows.

$$\begin{bmatrix} N_{xx} \\ N_{yy} \\ N_{xy} \end{bmatrix} = \left[A_{ij}\right]\begin{bmatrix} \overset{o}{\varepsilon}_{xx} \\ \overset{o}{\varepsilon}_{yy} \\ \overset{o}{\gamma}_{xy} \end{bmatrix} + \left[B_{ij}\right]\begin{bmatrix} k_{xx} \\ k_{yy} \\ k_{xy} \end{bmatrix} \tag{24}$$

where N_{xx}, N_{yy}, and N_{xy} are the force resultants.

$$\begin{bmatrix} M_{xx} \\ M_{yy} \\ M_{xy} \end{bmatrix} = \left[B_{ij}\right]\begin{bmatrix} \overset{o}{\varepsilon}_{xx} \\ \overset{o}{\varepsilon}_{yy} \\ \overset{o}{\gamma}_{xy} \end{bmatrix} + \left[D_{ij}\right]\begin{bmatrix} k_{xx} \\ k_{yy} \\ k_{xy} \end{bmatrix} \tag{25}$$

where M_{xx}, M_{yy}, and M_{xy} are the moment resultants.

$[A_{ij}]$ is the extensional stiffness matrix for the laminate.
$[B_{ij}]$ is the coupling stiffness matrix for the laminate.
$[D_{ij}]$ is the bending stiffness matrix for the laminate.

The elements in $[A_{ij}]$, $[B_{ij}]$, and $[D_{ij}]$ matrices are calculated as follows.

$$\left[A_{ij}\right] = \sum_{k=1}^{n}\left(\overline{Q}_{ij}\right)_k\left(h_k - h_{k-1}\right) \tag{26}$$

$$[B_{ij}] = \frac{1}{2}\sum_{k=1}^{n}(\overline{Q}_{ij})_k\left(h_k^{\,2} - h_{k-1}^{\,2}\right) \tag{27}$$

$$[D_{ij}] = \frac{1}{3}\sum_{k=1}^{n}(\overline{Q}_{ij})_k\left(h_k^{\,3} - h_{k-1}^{\,3}\right) \tag{28}$$

Due to the tedious nature of the calculations and the properties needed to apply the CLPT, more simplified yet accurate methods have been developed as an optimization tool for the preliminary designs.

4.2.5 The Ten Percent Rule.

The Ten Percent Rule is an empirical, yet fairly accurate, method used to estimate the strength and stiffness of composite structures given the orientation of the different plies and the percentage of the fibers in different directions. The underlying reasoning behind the Ten Percent Rule is that composites are always stronger and stiffer in the direction of the fibers than in the directions normal to this axis. Therefore, the fibers running along the loading direction, i.e., the primary fibers, are considered to be 100% efficient in carrying the load, whereas the fibers running along other directions, i.e., secondary fibers, are considered to be only 10% efficient [18].

4.2.5.1 Ten Percent Rule for Tape Laminates.

The Ten Percent Rule can be used as a preliminary analysis tool that gives results slightly lower than the CLPT. The only material properties needed for this method can be obtained by performing a simple tensile and compressive test with all the fibers in the 0° direction. These properties are the following [18 and 19]:

- E_0, the longitudinal modulus.
- F_0, the longitudinal tensile ($F_0^{\,t}$) or compressive ($F_0^{\,c}$) strength. The greater value is chosen.
- Poisson's ratio, if not available, can be assumed to be 0.3.

The results of the Ten Percent Rule are an accurate measurement of the mechanical properties of the repair since the coupons are manufactured with the same materials and processes. For tension or compression uniaxial loading, the Ten Percent Rule assumes that the fibers running along the principal loading direction, 0°, have a load-carrying capacity of 100%, whereas those aligned with the ±45° and 90° directions have only 10% of that capacity. For in-plane shear loading, fibers running along the ±45° direction have a 100% load-carrying capacity, whereas those running in the 0° or 90° directions have only 10% of that capacity. This is illustrated in figure 63, showing the load-carrying capability of a unitape laminate as a function of its ply orientation. For biaxial loads of the same sign, the ±45° plies have an increased contribution to the strength and stiffness. This contribution is 0.55 instead of 0.1 for uniaxial loads.

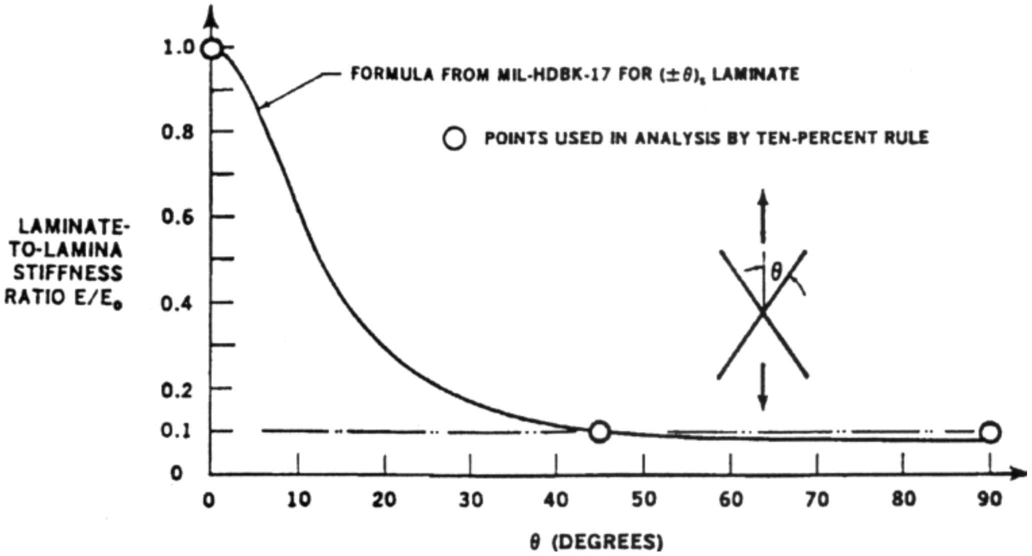

FIGURE 63. UNITAPE LAMINATE STIFFNESS AND STRENGTH RATIOS SHOWN FOR DIFFERENT PLY ORIENTATIONS [16]

For both tension and compression loading, the Ten Percent Rule for stiffness *E* and strength *F* can be calculated as follows.

$$\frac{E}{E_0} \approx \frac{F}{F_0} \approx 1.0 \times (\mathit{fraction\ of}\ 0^\circ\ \mathit{plies}) + 0.1 \times (\mathit{fraction\ of} \pm 45^\circ\ \mathit{and}\ 90^\circ\ \mathit{plies}) \tag{29}$$

where E_0 is the Young's modulus of a unidirectional monolayer.

For example, a cross-ply laminate would have a stiffness or strength ratio of (1.0×0.5+0.1×0.5) or 0.55. In other words, the strength of a cross-ply laminate is 0.55, the strength of an all 0° laminate.

A simpler equation can be used to determine the uniaxial strength and stiffness factors.

$$\frac{F}{F_0} = 0.1 + 0.9 \times (\mathit{fraction\ of}\ 0^\circ\ \mathit{plies}) \tag{30}$$

Similarly, the biaxial strength and stiffness factors can be evaluated as follows:

$$\frac{F}{F_0} = 0.55 \pm 0.45 \times (\mathit{fraction\ of}\ 0^\circ\ \mathit{plies} - \mathit{fraction\ of}\ 90^\circ\ \mathit{plies}) \tag{31}$$

The biaxial loads in this case are of the same sign. Furthermore, the larger value corresponds to the direction with the higher-fiber content in the 0° or 90° direction.

Figure 64 shows a comparison between the strength or stiffness ratios predicted by the CLPT and the Ten Percent Rule. The Ten Percent Rule consistently underpredicts the laminate strength and stiffness ratios by up to 10%.

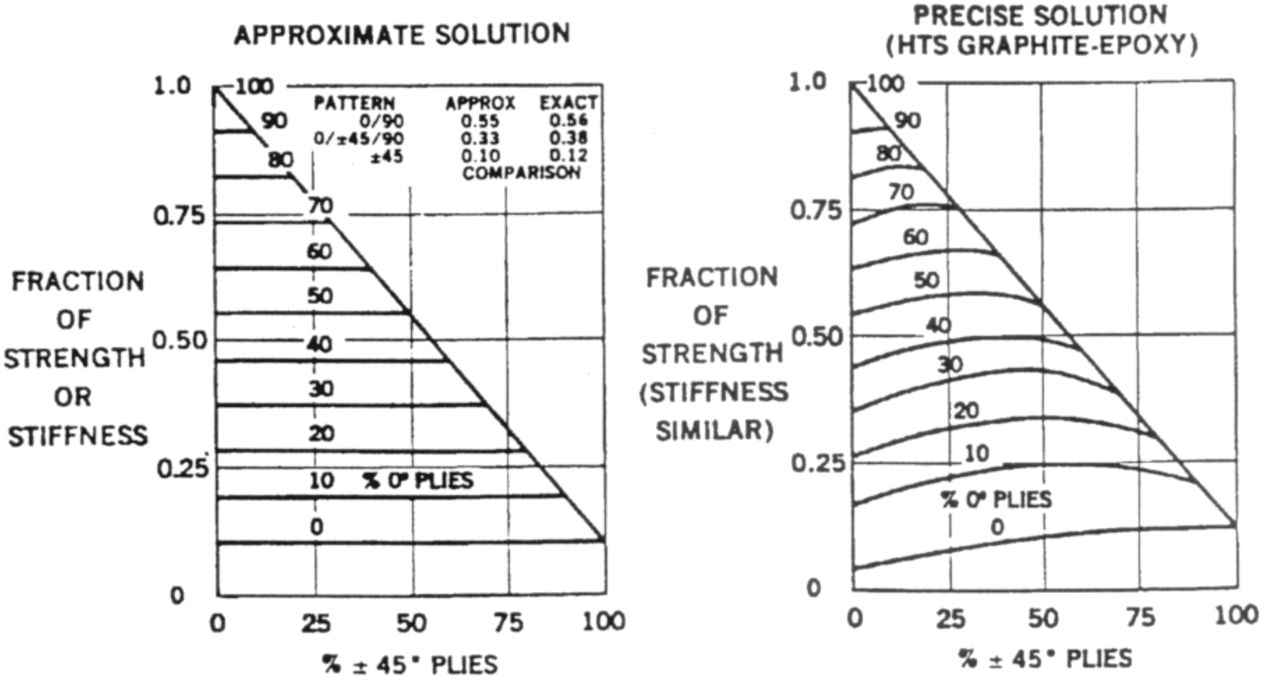

FIGURE 64. COMPARISON BETWEEN CLPT AND THE TEN PERCENT RULE [16]

Poisson's ratio is calculated as follows.

$$\upsilon_{xy} = \frac{1}{1+\dfrac{49(\%90^\circ)}{(\%\pm 45^\circ)}} \qquad (32)$$

This equation is valid for laminates with at least 12.5% of plies in each of the four directions, with no more than 37.5% in any one direction. The recommended fiber pattern is shown in figure 65. Nevertheless, this equation does not account for the matrix contribution, which may be significant for laminates with ply orientations different than the percentage specified.

For in-plane shear loading, the Ten Percent Rule can be applied as follows.

$$\frac{F_{SU}}{F_0} = \frac{1}{2}\left[\frac{(1.0+0.1)}{2}\left(fraction\,of \pm 45^\circ\ plies\right)+\left(fraction\,of\ 0^\circ\ and\,90^\circ\ plies\right)\right] \qquad (33)$$

This equation assumes that the tensile and compressive stresses are the same; thus, the shear strength can be estimated as half the uniaxial strength.

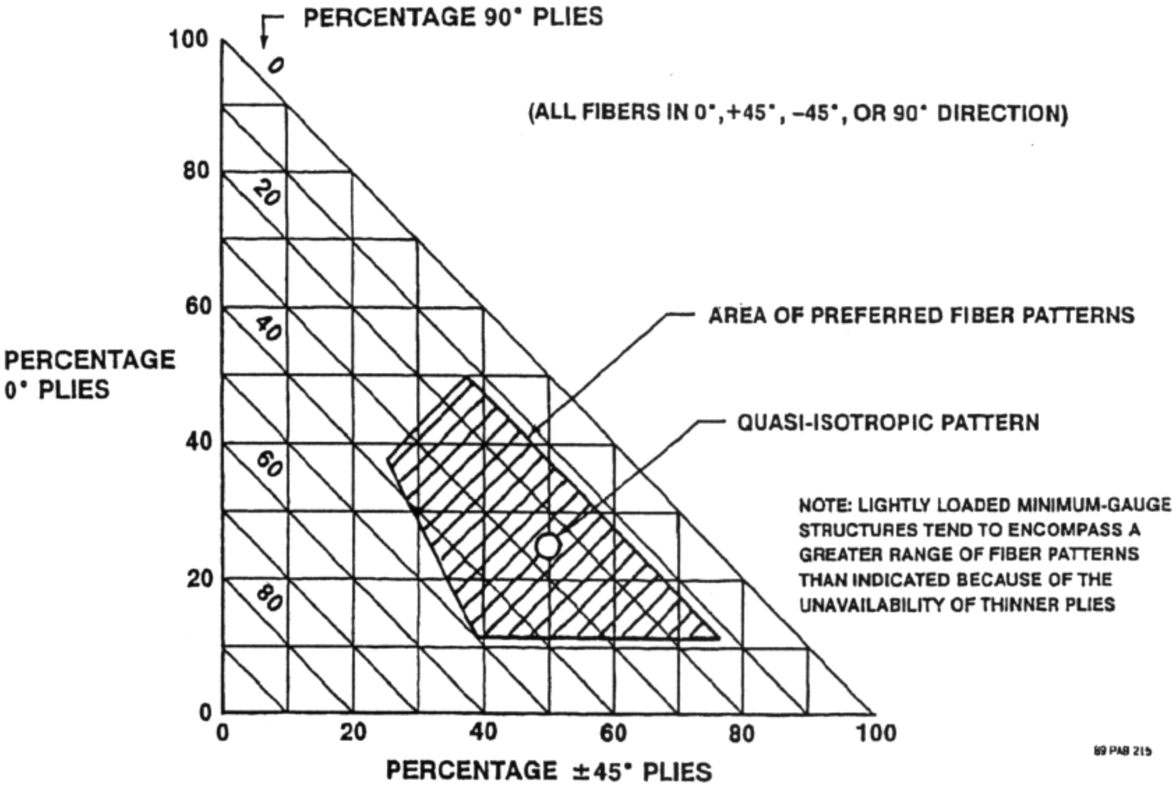

FIGURE 65. RECOMMENDED FIBER PATTERN

The shear strength factor can also be calculated using a simple formula.

$$\frac{F_{SU}}{F_0} = 0.05 + 0.225\ (\mathit{fraction\ of} \pm 45^\circ\ \mathit{plies}) \tag{34}$$

This factor is calculated with respect to the larger value of the uniaxial tension and compression of the lamina.

The shear modulus can be obtained as follows.

$$\frac{G}{E_0} = \left[G_{\pm 45} \times \left(\mathit{fraction\,of} \pm 45^\circ\ \mathit{layers}\right) + G_{0/90} \times \left(\mathit{fraction\,of}\ 0^\circ\ \mathit{layers}\right)\right] \tag{35}$$

or otherwise

$$\frac{G}{E_0} = 0.028 + 0.234 \times \left(\mathit{fraction\ of} \pm 45^\circ\right) \tag{36}$$

For doubly symmetric laminates, the uniaxial strength is related to the biaxial strength as follows

$$Uniaxial\ Strength = (1-\upsilon)\times Biaxial\ Strength \tag{37}$$

4.2.5.2 Ten Percent Rule for Fabric Laminates.

This method assumes that laminates are made out of balanced fabric, containing the same number of fibers in both the warp and fill directions. The formulas used for this analysis are similar to the ones used for tape laminates but are rearranged to better define the characteristics of the fabric.

The Ten Percent Rule applied to fabric laminates defines the strength and stiffness ratios as follows.

$$\frac{E}{E_{0/90}} \approx \frac{F}{F_{c,t}} \approx \frac{1}{0.55}\left[0.55\times\left(fraction\,of\ 0^\circ/90^\circ\ fibers\right)+0.1\times\left(fraction\,of\ \pm 45^\circ\ fibers\right)\right] \tag{38}$$

For a tape or fabric laminate with all the fibers in the ±45° directions, given υ_0 (Poisson's ratio for unidirectional monolayer tape), the Poisson's ratio can be calculated as follows.

$$\upsilon_{\pm 45^o} = \frac{250+100\upsilon_0}{350} \tag{39}$$

The overall Poisson's ratio can be obtained using the following equation.

$$\upsilon_{xy} = \left[\frac{2.5(\%\pm 45^\circ)+350(\upsilon_{\pm 45^\circ})-250}{550-2.0(\%\pm 45^\circ)}\right] \tag{40}$$

Similarly, the corresponding formula for shear strength can be obtained as follows.

$$F_{su} = \frac{F_c F_t}{F_c+F_t}\times\frac{1}{0.55}\left[0.55\left(fraction\,of\ \pm 45^\circ\ layers\right)+0.1\times\left(fraction\,of\ 0^\circ/90^\circ\ layers\right)\right] \tag{41}$$

The maximum and minimum shear modulus values are obtained from a cross-ply and an angle-ply laminate. These values are used to define the shear modulus equation as follows.

$$\frac{G}{E_0} = \left[G_{\pm 45}\times\left(fraction\,of\ \pm 45^\circ\ layers\right)+G_{0/90}\times\left(fraction\,of\ 0^\circ/90^\circ\ layers\right)\right] \tag{42}$$

4.2.6 CACRC-Improved Solution.

4.2.6.1 CACRC-Improved Solution for Tape Laminates.

The main difference between the Ten Percent Rule and the CACRC-improved solution is that the latter takes into consideration the resin matrix properties by using a monolayer Poisson's ratio value, υ_0 in the strength, stiffness, and Poisson's equations [16]. As a result, accuracy is improved and values obtained are comparable to, sometimes even higher than, those obtained using the CLPT.

Using this method, stiffness and strength ratios can be approximated as follows.

$$\frac{E}{E_0} \approx \frac{F}{F_0} \approx \frac{1}{100}\left\{\left[1-\frac{(\upsilon - \upsilon_0)\upsilon_0}{10}\right](\%0^\circ\ plies)+\left[\frac{1-\upsilon}{4}+\frac{1-\upsilon\upsilon_0}{10}\right](\%45^\circ\ plies)+\left[\frac{1-\upsilon\upsilon_0}{10}\right](\%90^\circ\ plies)\right\} \quad (43)$$

The resulting strength and stiffness ratios are shown in figure 66.

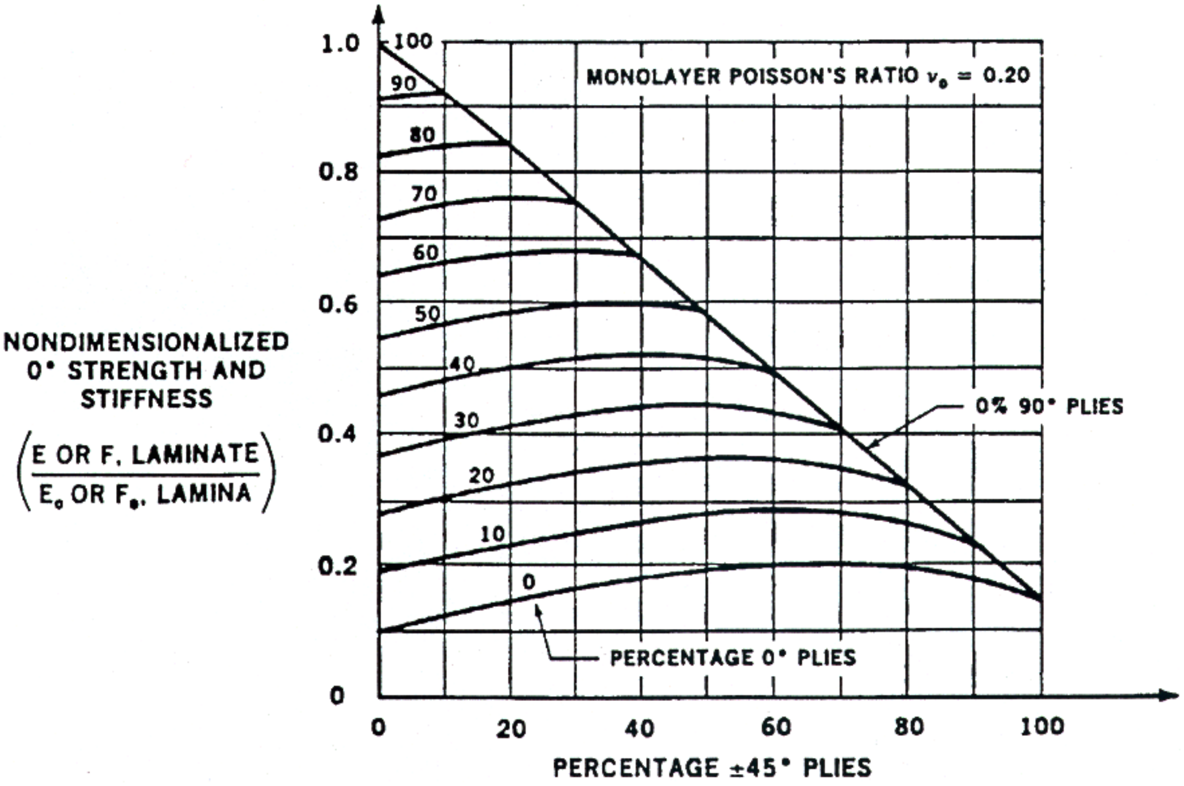

FIGURE 66. STRENGTH AND STIFFNESS RATIOS OF (0°, ±45°, 90°) LAMINATES CALCULATED USING THE CACRC-IMPROVED SOLUTION

Similarly, the Poisson's ratio can be calculated as follows.

$$\upsilon_{xy} = \left[\frac{2.5(\% \pm 45^{\circ}) + 100\upsilon_0}{2.5(\% \pm 45^{\circ}) + 9(\% 90^{\circ}) + 100} \right] \tag{44}$$

4.2.6.2 CACRC-Improved Solution for Balanced Fabric Laminates.

Unlike the Ten Percent Rule, this method takes into consideration the properties of the fibers and the resin matrix [16].

Strength and stiffness ratios are expressed as follows.

$$\frac{E}{E_{0/90}} = \frac{F}{F_{c,t}} \approx \frac{1}{0.55} \left\{ 0.35 \times [1 - \upsilon_{\pm 45}\upsilon] + \left[0.2 + 0.25\upsilon + \frac{(3.5\upsilon_{\pm 45} - 2.5)^2}{20} \right] (\textit{fraction of } 0^{\circ}/90^{\circ} \textit{ fibers}) \right\} \tag{45}$$

As illustrated in figures 67 through 70, both the Ten Percent Rule and the CACRC-improved solution show a good correlation with the CLPT, even if the results obtained using the Ten Percent Rule are generally lower.

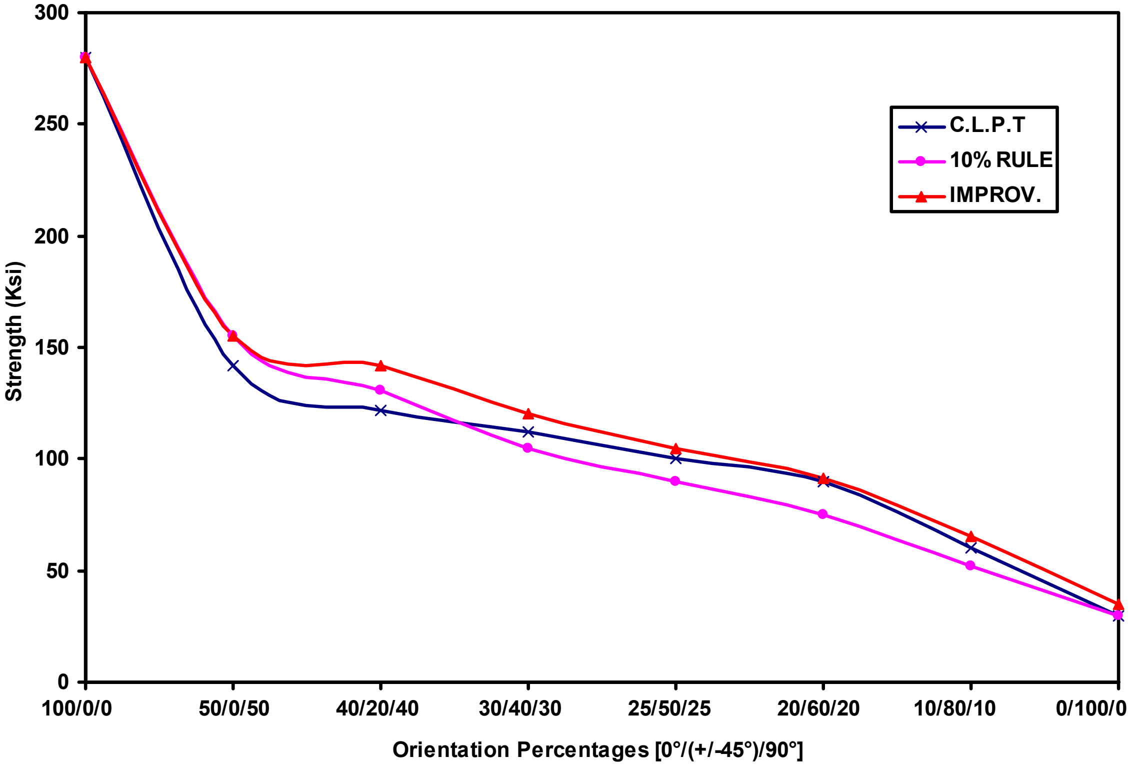

FIGURE 67. STRENGTH VALUES OBTAINED USING THE THREE ANALYSIS TECHNIQUES FOR AS4/3501-6 CARBON TAPE [16]

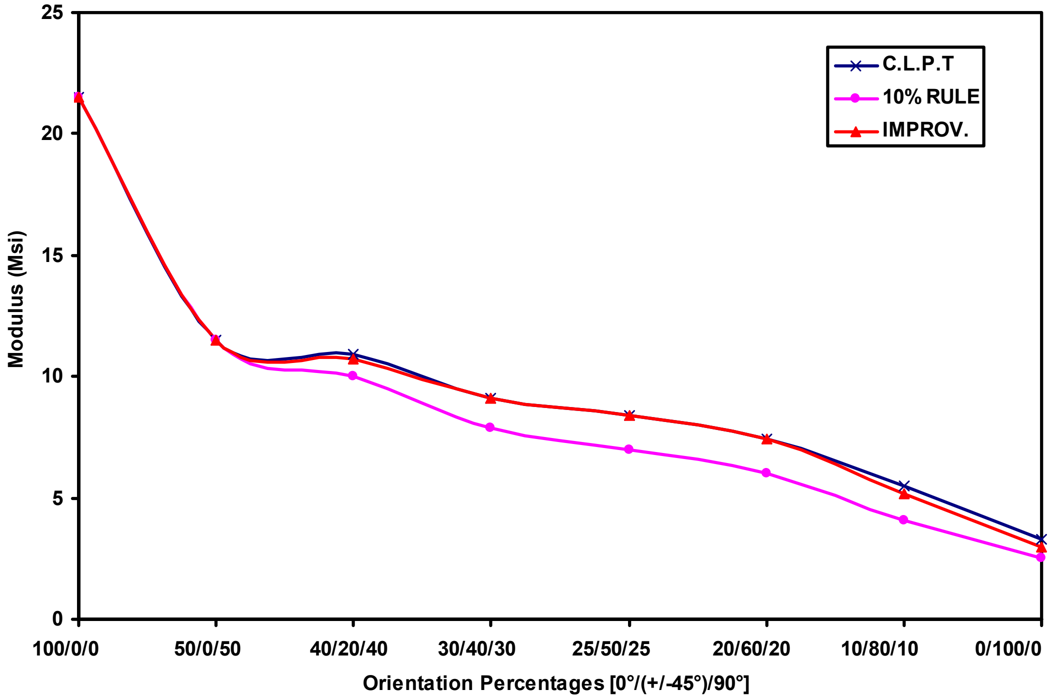

FIGURE 68. MODULUS VALUES OBTAINED USING THE THREE ANALYSIS TECHNIQUES FOR AS4/3501-6 CARBON TAPE [16]

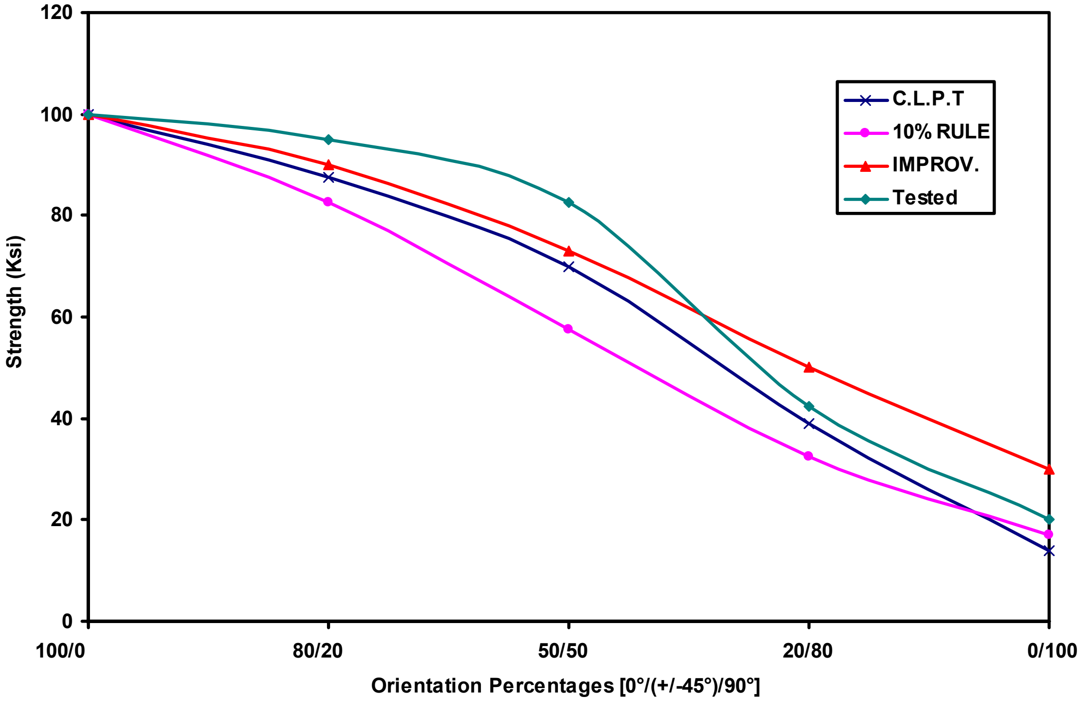

FIGURE 69. STRENGTH VALUES OBTAINED USING THE THREE ANALYSIS TECHNIQUES FOR CYCOM 919 GF3070PW CARBON FABRIC [16]

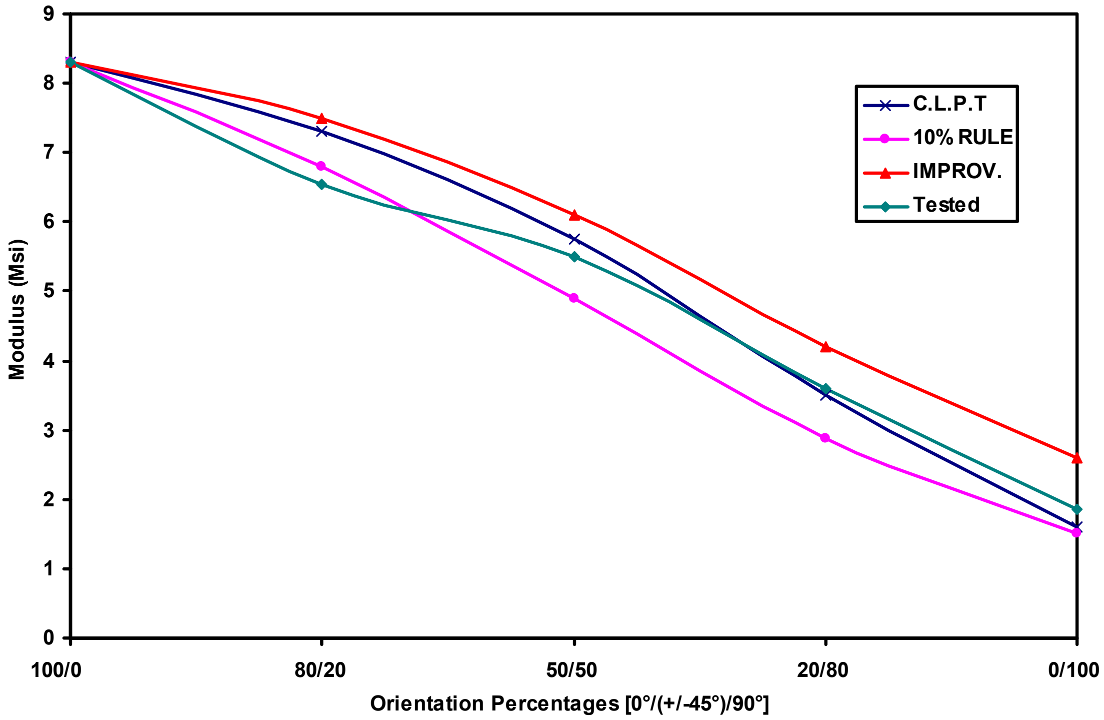

FIGURE 70. MODULUS VALUES OBTAINED USING THE THREE ANALYSIS TECHNIQUES FOR CYCOM 919 GF3070PW CARBON FABRIC [16]

Even if the results obtained using the Ten Percent Rule and the CACRC-improved solution have a good correlation with the CLPT and the tested values, these simplified methods have the following limitations:

- These methods do not take into consideration coupling effects; therefore, they are only valid for balanced and symmetric laminates.
- Multiple load conditions are not taken into account; the methods only evaluate load applied in one direction at a time.
- Thermal and moisture effects are not considered.
- Ply directions are limited to 0°, 90°, and ±45°.

4.2.7 Scarf Joint Models.

As previously mentioned, unlike single and double lap joints, scarf joints are the most efficient in restoring the load capability of a structure. In a scarf joint, the load eccentricities that make the single and double lap joints vulnerable are minimal. Therefore, as long as the scarf joint has sufficient overlap length and repair laminate stiffness and thickness comparable to the parent laminate, the desirable strength can be achieved. However, stiffness imbalance and thermal mismatch between the adherends limit the strength of this type of joint.

Adhesive-bonded scarf joints between composite materials are difficult to analyze due to the anisotropy and heterogeneity of the adherends. Analyses can be divided into two main subgroups: linear and nonlinear. Linear analyses assume the adhesive behavior to be linear elastic, while nonlinear analyses assume the adhesive behavior to be elastic-plastic.

The model developed by Reddy and Sinha [20] is a linear analysis between two orthotropic adherends. The model considers both plain strain and plain stress conditions. Results show that stresses in the adhesive are driven by its properties and that for different adherends, the highest stresses occur on the stiffer side of the joint. This model does not take into consideration the variation of stresses through the thickness. This model was further developed to include the effects of residual stresses due to thermal effects that occur during the curing process. As a result, the critical joint depends on the loading direction [21].

The adhesive nonlinear behavior is considered in the analysis of Grant [22]. Nevertheless, the most extensive work has been done by Hart-Smith [14]. His model shows that the adhesive shear stress is uniform if the adherends are identical. However, for dissimilar adherends, an increasing stiffness mismatch causes a nonuniform shear stress distribution in the adhesive.

4.2.7.1 Scarf Joint Simple Elastic Stress Analysis.

This method is a simple mechanics of materials analysis of adhesive-bonded scarf joints. It assumes that the stress distribution is uniform along the scarf and that the stiffnesses and expansion coefficients of the adherends are similar [23]. The optimum scarf angle to achieve an effective joint is 3° or less. In reality, scarf angles used for repair of composite structures range between 0.8° and 1.8°, corresponding to ply overlaps of 0.25 to 0.50 inch, respectively. Figure 71 shows the nomenclature of the scarf joint used for this analysis.

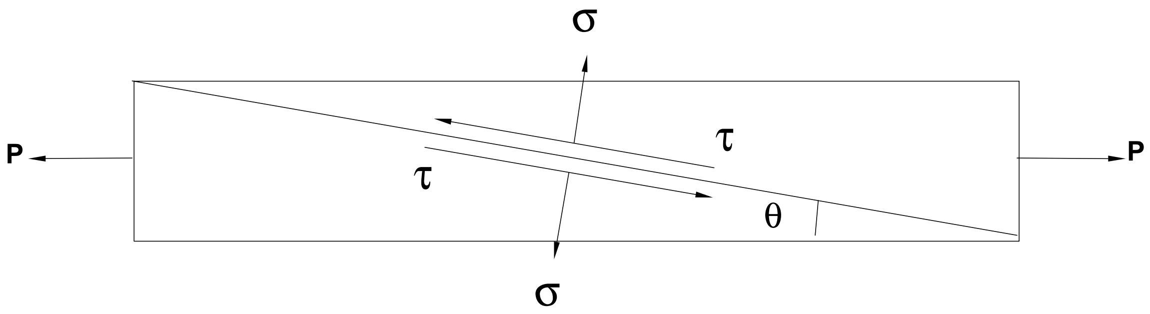

FIGURE 71. SCARF JOINT LOAD AND STRESS RESULTANTS

The adhesive is assumed to undergo only elastic deformation. Stresses can be evaluated as follows.

$$\tau = \frac{P \sin 2\theta}{2t} \tag{46}$$

$$\sigma = \frac{P\sin^2\theta}{t} \tag{47}$$

where τ is the shear stress acting along the scarf, and σ is the out-of-plane stress acting perpendicular to the scarf.

As the scarf angle approaches 0 and assuming $\tau = \tau_P$, the allowable load can be calculated as follows.

$$P = Ee_u t = \frac{2\tau_p t}{\sin 2\theta} \tag{48}$$

Solving for the required scarf angle yields

$$\theta = \frac{\tau_P}{E\varepsilon_u} \text{ (in radians)} \tag{49}$$

The required angle should not exceed 3° for optimum joint shear capacity.

<u>4.2.7.2 Scarf Joint Precise Elastic Stress Analysis</u>.

This model, developed by Hart-Smith, accounts for adherends with different stiffnesses and different temperature and moisture expansion coefficients. It also assumes that the scarf angle is very small, which is typical of practical aerospace structures [14]. The details of the geometry and the notation used for the analysis are shown in figure 72.

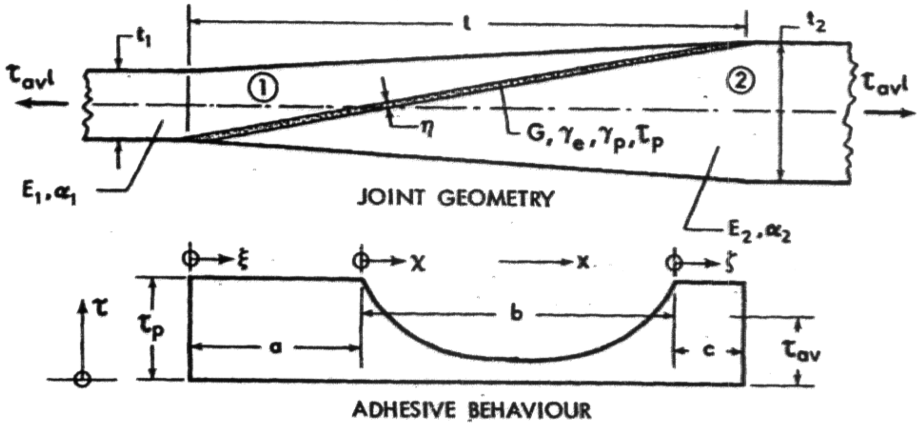

FIGURE 72. ADHESIVE-BONDED SCARF JOINT NOMENCLATURE [14]

Since this model only considers the elastic behavior of the adhesive, there are no regions that exhibit adhesive plasticity; therefore, $a = c = 0$ and $b = L$. In other words, the effects of peel stresses are not taken into account, which is a conservative assumption for very small scarf angles, i.e., very large repairs.

The equations of horizontal equilibrium of a differential element in the joint are as follows.

$$\frac{dT_1}{dx} + \tau = 0 \quad \text{and} \quad \frac{dT_2}{dx} - \tau = 0 \tag{50}$$

where T_1 and T_2 are the stress resultants in the adherends.

The stress-strain relationships for the adherends are defined as follows.

$$\frac{d\delta_1}{dx} = \frac{T_1}{(Et)_1} + \alpha_1 \Delta T \quad \frac{d\delta_2}{dx} = \frac{T_2}{(Et)_2} + \alpha_2 \Delta T \tag{51}$$

where δ_1 and δ_2 are the longitudinal displacements of the adherends.

The adhesive shear strain γ is assumed to be uniform across the thickness of the bondline yielding

$$\gamma = \frac{(\delta_2 - \delta_1)}{\eta} \tag{52}$$

where η is the adhesive thickness and δ_n is the longitudinal displacement of adherend n.

The elastic adhesive shear stress follows as

$$\tau = G\gamma = G\frac{(\delta_2 - \delta_1)}{\eta} \tag{53}$$

with G being the adhesive shear modulus.

A number of nondimensionalized parameters are defined in the following equations to minimize the number of independent variables.

The nondimensionalized overlap length, a direct measure of the joint capability, is defined as follows:

$$(\lambda l)^2 = \frac{Gl^2}{\eta}\left[\frac{1}{E_1 t_1} + \frac{1}{E_2 t_2}\right] = \frac{\tau_p l^2}{\eta \gamma_e}\left[\frac{1}{E_1 t_1} + \frac{1}{E_2 t_2}\right] \tag{54}$$

where E_1 and E_2 are the longitudinal Young's moduli for adherend 1 and 2, t_1 and t_2 are the respective thicknesses of the adherends, τ_p is the adhesive maximum shear stress, l is the overlap length, and γ_e is the adhesive elastic shear strain.

The nondimensionalized thermal mismatch is as follows.

$$CTHERM(1) = \frac{\lambda(\alpha_2 - \alpha_1)\Delta T}{\tau_p(\frac{1}{E_1 t_1} + \frac{1}{E_2 t_2})} \quad CTHERM(2) = -CTHERM(1) \tag{55}$$

where α_1 and α_2 are the coefficients of thermal expansion of the adherends.

The adherend stiffness ratio is as follows.

$$ETR(1) = \frac{E_1 t_1}{E_2 t_2} \tag{56}$$

$$ETR(2) = \frac{E_2 t_2}{E_1 t_1} \tag{57}$$

Using these nondimensionalized terms, a series solution to the scarf joint governing equations is given as follows:

$$\frac{\tau}{\tau_p} = \sum_1^\infty A_n \phi^{n-1} \tag{58}$$

where ϕ is the nondimensionalized axial coordinate $\phi = \frac{x}{l}$

A_n represents the power series coefficients that define the adhesive shear stress distribution in the bondline.

After a series of calculations for long overlaps, generally, the following applies.

$$\frac{\tau_{av}}{\tau} \rightarrow ETR\ (1) \le 1 \tag{59}$$

This equation shows that the ratio of the average bond shear stress to the peak bond shear stress is equal to the adherends stiffness ratio. It also shows the importance of maintaining the adherends stiffness ratio close to 1. In other words, whenever stiffness balance is maintained between the adherends, the scarf joint is uniformly stressed and, therefore, most efficient.

Integrating the scarf joint-governing equations, yields the following.

$$\frac{\tau_{av}}{\tau_p} = \sum_1^\infty \frac{A_n}{n} \tag{60}$$

Two arbitrary constants are used to satisfy the boundary conditions, as follows.

$$\frac{\tau_{av}}{\tau_p} = A_1 \times \sum(3) + A_2 \times \sum(4) \qquad (61)$$

If the most critical, or less capable, adherend is known, then the value A_n corresponding to the adherend is set to 1. If it is not known, one of the adherends is arbitrarily assigned the value $A_1 = 1$. The calculations are performed first with this value and again with $A_2 = 1$. After completing the calculations, the most critical adherend is identified, and the repair analysis is performed based on the lower value.

In this case, $A_1 = 1$, and therefore, the following applies.

$$\frac{\tau_{av}}{\tau_p} = \sum(3) + A_2 \times \sum(4) \qquad (62)$$

$\sum(3)$ and $\sum(4)$ are calculated from the following two equations after setting.

$$A_1 = 1 \text{ and } A_2 = 0 \; for \sum(3), \; with \sum(3) = A_1 + \frac{A_2}{2} + \frac{A_3}{3} + \text{....} + \frac{A_n}{n} \qquad (63)$$

and

$$A_1 = 0 \text{ and } A_2 = 1 \; for \sum(4), \; with \sum(4) = A_1 + \frac{A_2}{2} + \frac{A_3}{3} + \text{....} + \frac{A_n}{n} \qquad (64)$$

$$A_2 = (\lambda l)CTHERM(1) - (\lambda l)^2 \left[\frac{1}{1+ETR(1)}\right] \frac{\tau_{av}}{\tau_p} + (\lambda l)^2 \left[\frac{ETR(1)}{1+ETR(1)}\right] A_1 \qquad (65)$$

$$2A_3 - A_2 = -(\lambda l)CTHERM(1) - (\lambda l)^2 \left[\frac{1}{1+ETR(1)}\right] \left\{ [1 - ETR(1)]A_1 + ETR(1)\frac{A_2}{2} \right\} \qquad (66)$$

$$A_n = \left\{ (n-2)\frac{A_{n-1}}{n-1} + \frac{(\lambda l)^2}{n-1} \Bigg[\left(\frac{ETR(1)}{1+ETR(1)}\right) \frac{A_{n-1}}{n-1} + \left(\frac{1-ETR(1)}{1+ETR(1)}\right) \frac{A_{n-2}}{n-2} \Bigg] \Bigg] \right\} \qquad (67)$$

The coefficient A_3 is evaluated for both sets of initial conditions corresponding to $\sum(3)$ and $\sum(4)$. Then, through a recursive process, higher-order terms are evaluated. The series will usually converge after five terms; however, 10 to 20 iterations are recommended. The values of the summations are then substituted in the following equation to solve for the unknown K, which is defined as follows.

$$K = \frac{(\lambda l)(CTHERM(1))[1+ETR(1)]+(\lambda l)^2[ETR(1)-\sum(3)]}{[1+ETR(1)]+(\lambda 1)^2\sum(4)} \tag{68}$$

The potential bond shear strength is determined as follows.

$$\frac{\tau_{av}}{\tau_p} = ETR(1)+\frac{[1+ETR(1)]CTHERM(1)}{\lambda l}-\frac{[1+ETR(1)]}{(\lambda l)^2}K \tag{69}$$

4.2.7.3 Scarf Joint Elastic-Plastic Stress Analysis.

This model, unlike the previous one, accounts for the nonlinear behavior of the adhesive, which is very important for characterizing the shear stress distribution and for predicting failure [14]. The nomenclature used in the following equations was identified in figure 72.

Horizontal equilibrium for a differential element dx within the joint requires the following.

$$\frac{dT_1}{dx}+\tau=0 \quad \text{and} \quad \frac{dT_2}{dx}-\tau=0 \tag{70}$$

where $dx = ld\xi = ld\chi = ld\zeta$

The stress-strain relationships for the adherends with thermal mismatch as well as the adhesive shear strain expression remain the same, as defined in the previous model, with the only difference being $dx = ld\xi = ld\chi = ld\zeta$ when applicable.

$$\tau = \tau_p \text{ for } 0 \le \xi \le a \text{ and } 0 \le \zeta \le c \tag{71}$$

The adherend stiffness coefficients are defined as follows.

$$(Et)_1 = E_1 t_1(1-\xi) = E_1 t_1(1-\frac{a}{l}-\chi) = E_1 t_1(1-\frac{a}{l}-\frac{b}{l}\zeta) \tag{72}$$

and

$$(Et)_2 = E_2 t_2 \xi = E_2 t_2(\frac{a}{l}+\chi) = E_2 t_2(\frac{a}{l}+\frac{b}{l}+\zeta) \tag{73}$$

The solution in the elastic zone remains the same with $A_1 = 1$, that is, adherend 1 is highly loaded or more critical, as follows.

$$\frac{\tau}{\tau_p} = \sum_1^\infty A_n \chi^{(n-1)} \tag{74}$$

For the left plastic region, the adherend forces per unit width are

$$T_1 = \tau_{av} l - \tau_p l \xi \text{ and } T_2 = \tau_p l \xi \tag{75}$$

The shear strain, taking into account the plastic region, is as follows.

$$\gamma = \frac{1}{\eta}(\alpha_2 - \alpha_1)\Delta T l \xi + \tau_p l^2 \left[\frac{1}{E_2 t_2} - \frac{1}{E_1 t_1}\right]\xi - \frac{(\tau_p - \tau_{av}) l^2}{E_1 t_1} \ln(1 - \xi) + \gamma_e + \gamma_p \tag{76}$$

Furthermore, since $\gamma = \gamma_e$ for $\xi = \frac{a}{l}$, then the following applies.

$$\gamma_p = -\left(\frac{1}{\eta}(\alpha_2 - \alpha_1)\Delta T l \left(\frac{a}{l}\right) + \tau_p l^2 \left[\frac{1}{E_2 t_2} - \frac{1}{E_1 t_1}\right]\left(\frac{a}{l}\right) - \frac{(\tau_p - \tau_{av}) l^2}{E_1 t_1} \ln\left(1 - \frac{a}{l}\right)\right) \tag{77}$$

Nondimensionalizing the equation yields the following.

$$\frac{\gamma_p}{\gamma_e} = -(\lambda l) CTHERM(1)\left(\frac{a}{l}\right) + (\lambda l)^2 \left(\frac{a}{l}\right)\frac{1 - ETR(1)}{1 + ETR(1)} + (\lambda l)^2 \frac{1 - \frac{\tau_{av}}{\tau_p}}{1 + ETR(1)} \ln\left(1 - \frac{a}{l}\right) \tag{78}$$

The continuity at the transition between elastic and plastic regions needs to be maintained when solving for the joint potential strength. Continuity implies that $\frac{d\gamma}{dx}$ remains constant. In the plastic region of the transition, this boundary condition implies the following.

$$\left.\frac{d(\gamma / \gamma_e)}{d\xi}\right|_{\xi = a/l} = (\lambda l) CTHERM(1) - (\lambda l)^2 \frac{1 - ETR(1)}{1 + ETR(1)} + \frac{(\lambda l)^2 [1 - (\tau_{av} / \tau_p)]}{[1 + ETR(1)]} \tag{79}$$

In the elastic region of the transition, this boundary condition requires the following.

$$\left.\frac{d(\gamma / \gamma_e)}{d\chi}\right|_{\chi = 0} = A_2 \tag{80}$$

The recurrence formula, defined in the previous section, can be used to determine the elastic shear stress distribution.

To check the existence of a second plastic shear stress zone at the far end of the joint, the elastic shear stress is evaluated at $\chi = 1 - a/l$.

The adherends force per unit width at the right side of the joint can be calculated as follows.

$$T_1 = \tau_p l\left(\frac{c}{l} - \zeta\right) \text{ AND } T_2 = \tau_{av} l - \tau_p l\left(\frac{c}{l} - \zeta\right) \qquad (81)$$

Continuity at the right-hand side of the joint, where the adhesive behavior changes from elastic to plastic, needs to be maintained. This boundary condition requires that $\frac{d\gamma}{dx}$ remains the same from both sides of the transition.

After several calculations, it follows that

$$\frac{\gamma_{max}}{\gamma_e} = (\lambda l)CTHERM(1)\left(\frac{c}{l}\right) - (\lambda l)^2\left[\frac{1-ETR(1)}{1+ETR(1)}\right]\left(\frac{c}{l}\right) + (\lambda l)^2\frac{[1-(\tau_{av}/\tau_p)]ETR(1)}{1+ETR(1)} ln\left(1 - \frac{c}{l}\right) \qquad (82)$$

where $\gamma_{\max}$ is the maximum adhesive shear strain on the right-hand side of the joint, i.e., the less-critical side by definition.

Due to convergence difficulties found when evaluating the joint potential strength, another equation is used to evaluate the ratio $\frac{\tau_{av}}{\tau_p}$.

$$\frac{\tau_{av}}{\tau_p} = 1 - \frac{\left\{\frac{1+ETR(1)}{(\lambda l)^2}\left(\frac{\gamma_p}{\gamma_e}\right) + \left[\frac{[1+ETR(1)]CTHERM(1)}{(\lambda l)} - [1-ETR(1)]\right]\left(\frac{a}{l}\right)\right\}}{\ln[1 - a/l]} \qquad (83)$$

For the minimum value of $\frac{\tau_{av}}{\tau_p}$, the equation becomes.

$$\frac{\tau_{av}}{\tau_p} = ETR(1) + \frac{[1+ETR(1)]CTHERM(1)}{(\lambda l)} + \frac{a}{l}\left\{[1-ETR(1)] - \frac{[1+ETR(1)]CTHERM(1)}{(\lambda l)}\right\} \qquad (84)$$

As previously mentioned, in most cases, it is possible to transfer the adherends strength through the joint, provided the scarf angle is small enough. In cases where the angle is too small, adherend failure may occur [14]. To prevent this situation from happening, the scarf angle should always be kept as follows.

$$\theta \ \langle \ \frac{\tau_p}{F_u}, \qquad (85)$$

where F_u is the ultimate tensile, compressive, or shear stress in the most critical end of the joint.

4.2.7.4 Scarf Joint Elastic-Plastic Stress Analysis.

This scarf joint analysis assumes that the stress distribution in the adhesive varies through the thickness. It investigates the effects of doublers on the strength of the joint and assumes that stresses in the adhesive have two main components: one due to the joint extension or compression, as a result of the applied loads, and one due to the load transfer from the adherends, as a result of a shear load [24]. The adhesive is assumed to behave in a linear elastic manner, and its behavior in shear and tension are independent. The free-body diagram used for the purpose of this analysis is shown in figure 73.

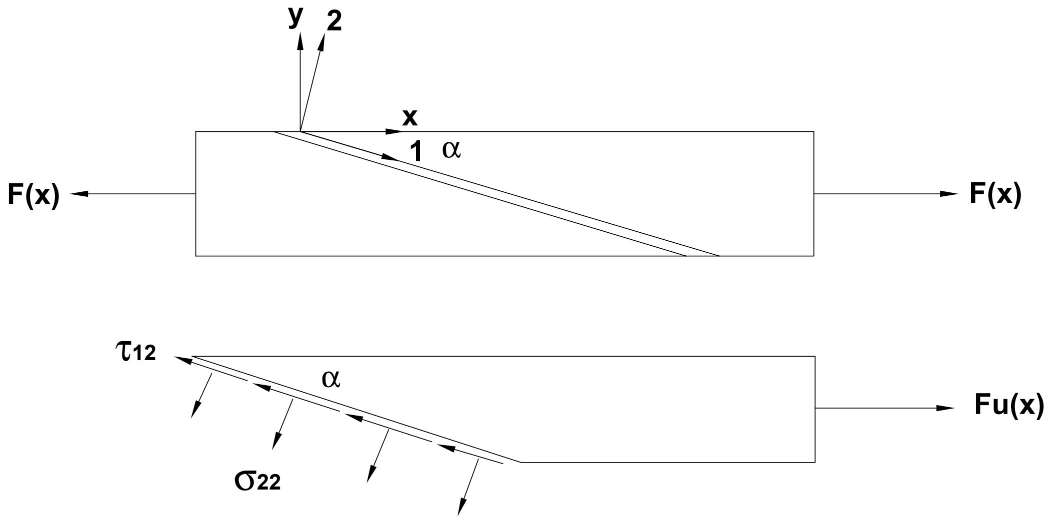

FIGURE 73. SCARF JOINT FREE-BODY DIAGRAM

$$\tau_{12} = \frac{G_A}{t_A}(\Delta u_x \cos\alpha - \Delta u_y \sin\alpha) \tag{86}$$

$$\sigma_{22} = \frac{E_A}{t_A}(\Delta u_x \sin\alpha + \Delta u_y \cos\alpha) \tag{87}$$

The condition of equilibrium in the upper adherend can be written as follows.

$$F_u(x) = w\int_0^x \{\tau_{12}(t)\cos\alpha + \sigma_{22}(t)\sin\alpha\}\frac{dt}{\cos\alpha} \tag{88}$$

$$\int_0^x \{\tau_{12}(t)\sin\alpha - \sigma_{22}(t)\sin\alpha\}\frac{dt}{\cos\alpha} = 0 \tag{89}$$

To calculate the strains in both adherends, Hooke’s law is applied. Furthermore, considering that both adherends will contract the same amount away from the specimen edges, strains in both adherends can be calculated as follows.

$$\varepsilon_{xxu} = \frac{(1-\upsilon_{xzu}\upsilon_{zxu})}{E_{xu}}\frac{F_u}{t_u w} + \frac{\upsilon_{xzlam}\upsilon_{zxu}}{E_{xlam}}\frac{F_{ext}}{t_{lam} w} \tag{90}$$

$$\varepsilon_{xxl} = \frac{(1-\upsilon_{xzl}\upsilon_{zxl})}{E_{xl}}\frac{F_l}{t_l w} + \frac{\upsilon_{xzlam}\upsilon_{zxl}}{E_{xlam}}\frac{F_{ext}}{t_{lam} w} \tag{91}$$

After some manipulation, the scarf joint-governing differential equation can be calculated as follows.

$$\frac{d^2F_u}{dx^2} - K\left[\frac{1-\upsilon_{xzu}\upsilon_{zxu}}{E_{xu}x\,tan\,\alpha} + \frac{1-\upsilon_{xzl}\upsilon_{zxl}}{E_{xl}(d-x)\,tan\,\alpha}\right]F_u = K\left[\frac{\upsilon_{xzlam}}{E_{xlam}t_{lam}}(\upsilon_{zxu}-\upsilon_{zxl}) - \frac{1-\upsilon_{xzl}\upsilon_{zxl}}{E_{xl}(d-x)\,tan\,\alpha}\right]F_{ext} \tag{92}$$

By nondimensionalizing the equation, using the following

$$\overline{F} = \frac{F_u}{F_{ext}} \text{ and } \overline{x} = \frac{x}{d}$$

the equation then becomes

$$\frac{d^2\overline{F_u}}{d\overline{x}^2} - \frac{Kd}{tan\,\alpha}\left[\frac{1-\upsilon_{xzu}\upsilon_{zxu}}{E_{xu}\overline{x}} + \frac{1-\upsilon_{xzl}\upsilon_{zxl}}{E_{xl}(1-\overline{x})}\right]\overline{F} = \frac{Kd}{tan\,\alpha}\left[\frac{d\upsilon_{xzlam}(\upsilon_{zxu}-\upsilon_{zxl})\,tan\,\alpha}{E_{xlam}t_{lam}} - \frac{1-\upsilon_{xzl}\upsilon_{zxl}}{E_{xl}(1-\overline{x})}\right] \tag{93}$$

The upper adherend carries no load at the tip because no load has been transferred to it; however, at the other end of the joint, the entire load is carried by the upper adherend. The boundary conditions are as follows.

$$F_u = 0 \text{ at } x = 0 \text{ and } F_u = F \text{ at } x = d \tag{94}$$

which is equivalent to the following

$$\overline{F} = 0 \text{ at } \overline{x} = 0 \text{ and } \overline{F} = 1 \text{ at } \overline{x} = 1 \tag{95}$$

Solving of the governing differential equation

$$\varepsilon^2 \bar{F}'' - Q(\bar{x})\bar{F} + R(\bar{x}) = 0 \tag{96}$$

where

$$\varepsilon = \sqrt{\frac{\tan\alpha}{Kd}} \tag{97}$$

yields

$$Q(\bar{x}) = \frac{1-\upsilon_{xzu}\upsilon_{zxu}}{E_{xu}\bar{x}} + \frac{1-\upsilon_{xzl}\upsilon_{zxl}}{E_{xl}(1-\bar{x})} \tag{98}$$

and

$$R(\bar{x}) = \frac{1-\upsilon_{xzl}\upsilon_{zxl}}{E_{xl}(1-\bar{x})} - \frac{d\upsilon_{xzlam}(\upsilon_{zxu}-\upsilon_{zxl})\tan\alpha}{E_{xlam}t_{lam}} \tag{99}$$

When ε is small (α<6°), the Wentzel, Kramers, and Brillouin method can be used to approximate the solution as follows.

$$F(\bar{x}) \sim \frac{R(\bar{x})}{Q(\bar{x})} + B_1 \exp\left[\frac{S_0}{\varepsilon} + S_1\right] + B_2 \exp\left[-\frac{S_0}{\varepsilon} + S_1\right] \tag{100}$$

This solution does not hold at the scarf tip for (α > 6°). The following Frobenius method needs to be used.

$$F(\bar{x}) = \sum_{n=0}^{\infty} a_n \bar{x}^{n+1} + \sum_{n=0}^{\infty} c_n \bar{x}^{n} - \ln\bar{x}\sum_{n=0}^{\infty} a_n \bar{x}^{n+1} - \sum_{n=0}^{\infty} b_n \bar{x}^{n+1} + \sum_{n=0}^{\infty} a_n^{pt} \bar{x}^{n+1} \tag{101}$$

Away from the tip of the adherend, a Taylor Series expansion can be used.

$$\bar{F} = \sum_{n=0}^{\infty} (a_n + a_n^{pt})(\bar{x} - \bar{x}_i)^n \tag{102}$$

The adhesive stresses in the scarf joint, including load transfer stresses and joint extension stresses, can be calculated as follows.

$$\sigma_{xx} = E_{adhes} \frac{F}{w(t_{adher} - \frac{t_{adhes}}{\cos\alpha})E_{xlam}} \tag{103}$$

$$\sigma_{11tot} = \frac{1}{2}\{1+\cos(-2\alpha)\}\sigma_{xx} \tag{104}$$

$$\tau_{12tot} = -\frac{1}{2}\sin(-2\alpha)\sigma_{xx} + K_{str}\frac{F\cos\alpha\sin\alpha}{wt_{adher}} \tag{105}$$

$$\sigma_{22tot} = \frac{1}{2}\{1+\cos(\pi-2\alpha)\}\sigma_{xx} + K_{str}\frac{F\cos\alpha\sin\alpha\tan\alpha}{wt_{adher}} \tag{106}$$

where K_{str} is the stress concentration factor for a particular location in the joint.

The maximum stresses follow

$$\tau_{\max} = \sqrt{\sigma_{11tot}{}^{2} + (\frac{\sigma_{11tot} - \sigma_{22tot}}{2})^{2}} \tag{107}$$

$$\sigma_{\max} = \frac{\sigma_{11tot} + \sigma_{22tot}}{2} + \tau_{\max} \tag{108}$$

The main conclusions obtained from this investigation can be summarized as follows [24]:

- Slight bluntness in adherend tips may cause a significant reduction in joint strength due to high-stress concentrations in the adhesive.
- Stress distribution in the adhesive varies through the thickness.
- Joints with doublers on one side bend under tensile loads and may be weaker than joints that are not reinforced.

4.3 ANALYTICAL MODEL RESULTS.

Table 6 summarizes the different coupon configurations used for the repair variable investigation, their modes of failure, and the applicable analytical models, depending on the failure.

4.3.1 Laminate Models.

The laminate models used for evaluation included the Delta Design Spreadsheet, the Ten Percent Rule, and the modified Ten Percent Rule.

TABLE 6. APPLICABLE MODELS FOR THE DIFFERENT COUPON CONFIGURATIONS

Coupon Configuration	Repair Configuration	Core Cell Size	Failure Modes	Applicable Models
Large Four-Point Bending Beams	Two-Dimensional Prepreg, 350°F Cure	1/8	Compression failure of the parent laminate (failure outside the repair)	• Delta CLPT design spreadsheet • Ten Percent Rule • CACRC-improved solution
			Compression failure of the repair (failure at the center of the repair)	• Delta CLPT design spreadsheet • Ten Percent Rule • CACRC-improved solution
		3/8	Taper repair area (cohesive failure of the adhesive)	• Delta scarf joint analysis • Hart-Smith scarf joint analysis
Small Four-Point Bending Beams	One-Dimensional Wet Lay-Up, 250°F Cure	1/8	Compression failure of the repair laminate (failure in the scarf or in the middle of the repair)	• Delta CLPT design spreadsheet • Ten Percent Rule • CACRC-improved solution • SUBLAM
		3/8		
	One-Dimensional Prepreg, 250°F Cure	3/8	Core shear failure	• Test for core shear stress and core shear allowable
Unidirectional Tension Coupons	One-Dimensional Prepreg, 250°F Cure	1/8	Taper repair area (tension failure of the repaired laminate)	• Delta CLPT design spreadsheet • Ten Percent Rule • CACRC-improved solution • SUBLAM
	One-Dimensional Wet Lay-Up, 250°F Cure			
	One-Dimensional Prepreg, 250°F Cure	3/8		
	One-Dimensional Wet Lay-Up, 250°F Cure			

The Delta Analysis Design Spreadsheet model uses the CLPT to compare the performance of the repair laminate to the parent laminate. CLPT is used to develop the extensional stiffness matrix [A] for both the repair and parent laminates from which the laminate properties E1, E2, and G12 can be obtained. Strength and stiffness margins of safety are then calculated from the ratio of the original laminate values and the repair laminate values. Margins of safety are obtained for longitudinal, transverse, and shear stiffnesses as follows.

$$MS(longitudinal) = \frac{E_{1,repair}}{E_{1,parent}} - 1 \tag{109}$$

$$MS(transverse) = \frac{E_{2,repair}}{E_{2,parent}} - 1 \tag{110}$$

$$MS(shear) = \frac{G_{12,repair}}{G_{12,parent}} - 1 \tag{111}$$

The CLPT is used to generate the components of the normalized compliance matrix $[a^*_{ij}]$ defined as follows.

$$\left[a^*_{ij}\right] = \left(\frac{1}{h}\left[A_{ij}\right]\right)^{-1} \text{ where } \begin{bmatrix} \varepsilon_1 \\ \varepsilon_2 \\ \varepsilon_6 \end{bmatrix} = \left[a^*_{ij}\right] \begin{bmatrix} \sigma_1 \\ \sigma_2 \\ \sigma_6 \end{bmatrix} \tag{112}$$

From the above matrix, stresses are applied in the longitudinal and transverse directions, both in tension and compression until the allowable strains are reached, in which case, failure is said to have occurred. These stresses are then converted to stress resultants, and a laminate strength margin of safety for tension, compression, and shear loading is obtained as follows.

$$MS(repair) = \frac{q_{repair}}{q_{parent}} - 1 \tag{113}$$

However, the matrix described by equation 111 only evaluates the on-axis or shear failure of the 0° or 90° plies. To evaluate the on-axis or shear failure of the ±45° plies, the laminate stiffness matrix is transformed using the following equations.

$$\begin{aligned}\overline{A}_{11} = {} & A_{11}\cos^4\theta + 2(A_{12} + 2A_{66})\sin^2\theta\cos^2\theta + A_{22}\sin^4\theta - 4A_{16}\sin\theta\cos^3\theta - \\ & 4A_{26}\sin^3\theta\cos\theta\end{aligned} \tag{114}$$

$$\begin{aligned}\overline{A}_{12} = {} & \left(A_{11} + A_{22} - 4A_{66}\right)\sin^2\theta\cos^2\theta + A_{12}(\sin^4\theta + \cos^4\theta) + 2(A_{16} - A_{26})\sin\theta\cos^3\theta + \\ & 2(A_{26} - A_{16})\sin^3\theta\cos\theta\end{aligned} \tag{115}$$

$$\begin{aligned}\overline{A}_{22} = {} & A_{11}\sin^4\theta + 2(A_{12} + 2A_{66})\sin^2\theta\cos^2\theta + A_{22}\cos^4\theta + 4A_{16}\sin^3\theta\cos\theta + \\ & 4A_{26}\sin\theta\cos^3\theta\end{aligned} \tag{116}$$

$$\begin{aligned}\overline{A}_{16} = {} & (A_{11} - A_{12} - 2A_{66})\sin\theta\cos^3\theta + (A_{12} - A_{22} + 2A_{66})\sin^3\theta\cos\theta + \\ & 4(A_{26} - A_{16})\sin^2\theta\cos^2\theta + A_{16}\cos^4\theta - A_{26}\sin^4\theta\end{aligned} \tag{117}$$

$$\begin{aligned}\overline{A}_{26} = {} & (A_{11} - A_{12} - 2A_{66})\sin^3\theta\cos\theta + (A_{12} - A_{22} + 2A_{66})\sin\theta\cos^3\theta + \\ & 4(A_{16} - A_{26})\sin^2\theta\cos^2\theta + A_{16}\cos^4\theta - A_{26}\sin^4\theta\end{aligned} \tag{118}$$

$$\begin{aligned}\overline{A}_{66} = {} & (A_{11} + A_{22} - 2A_{12} - 2A_{66})\sin^2\theta\cos^2\theta + A_{66}(\sin^4\theta + \cos^4\theta) + \\ & 2(A_{16} - A_{26})\sin\theta\cos^3\theta + 2(A_{26} - A_{16})\sin^3\theta\cos\theta\end{aligned} \tag{119}$$

Therefore, for the ±45° plies, the on-axis failure can be calculated as follows

$$\begin{bmatrix}\varepsilon_1\\ \varepsilon_2\\ \varepsilon_6\end{bmatrix} = [a^*_{ij}]_{45^o}\begin{bmatrix}\sigma_1\\ \sigma_2\\ \sigma_6\end{bmatrix} \text{ where } [a^*_{ij}]_{45^o} = \left(\frac{1}{h}[\overline{A}_{ij}]\right)^{-1} \tag{120}$$

Failure occurs when one of the plies reaches its strain allowable as a result of the applied stress. The model generates ultimate stress resultants for the parent and the repaired structure in the 0°, 90°, and 45° directions that are subsequently converted to applied loads, depending on the loading condition.

This model is usually used by airlines when the loads are not known; therefore, three directions (45, 90, and 0) are checked, assuming the principal loads are in that direction. For this exercise, the load is known and is in the 0 degree direction. Hence, only the 0/90 degree direction is checked.

As shown in the table 6, laminate models can be applied to the 1/8-inch core large four-point bending beams, the small four-point bending beams repaired with the wet lay-up material system, and all the unidirectional tension coupons. The results predicted by the laminate models for the large four-point bending beams are summarized in figure 74.

Figure 74 shows the laminate models load predictions for the 1/8-inch core large four-point bending beams. As previously mentioned, failure in these beams occurred in the laminate; therefore, it is appropriate to verify whether the model predictions matched the experimental results. The experimental data shown represents average points and not individual ones. This data is also shown in figure 32, with the actual scatter obtained experimentally.

As shown in figure 74, the Delta Design Spreadsheet yielded the most accurate results with a percent error of less than 5%. The predictions obtained were a function of the failure strains input into the program. These values were not available; therefore, assumptions were made about what those values would be. The failure strains used were 9000 microstrain for tension loading and 7000 microstrain for compression loading.

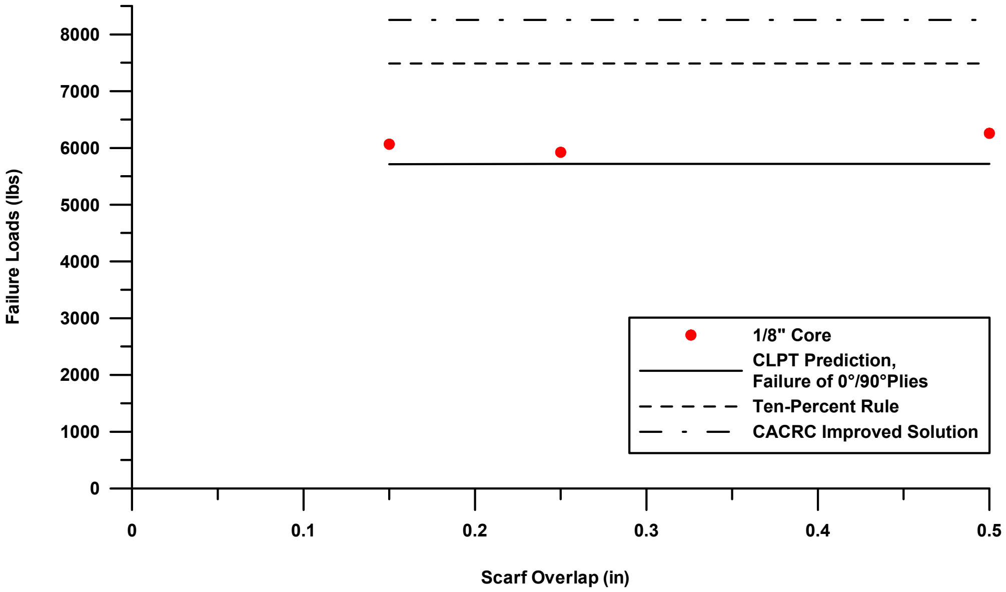

FIGURE 74. LAMINATE MODELS FAILURE LOAD PREDICTIONS COMPARED WITH EXPERIMENTAL DATA FOR THE 1/8-inch CORE LARGE FOUR-POINT BENDING BEAMS

The Ten Percent Rule yielded less accurate results than the Delta Design Spreadsheet with failure loads about 23% higher than the experimental data, and the CACRC-improved solution yielded the least precise results with failure loads about 38% higher than the average experimental data. The failure loads predicted by the Ten Percent Rule and the CACRC-improved solution were dependent upon the material properties input and since similar material properties were used instead of the actual ones, which were not available, this could be a reason for the discrepancies found. Furthermore, both the Ten Percent Rule and the CACRC-improved solution calculate stress resultants in tension and compression as a fraction of the ultimate tensile and compressive strength values. The results obtained indicate that the compressive strength values used for the repair material may be higher than the actual values.

Furthermore, one needs to remember that these are laminate models used to predict failure in a sandwich structure. Laminate properties will always be higher than facesheet properties due to the difference in pressure applied during the cure, i.e., the level of compaction between a pure laminate and a sandwich structure, nonuniform compaction (honeycomb walls are the only places where support is available), and the resulting waviness of the laminate, particularly in compression.

Figure 75 shows the laminate models failure load predictions for the unidirectional tension coupons repaired with the prepreg material system. The experimental data shown represents average values and not individual points. All the unidirectional tension coupons failed in the laminate, which is why the laminate model predictions were investigated. It should be noted that the failure load predictions shown were based on laminate failure strains or strengths. The maximum strains used were in the order of 9000 microstrain for the repair material. No factor of safety was embedded in this number. The Delta Design Spreadsheet and the CACRC-improved solution yielded almost identical results, underpredicting the strength of the 1/8-inch core tension coupons with a 0.25- and 0.5-inch scarf overlap by about 10% and overpredicting the strength of the 3/8-inch core coupons by about 14%. The Ten Percent Rule predictions matched the failure loads obtained for the 3/8-inch core tension coupons and underpredicted the strength of the 1/8-inch core coupons by 22%.

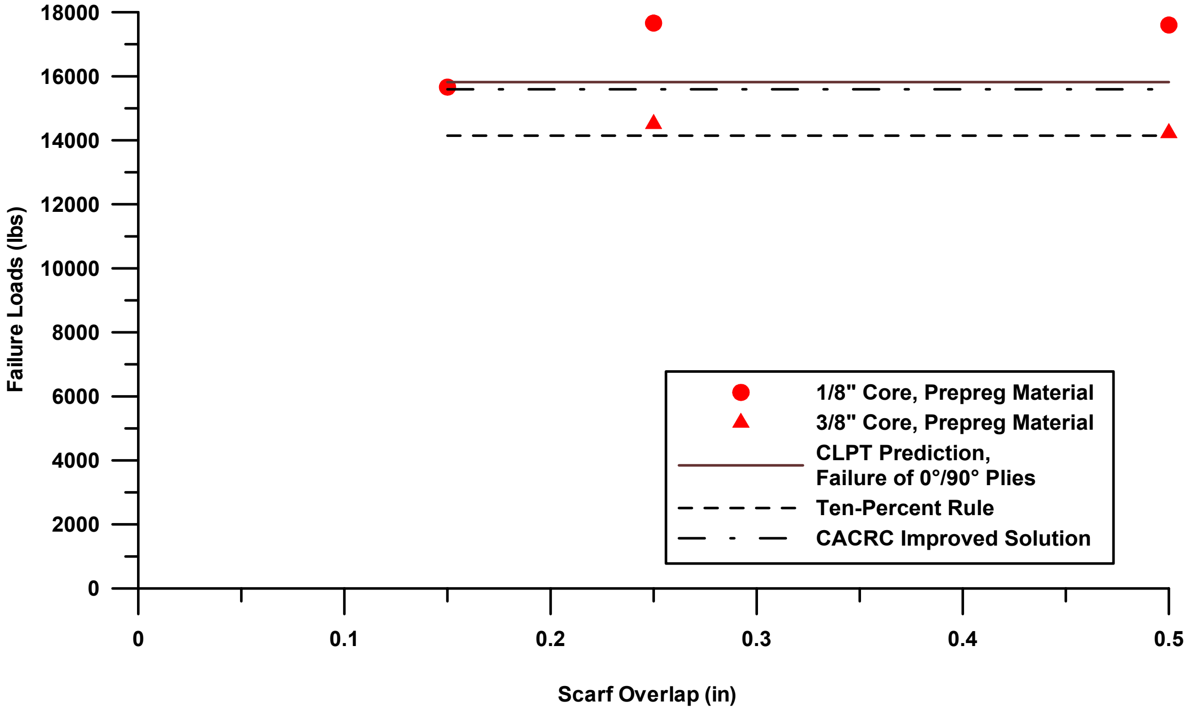

FIGURE 75. LAMINATE MODELS FAILURE LOAD PREDICTIONS COMPARED WITH EXPERIMENTAL DATA FOR THE UNIDIRECTIONAL TENSION COUPONS REPAIRED WITH THE PREPREG MATERIAL SYSTEM

Figure 76 shows the laminate models failure load predictions for the unidirectional tension coupons repaired with the wet lay-up material system. The experimental data shown represents average values and not individual points. It should be noted that the failure load predictions shown for the Delta Design Spreadsheet are based on laminate failure strains. These values were not available, therefore, a failure strain of 7000 microstrain was used for the wet lay-up repair material. The Ten Percent Rule and the CACRC-improved solution predictions were dependent upon the material properties input, mainly the ultimate tensile and compressive strengths.

The Delta Design Spreadsheet predictions, based on the CLPT, overpredicted the results by, at most, 18%. The Ten Percent Rule and the CACRC-modified solution overpredicted the strength by 45% and 63% respectively.

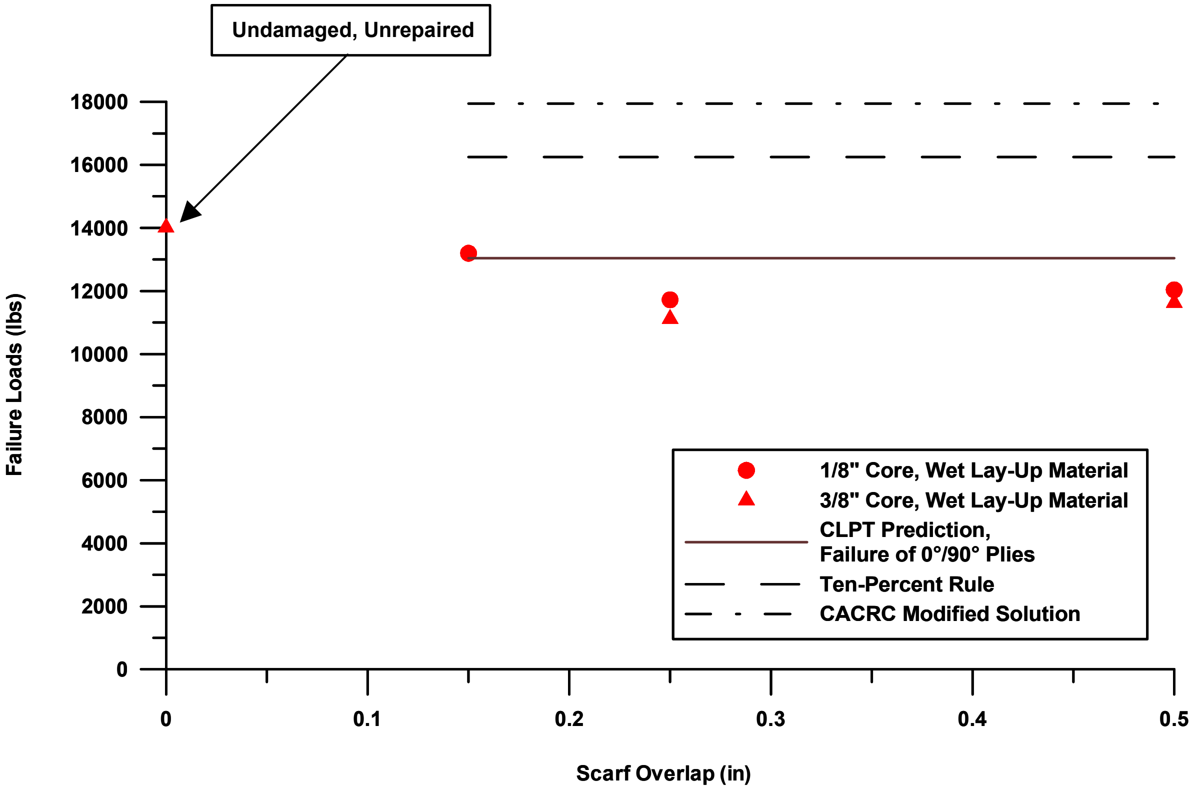

FIGURE 76. LAMINATE MODELS FAILURE LOAD PREDICTIONS COMPARED WITH EXPERIMENTAL DATA FOR THE UNIDIRECTIONAL TENSION COUPONS REPAIRED WITH THE WET LAY-UP MATERIAL SYSTEM

Figure 77 shows the laminate models load predictions for the small four-point bending beams repaired with the wet lay-up material system. The experimental data shown represents average values and not individual points. It should be noted that the failure load predictions shown for the Delta Design Spreadsheet were based on laminate failure strains. The values used for these strains were in the order of 5000 microstrain for the wet lay-up repair material. No factor of safety was embedded in this number. Using these strains to predict failure underpredicted the failure loads of the small beams by, at most, 25%.

The Ten Percent Rule and the CACRC-improved solution results overpredicted those loads by, at most, 20% and 38%.

As part of the Delta Design Spreadsheet, a simple mechanics of materials analysis was used to determine the margin of safety of the adhesively bonded scarf joints. Even if this analysis does not apply to the unidirectional tension coupons, the 1/8-inch core large beams, or the small beams repaired with the wet lay-up system, it was only used to demonstrate the safety of the joints. This method calculates the ultimate shear capacity based on maximum adhesive shear strength, thickness of the laminate, and scarf angle. The maximum adhesive shear strength is obtained from the ASTM D 5656 thick-adherend structural tests. This value is then compared to the allowable strength of the plies, and a margin of safety for the adhesive joint is deduced as follows.

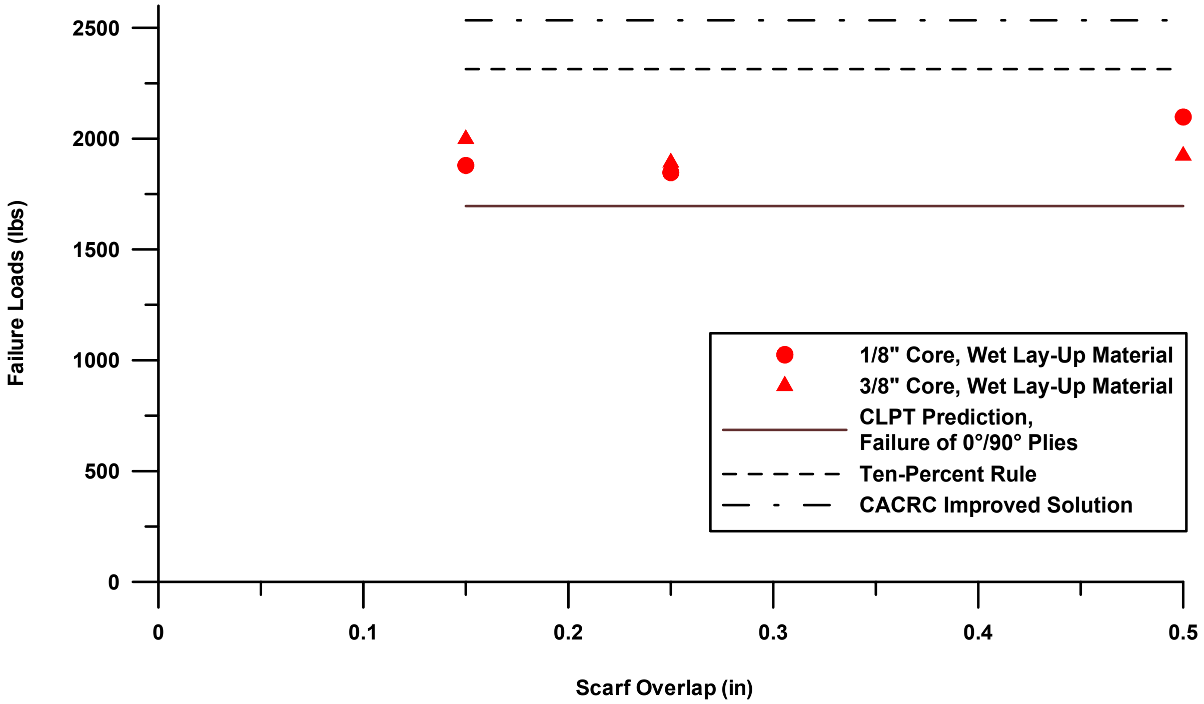

FIGURE 77. LAMINATE MODELS FAILURE LOAD PREDICTIONS COMPARED WITH EXPERIMENTAL DATA FOR THE SMALL FOUR-POINT BENDING COUPONS REPAIRED WITH THE WET LAY-UP MATERIAL SYSTEM

$$MS(bondline) = \frac{q_{ultimate,shear}}{q_{original} \times 1.15} - 1 \qquad (121)$$

where

$$q_{ultimate,shear} = \frac{2 * t_{parent} * \tau_{adhesive}}{\sin 2\theta} \qquad (122)$$

and $q_{original}$ is the actual maximum load obtained from the laminate analysis. It is the ultimate laminate load in tension, compression or shear, whichever is most critical. As previously mentioned, the scarf adhesive joint should never become the weak link, i.e., its strength should always exceed that of the adherends by at least 50%. Furthermore, all margins of safety obtained for repairs that failed in the laminate exceeded 50% regardless of the scarf overlap, which proves that the adhesive will not become the weak link and, therefore, confirms the structural integrity of these bonded joints.

4.3.2 Analysis of Scarf Joints.

The only coupons that clearly failed in the adhesive bondline were the 3/8-inch core large four-point bending beams. As was shown in figure 40, the patch clearly peeled at the taper repair area. Therefore, scarf joint models were used to verify the shear strength of the adhesive with respect to the ultimate strength of the laminate. A margin of safety of at least 50% is required, i.e., the adhesive strength needs to be at least 50% higher than the strength of the adherends to avoid a failure in the adhesive.

Two models were used for this purpose: the Delta Design Spreadsheet strength model based on a mechanics of materials approach and Hart-Smith's model described in section 4.2.7.2 which takes into account stiffness imbalance and thermal mismatch. The margin of safety used for the Delta Design Spreadsheet joint model was calculated using equation 121. For Hart-Smith's model, the critical potential bond shear stress ratio was calculated from which an allowable running load was deduced. This value was divided by the ultimate compressive failure load of the laminate to obtain a margin of safety.

For both models considered, the margins of safety obtained for the adhesive exceeded 50%, which theoretically excludes a possible failure in the adhesive. In an attempt to understand why these coupons failed in the core, even though the theory excluded the possibility of a core failure, one can examine the results obtained for the same large beams with a smaller core cell size. All of these coupons failed either in the repair laminate or in the parent laminate, as the theory predicted. It should be emphasized that the large four-point bending beams were all manufactured at the same time, with the same materials and processes. The only difference between the coupons was the core cell size and properties. According to the adhesive models, the adhesive exceeds by far the strength of the adherends; therefore, failure should occur in the adherends, which was the case for the 1/8-inch core coupons. Failure in the adhesive for the 3/8-inch core coupons was at the interface of the repair facesheet and the 3/8-inch core due to the small bonded interface area, which causes high peel stresses. As previously mentioned, the larger the core cell size, the smaller the bonded interface area and, therefore, the higher the peel stresses.

In summary, the outcome of the results obtained by the model was dependent on the material properties used. Since some of the properties were not available, values from previous research studies were used. These values did not necessarily reproduce the actual materials and processes used for this study. Furthermore, laminate models base failure on pure tension or compression loading modes, with the main assumption of small deformations, and do not take into account bending effects, which involve large deformations. Therefore, some discrepancies could result from using pure compression failure results to represent a compression failure due to bending. Finally, the core effects are not embedded in the model, which could lead to additional inaccuracies.

4.3.3 Material Science Corporation SUBLAM Analysis Code.

This model uses plate theory to represent the cross section of a composite structure. Since plain strain theory is used, the cross section of the structure needs to be constant in the x direction. Furthermore, this model requires an extensive number of material properties, and some of them were not available. As a consequence, assumptions were made about what those properties would be, and therefore, the solutions presented are dependent upon the values chosen. Assumptions were also made about the Poisson's ratio and the elastic modulus of the adhesive [25].

Figures 78, 79, and 80 show the different components used to construct the repaired unidirectional tension coupon models. Due to symmetry, only half of the coupons was modeled. The model was constrained in all degrees of freedom at $y = 0$, and a tensile load of magnitude $F/2$ was applied at ($y = L/2$, $z = \pm h/2$), where h is the thickness of the coupon and L its length. The model was initially constructed with only one element in the taper repair area and then reconstructed with three elements in the scarf area. Refining the mesh at the taper repair area significantly improved the results.

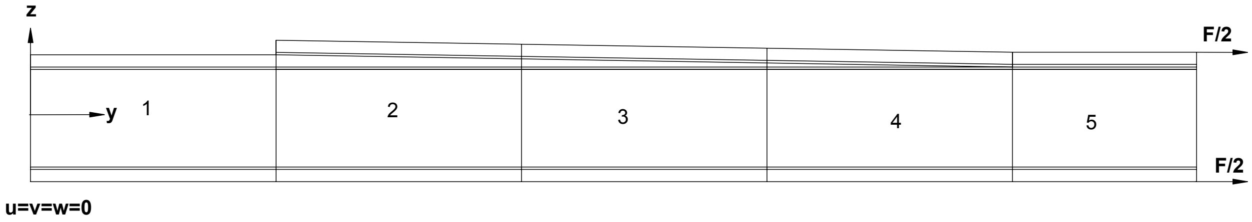

FIGURE 78. SUBLAM MODEL OF A UNIDIRECTIONAL TENSION COUPON WITH A 0.50-inch SCARF REPAIR

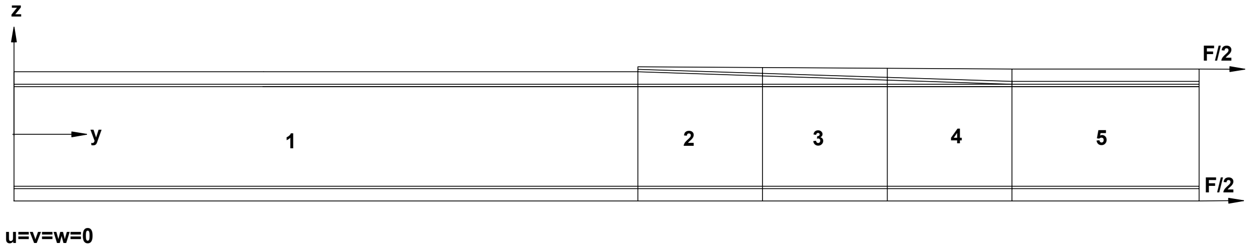

FIGURE 79. SUBLAM MODEL OF A UNIDIRECTIONAL TENSION COUPON WITH A 0.25-inch SCARF REPAIR

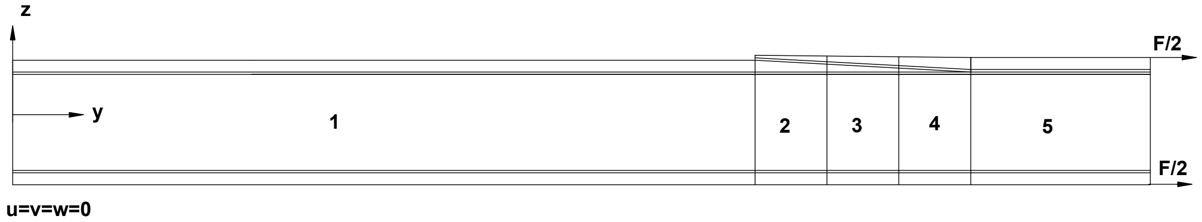

FIGURE 80. SUBLAM MODEL OF A UNIDIRECTIONAL TENSION COUPON WITH A 0.15-inch SCARF REPAIR

Different input files were generated for each of the different unidirectional tension coupon configurations considered. These configurations included two different cores and three different scarf ratios. Five elements were used to model this particular loading condition, each element contained a number of sublaminates stacked together vertically and each sublaminate represented a particular component of the sandwich structure with its corresponding thickness and material properties. In an element, sublaminates were connected using interfaces, and every interface was defined as the line connecting two nodes. Continuity of displacements and traction forces was fulfilled at the element interconnections. Displacement and force boundary conditions were then applied at specific nodes to represent the actual physical problem. The model was then analyzed using the SUBLAM code, and a series of output files containing the analyzed data was generated. The data consisted of x, y, and z displacements, as well as extensional and shear stresses and strains as a function of spatial position.

The unidirectional tension results obtained using SUBLAM are summarized in the following paragraphs.

Figure 81 shows plots of the strains obtained in the laminate scarf region as a function of spatial position for the 1/8-inch core unidirectional tension coupons repaired with the 250°F cure prepreg material system. It should be noted that all the coupons with this specific configuration failed in the laminate scarf region, which is why the strains in that region were plotted. Furthermore, for symmetry purposes, only half of the repair was modeled; therefore, only the scarf region in one-half of the repair is shown. The zero position corresponds to the edge of the scarf, moving towards the center of the repair. In other words, the zero position corresponds to the edge of ply 3, i.e., the last ply in the scarf. The end of the scarf, i.e., positions 0.45, 0.75, and 1.5, correspond to the flat region where the repair meets the core of the structure.

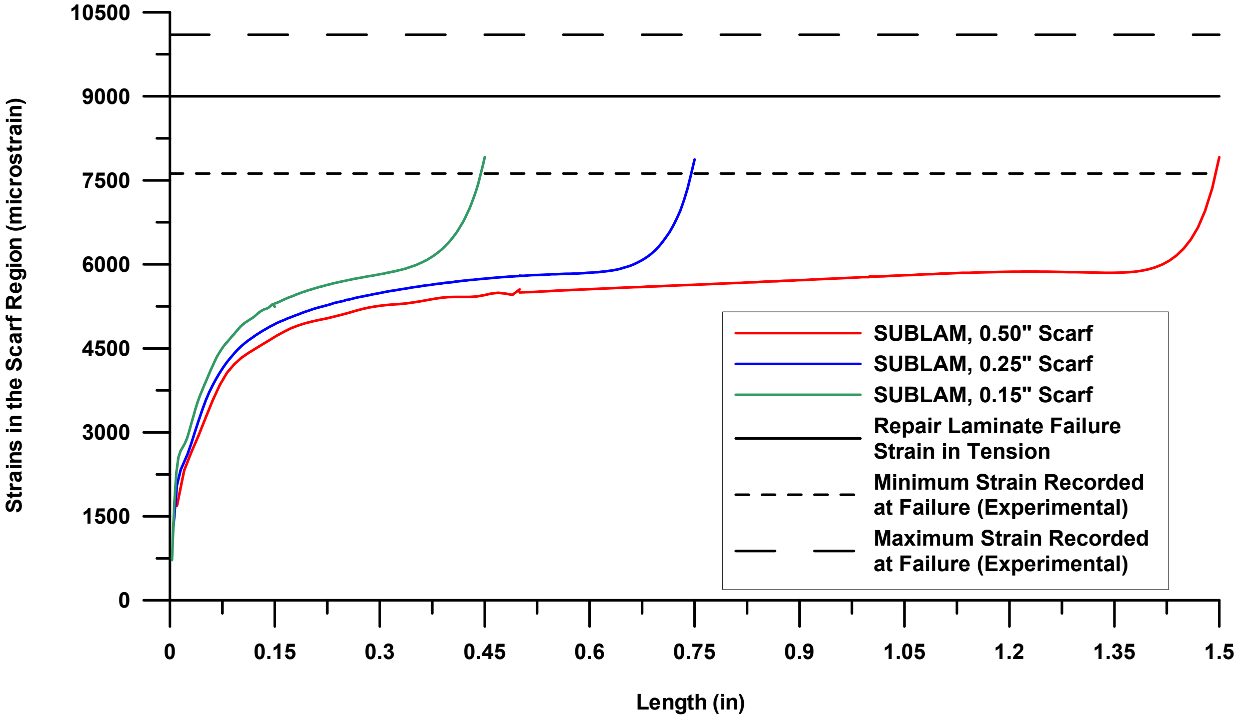

FIGURE 81. COMPARISON BETWEEN FAILURE STRAINS FOR THE REPAIR AND STRAINS RECORDED EXPERIMENTALLY FOR THE 1/8-inch CORE UNIDIRECTIONAL TENSION COUPONS (PREPREG REPAIR)

Also shown in figure 81 is the failure strain of the repair laminate. This value is an ultimate value and, therefore, does not have a factor of safety embedded in it. The minimum and maximum strains in the scarf laminate, obtained experimentally using ARAMIS, are also shown. These strains were obtained by plotting sections of the repair scarf just before failure and determining the minimum and maximum strains in that region just before failure for all the coupons tested. These minimum and maximum values were then averaged and plotted on the graph. As can be seen, the failure strains predicted by SUBLAM were conservative, 12.5% lower than the ultimate strains. However, they barely exceeded the minimum failure strains recorded experimentally. This demonstrates that SUBLAM predictions for this case were very conservative.

Figures 82 and 83 are shown for illustration purposes only. The failure mode of the unidirectional tension coupons was a laminate failure and not an adhesive one; therefore, these figures are shown to demonstrate that the peak stresses in the adhesive did not exceed the adhesive strength, i.e., its plastic shear stress, obtained using ASTM D 5656 thick-adherend tests. Figure 82 shows the adhesive shear strain as a function of spatial position for the three scarf overlaps.

Figure 83 shows the adhesive shear stress as a function of spatial position for three scarf configurations. As shown, the average shear strain and stress in the 0.50-inch scarf is very low. The average shear strain and stress in the scarf increases as the scarf overlap becomes smaller. Furthermore, peak strains and stresses in the scarf increase as the size of the scarf becomes smaller. This would cause failure to initiate in a smaller repair faster than it would in a larger one. In other words, stress concentrations are lower in a larger scarf repair.

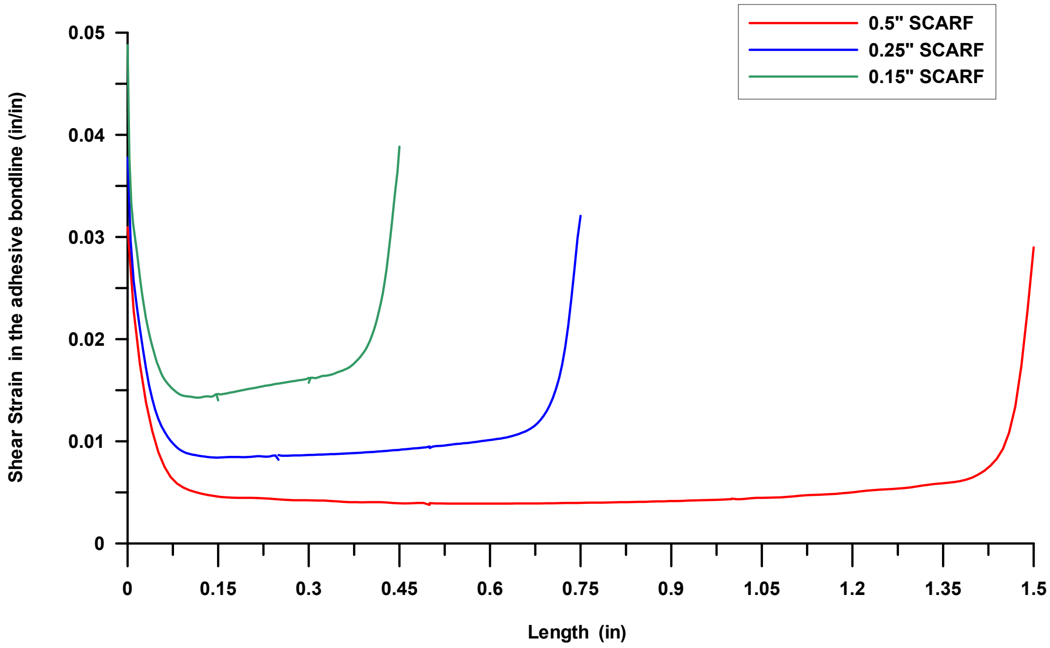

FIGURE 82. SHEAR STRAIN IN THE ADHESIVE BONDLINE FOR DIFFERENT SCARF REPAIRS ON 1/8-inch CORE UNIDIRECTIONAL TENSION COUPONS (PREPREG REPAIR)

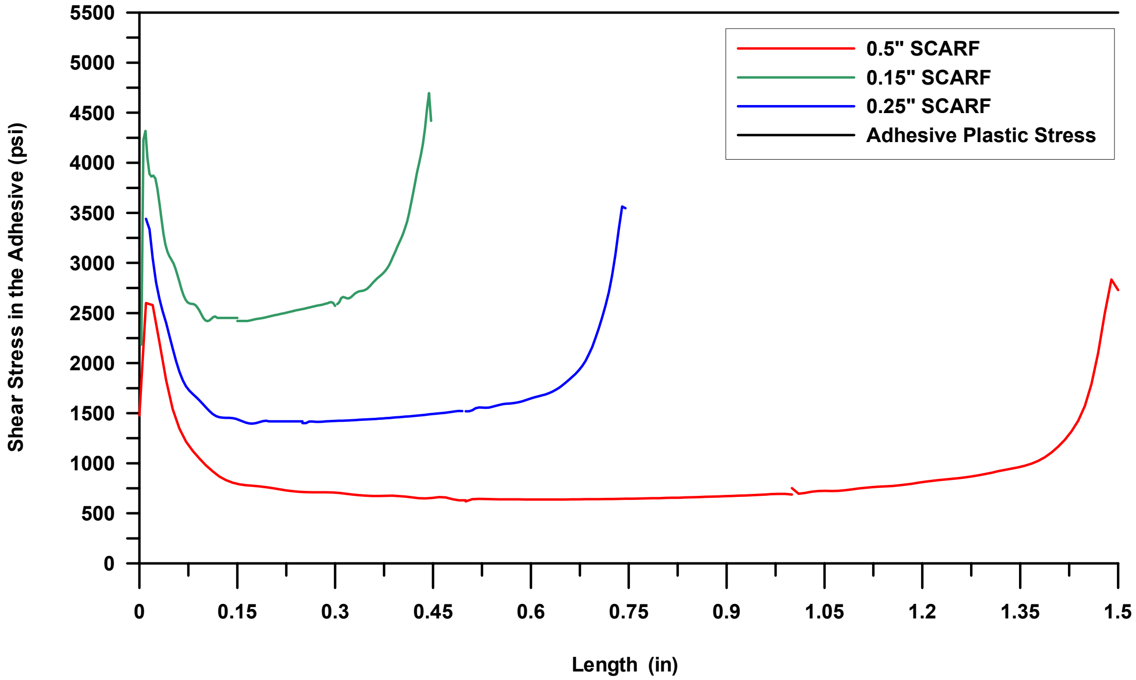

FIGURE 83. SHEAR STRESS IN THE ADHESIVE BONDLINE FOR DIFFERENT SCARF REPAIRS ON THE 1/8-inch CORE UNIDIRECTIONAL TENSION COUPONS (PREPREG REPAIR)

Figure 84 shows a comparison between the ultimate strains predicted by the SUBLAM code, the failure strains for the repair laminate in tension, and the strains obtained experimentally. As previously mentioned, the plotted values represent strains in the laminate scarf region just before failure. These values were plotted for the 3/8-inch core unidirectional tension coupons because failure occurred in that region for these coupons. Failure strains predicted by SUBLAM were conservative but 33% lower than the ultimate strain for the repair laminate. Comparing SUBLAM results to experimental data, it was found that the model predictions matched the minimum strain values recorded experimentally in the scarf. As a consequence, SUBLAM predictions for failure were conservative.

Figures 85 and 86 are shown for illustration purposes only. Failure of the 3/8-inch core unidirectional tension coupons occurred in the laminate and not in the adhesive. Figure 85 is a plot of adhesive shear strains versus spatial position for three different scarf overlaps. Figure 86 shows plots of the adhesive shear stresses as a function of spatial position for three different scarf overlaps. This figure demonstrates that bondline shear stresses did not exceed the ultimate strength of the adhesive, obtained using ASTM D 5656 thick-adherend tests.

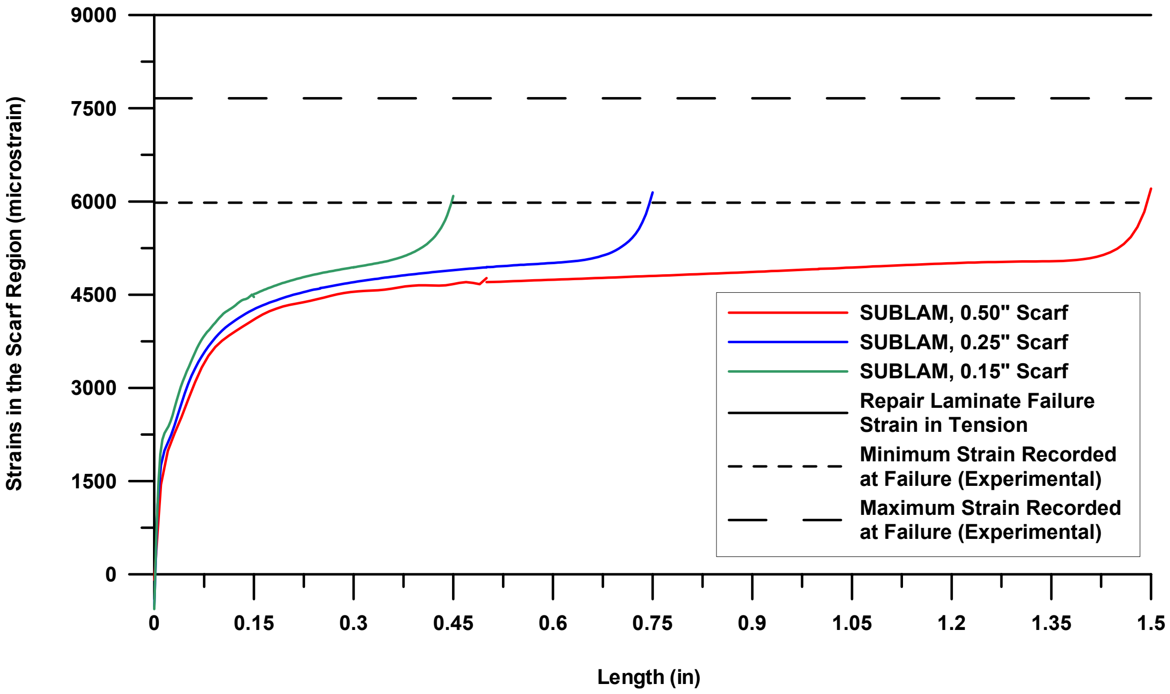

FIGURE 84. COMPARISON BETWEEN FAILURE STRAINS FOR THE REPAIR AND STRAINS RECORDED EXPERIMENTALLY FOR THE 3/8-inch CORE UNIDIRECTIONAL TENSION COUPONS (PREPREG REPAIR)

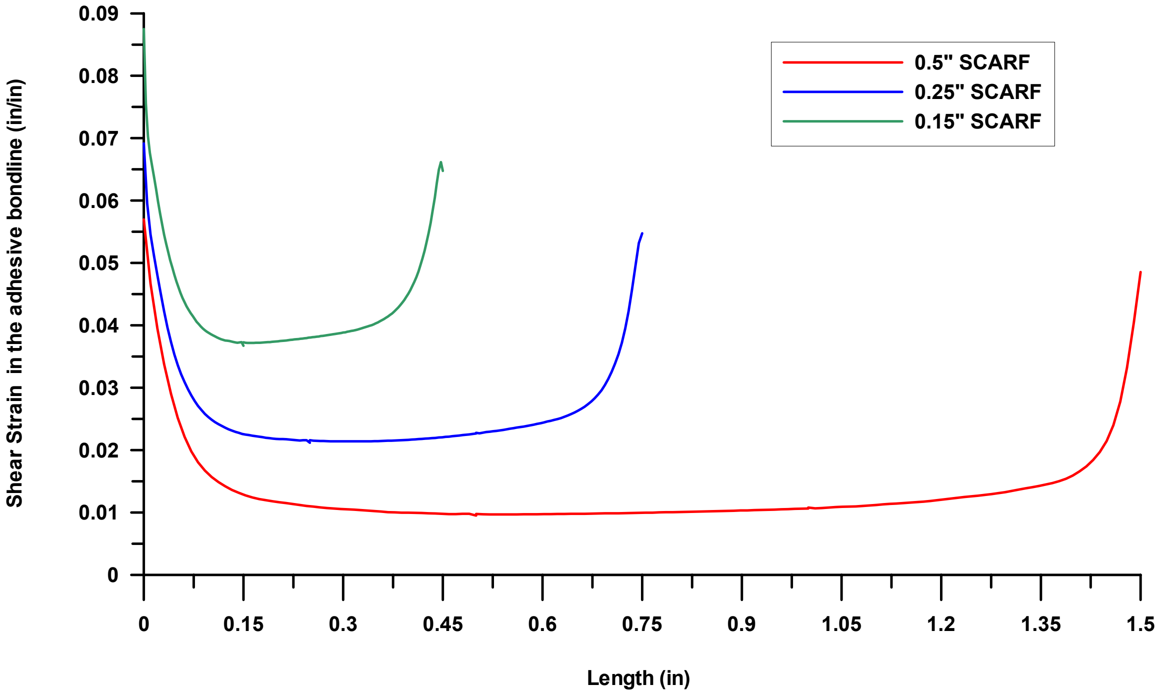

FIGURE 85. SHEAR STRAIN IN THE ADHESIVE BONDLINE FOR DIFFERENT SCARF REPAIRS ON THE 3/8-inch CORE UNIDIRECTIONAL TENSION COUPONS (PREPREG REPAIR)

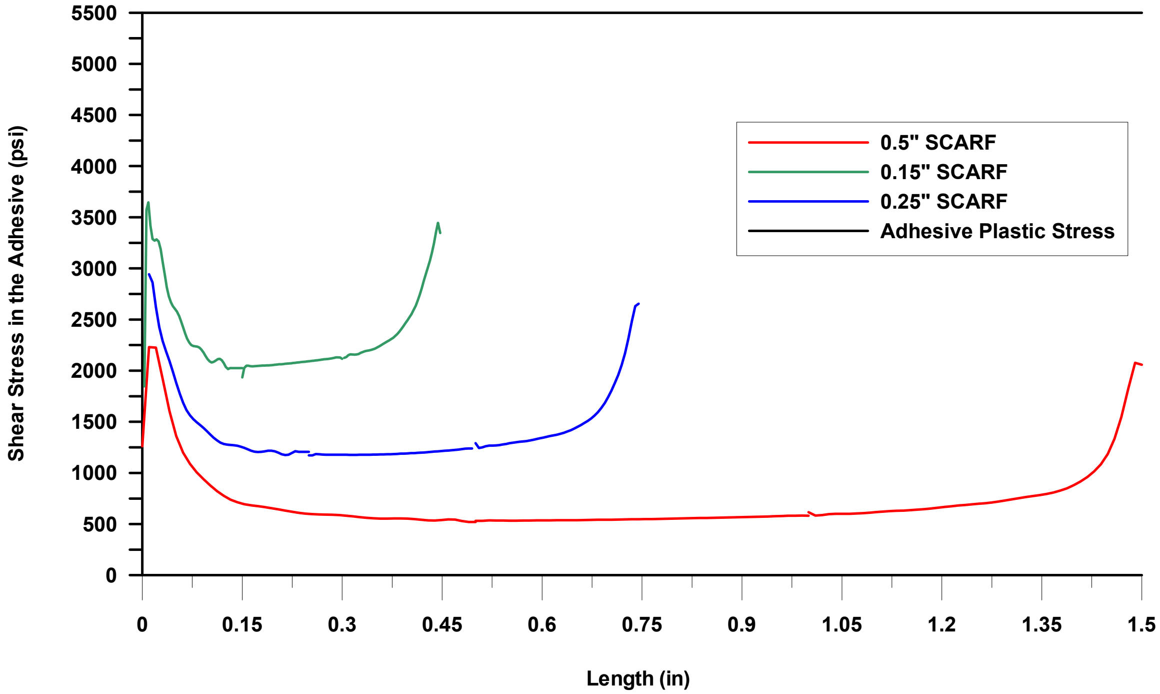

FIGURE 86. SHEAR STRESS IN THE ADHESIVE BONDLINE FOR DIFFERENT SCARF REPAIRS ON THE 3/8-inch CORE UNIDIRECTIONAL TENSION COUPONS (PREPREG REPAIR)

Figure 87 shows ultimate strain predictions, using the SUBLAM code, compared with strain values obtained experimentally as well as failure strains of the repair laminate. The strains shown are those in the scarf laminate region. Model predictions were very conservative and yielded failure strains about 14% lower than ultimate strain values for the laminate in tension. Furthermore, the peak strains predicted by SUBLAM matched minimum strains in the scarf laminate recorded at failure, using the ARAMIS system. This demonstrates that the SUBLAM method is conservative and is appropriate to use for failure prediction of these coupons.

Figures 88 and 89 are shown for illustration purposes only. Figure 88 shows the bondline shear strain for three different repair configurations. Figure 89 shows shear stresses in the adhesive bondline for three different scarf overlaps compared to the adhesive strength obtained experimentally using ASTM D 5656 thick-adherend tests. This figure also shows that for all three repair sizes considered, the plastic strength of the adhesive was not exceeded.

Figure 90 shows the SUBLAM code ultimate strain predictions for three different scarf overlaps. This figure also shows the minimum and maximum strains obtained experimentally in the scarf laminate before failure and also the ultimate strain of the repair laminate material in tension. SUBLAM predictions were very conservative. The model strains were 11% lower than the minimum strains recorded experimentally and 35% lower than the ultimate strains of the repair material in tension.

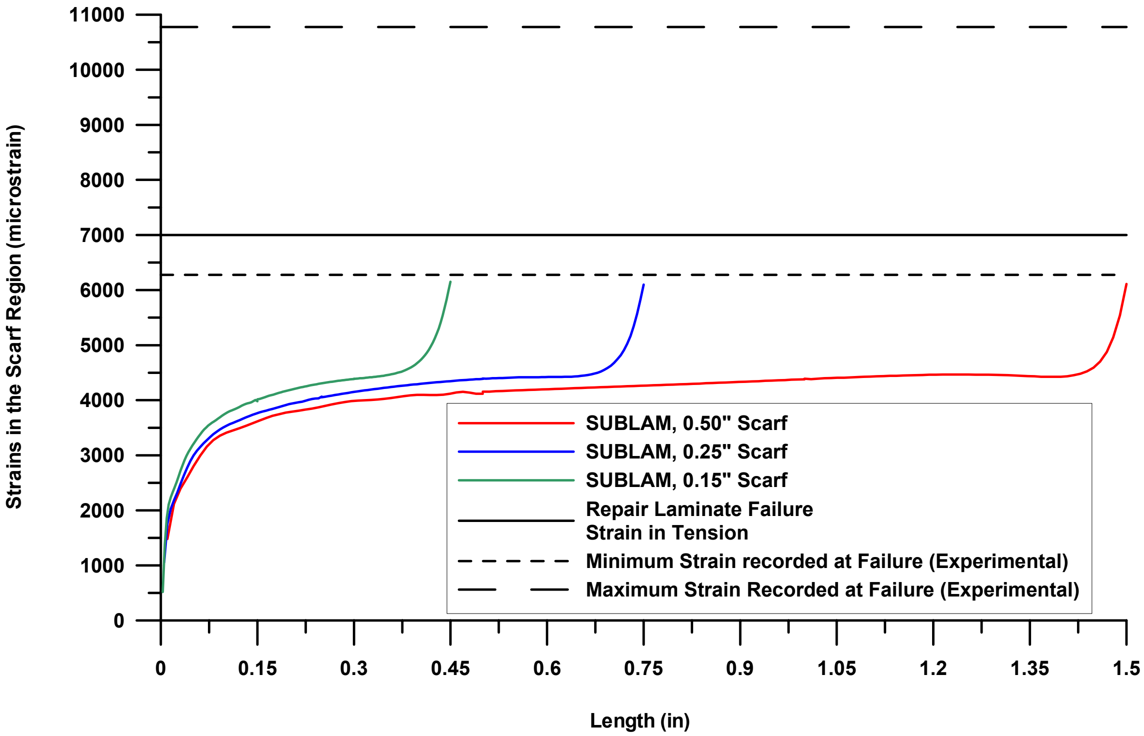

FIGURE 87. COMPARISON BETWEEN FAILURE STRAINS FOR THE REPAIR AND STRAINS RECORDED EXPERIMENTALLY FOR THE 1/8-inch CORE UNIDIRECTIONAL TENSION COUPONS (WET LAY-UP REPAIR)

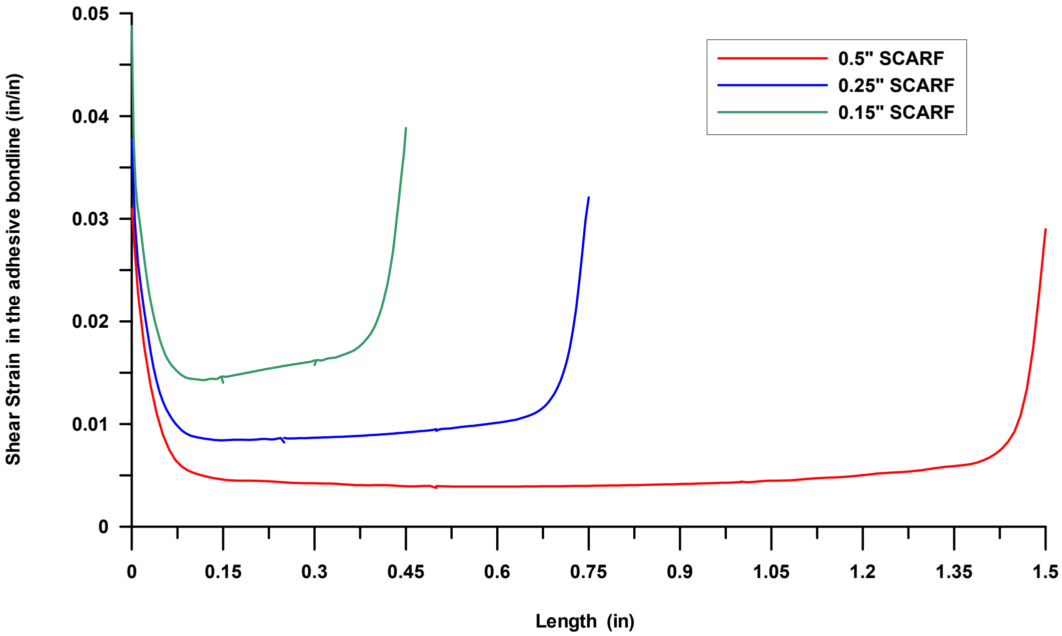

FIGURE 88. SHEAR STRAIN IN THE ADHESIVE BONDLINE FOR DIFFERENT SCARF REPAIRS ON THE 1/8-inch CORE UNIDIRECTIONAL TENSION COUPONS (WET LAY-UP REPAIR)

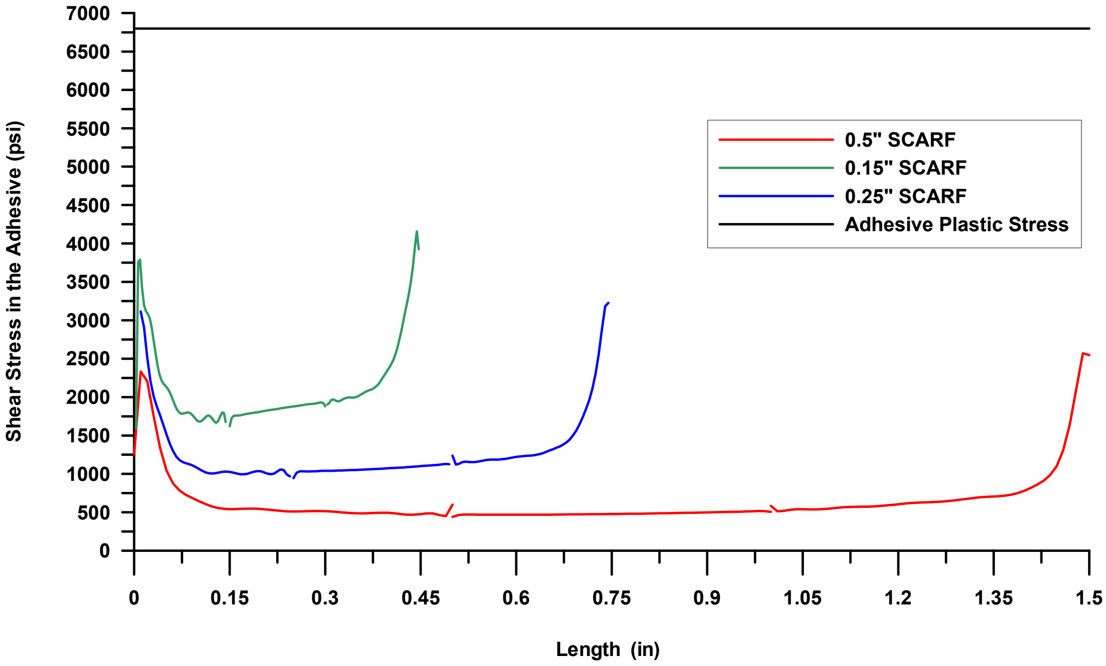

FIGURE 89. SHEAR STRESS IN THE ADHESIVE BONDLINE FOR DIFFERENT SCARF REPAIRS ON THE 1/8-inch CORE UNIDIRECTIONAL TENSION COUPONS (WET LAY-UP REPAIR)

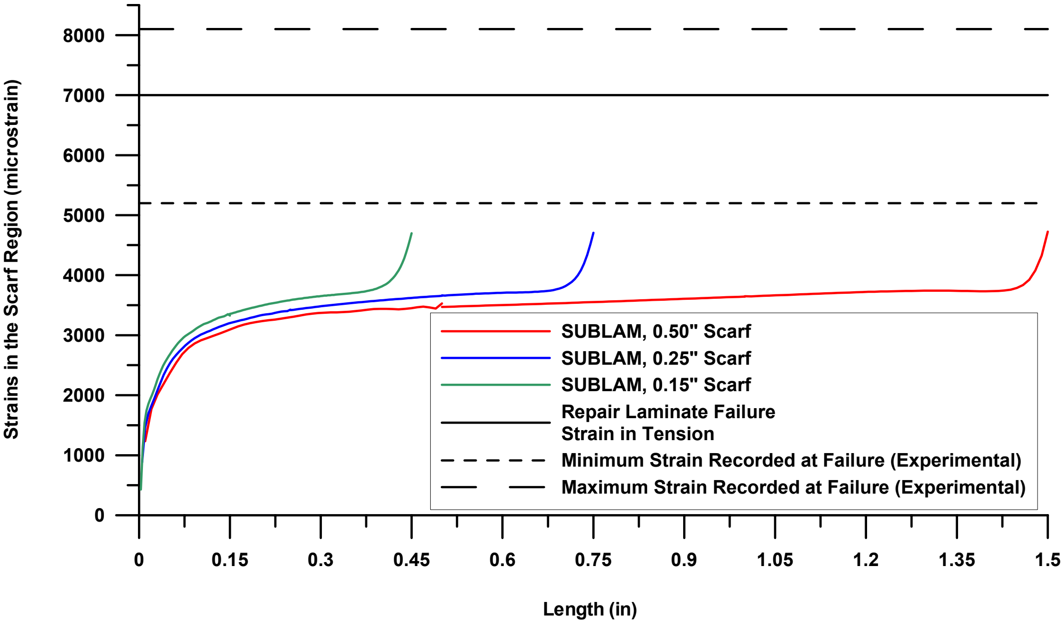

FIGURE 90. COMPARISON BETWEEN FAILURE STRAINS FOR THE REPAIR AND STRAINS RECORDED EXPERIMENTALLY FOR THE 3/8-inch CORE UNIDIRECTIONAL TENSION COUPONS (WET LAY-UP REPAIR)

For the 3/8-inch core unidirectional tension coupons, failure did not occur in the adhesive. However, stresses and strains in the adhesive are plotted in figures 91 and 92 to demonstrate that the adhesive strength, obtained using ASTM D 5656 adherend tests, was not exceeded.

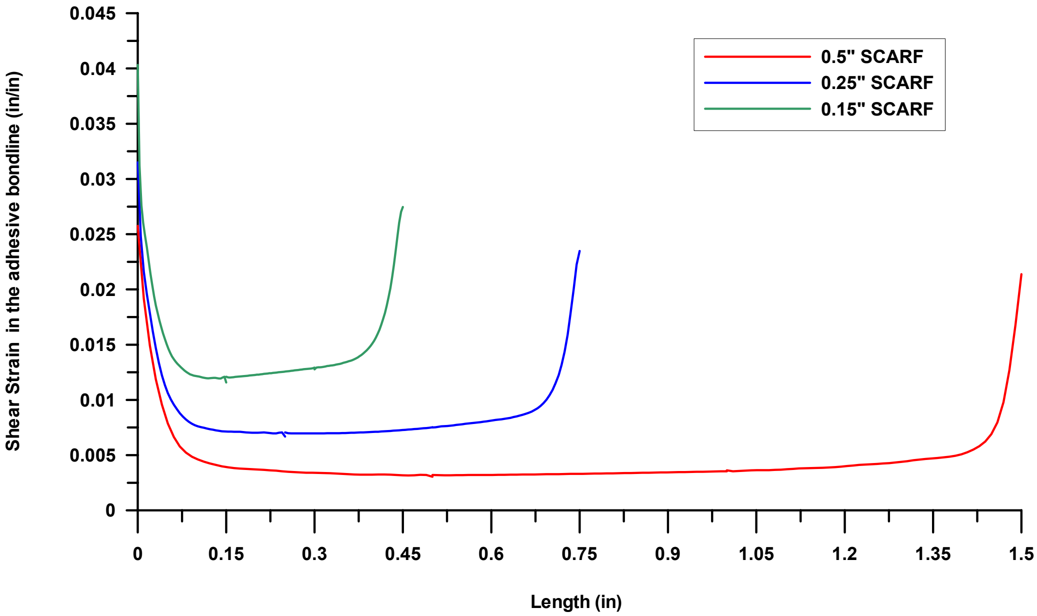

FIGURE 91. SHEAR STRAIN IN THE ADHESIVE BONDLINE FOR DIFFERENT SCARF REPAIRS ON THE 3/8-inch CORE UNIDIRECTIONAL TENSION COUPONS (WET LAY-UP REPAIR)

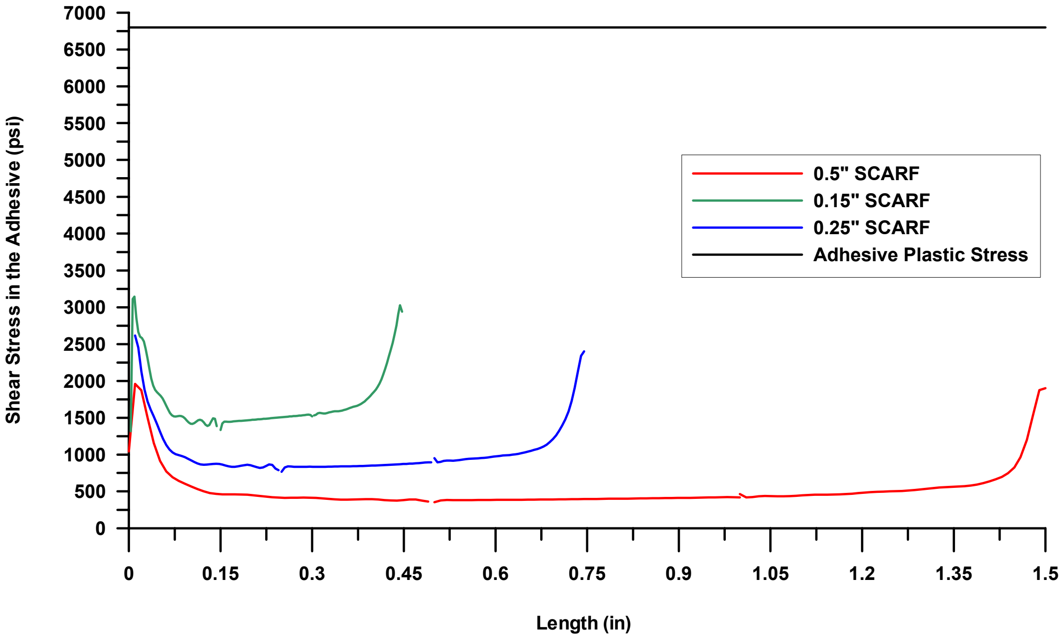

FIGURE 92. SHEAR STRESS IN THE ADHESIVE BONDLINE FOR DIFFERENT SCARF REPAIRS ON THE 3/8-inch CORE UNIDIRECTIONAL TENSION COUPONS (WET LAY-UP REPAIR)

Using the SUBLAM code, the small beams were modeled as follows.

As for the unidirectional tension coupons, only half of the small beams is modeled due to symmetry. This is shown in figures 93, 94, and 95. Displacement constraints are applied at $y = 0$ and $y = L/2$, and a point load equal to half of the actuator load was applied at $y = 3.25$.

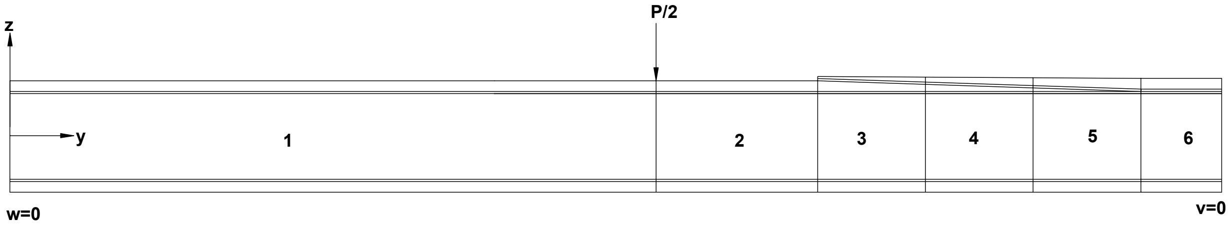

FIGURE 93. SUBLAM MODEL OF A SMALL FOUR-POINT BENDING COUPON WITH A 0.50-inch SCARF REPAIR

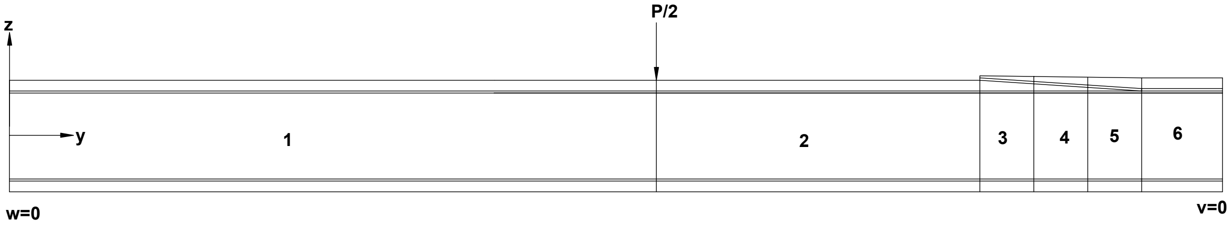

FIGURE 94. SUBLAM MODEL OF A SMALL FOUR-POINT BENDING COUPON WITH A 0.25-inch SCARF REPAIR

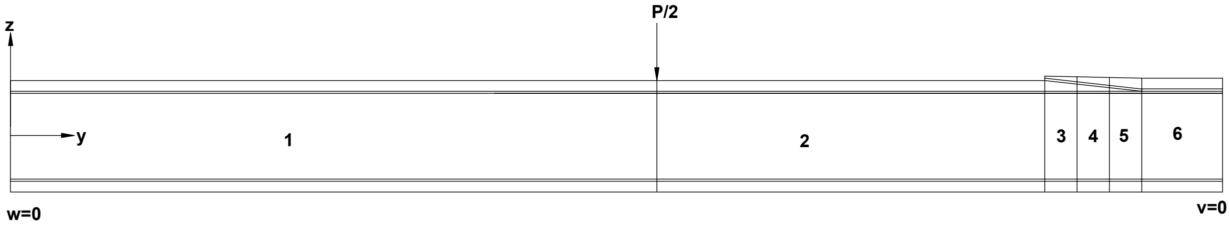

FIGURE 95. SUBLAM MODEL OF A SMALL FOUR-POINT BENDING COUPON WITH A 0.15-inch SCARF REPAIR

Figures 96 and 97 show actuator loads versus strains in the middle of the repair and strains in the middle of the parent structure (bottom facesheet), obtained experimentally and using SUBLAM for the scarf overlaps considered, for the small four-point bending beams repaired with the 250°F cure prepreg. Since failure of these coupons occurred in the core, figures 96 and 97 are shown for illustration purposes only. They simply demonstrate the level of accuracy of the model in representing the physical problem. SUBLAM predictions of strains at the center of the repair were higher than failure strains obtained experimentally for all repair sizes considered. Figure 96 shows that the larger the scarf overlap, the higher the strain at failure in the patch. The correlation between experimental data and SUBLAM was better for lower load levels than it was for high loads. At failure, the percent error in the SUBLAM data was as high as 25%.

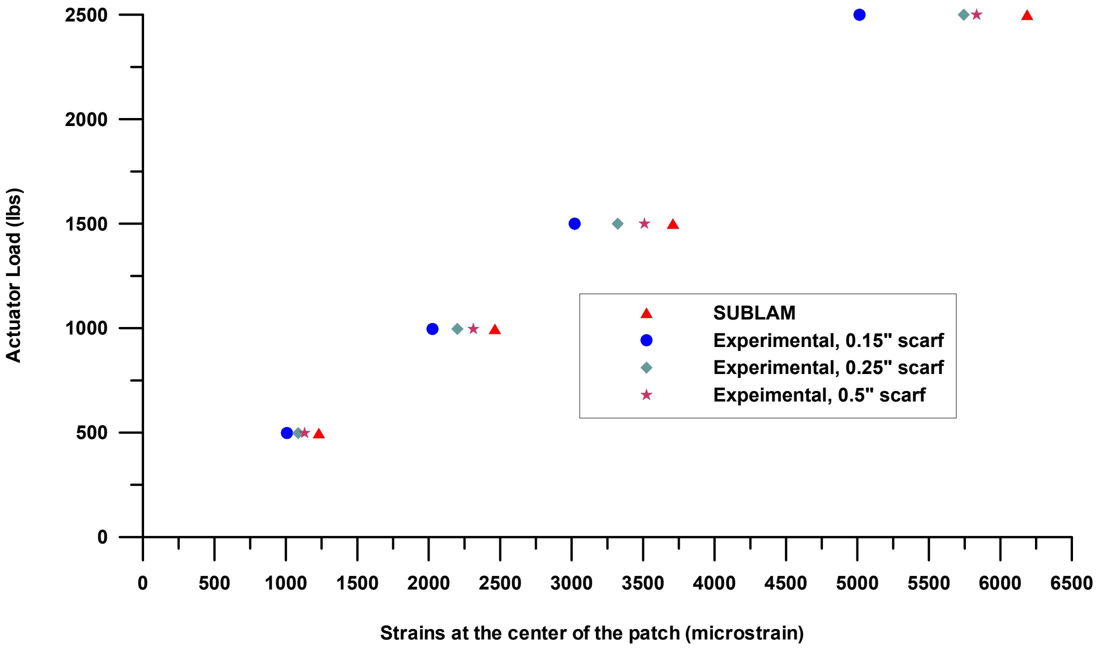

FIGURE 96. COMPARISON BETWEEN STRAINS AT THE CENTER OF THE REPAIR PATCH, OBTAINED EXPERIMENTALLY AND USING SUBLAM, FOR THE 3/8-inch CORE SMALL FOUR-POINT BENDING BEAMS (PREPREG REPAIR)

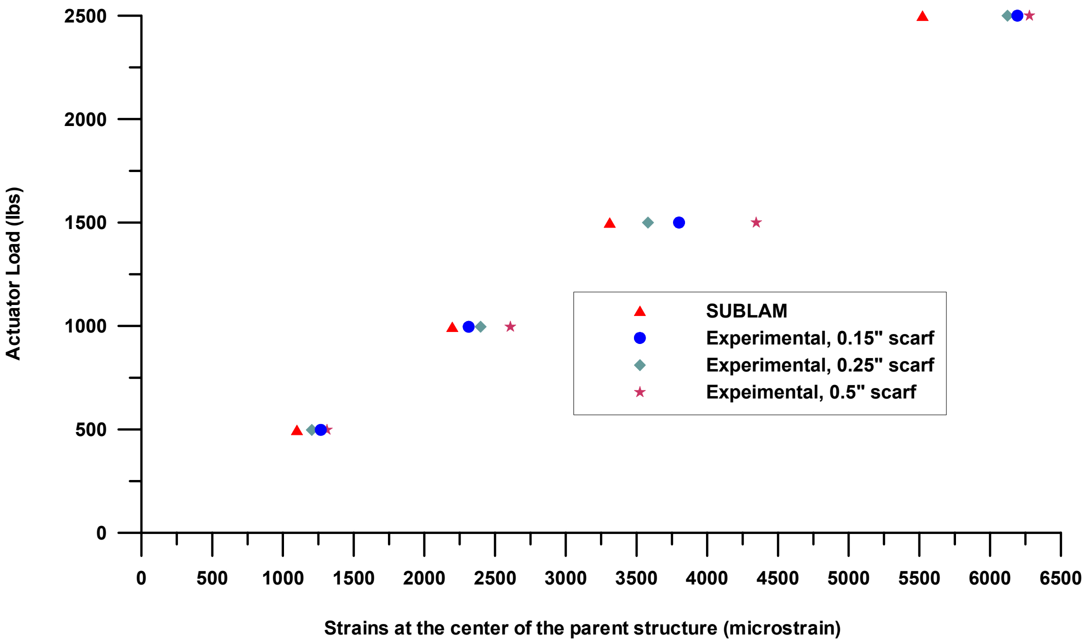

FIGURE 97. COMPARISON BETWEEN STRAINS AT THE CENTER OF THE PARENT STRUCTURE, OBTAINED EXPERIMENTALLY AND USING SUBLAM, FOR THE 3/8-inch CORE SMALL FOUR-POINT BENDING BEAMS (PREPREG REPAIR)

Similar to the strains in the center of the patch, SUBLAM predictions for strains in the parent structure (middle of the lower facesheet) were fairly accurate, even if the modeled parent structure exhibited a stiffer behavior than the actual structure. Accuracy decreased as the load was increased, and the SUBLAM percent error was, at most, 12.5% lower than strains obtained experimentally. This shows that SUBLAM's representation of the physical problem was fairly accurate.

Figure 98 shows a comparison between SUBLAM predictions of deflection and the deflections obtained experimentally for all scarf ratios considered. As can be seen, SUBLAM deflections were slightly higher than the actual deflections, with a percent error as high as 20%. The purpose of this graph is to illustrate how well the model correlated with the experimental results.

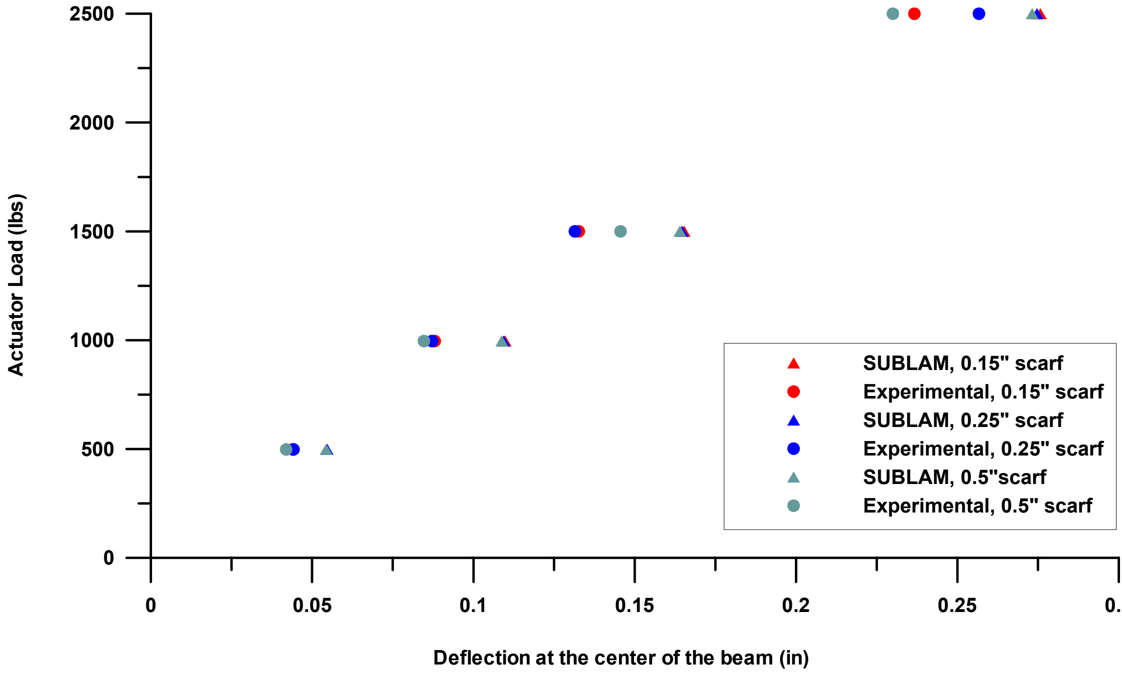

FIGURE 98. COMPARISON BETWEEN DEFLECTIONS AT THE CENTER OF THE BEAM, OBTAINED EXPERIMENTALLY AND USING SUBLAM, FOR THE 3/8-inch CORE SMALL FOUR-POINT BENDING BEAMS (PREPREG REPAIR)

Figures 99 and 100 show plots of bondline strains and stresses for all the repair configurations. It should be emphasized that the 3/8-inch core small four-point bending coupons failed in the core and not in the laminate or adhesive; therefore, figures 99 and 100 are shown only to demonstrate that the adhesive did not exceed its ultimate strength, obtained using ASTM D 5656 thick-adherend tests.

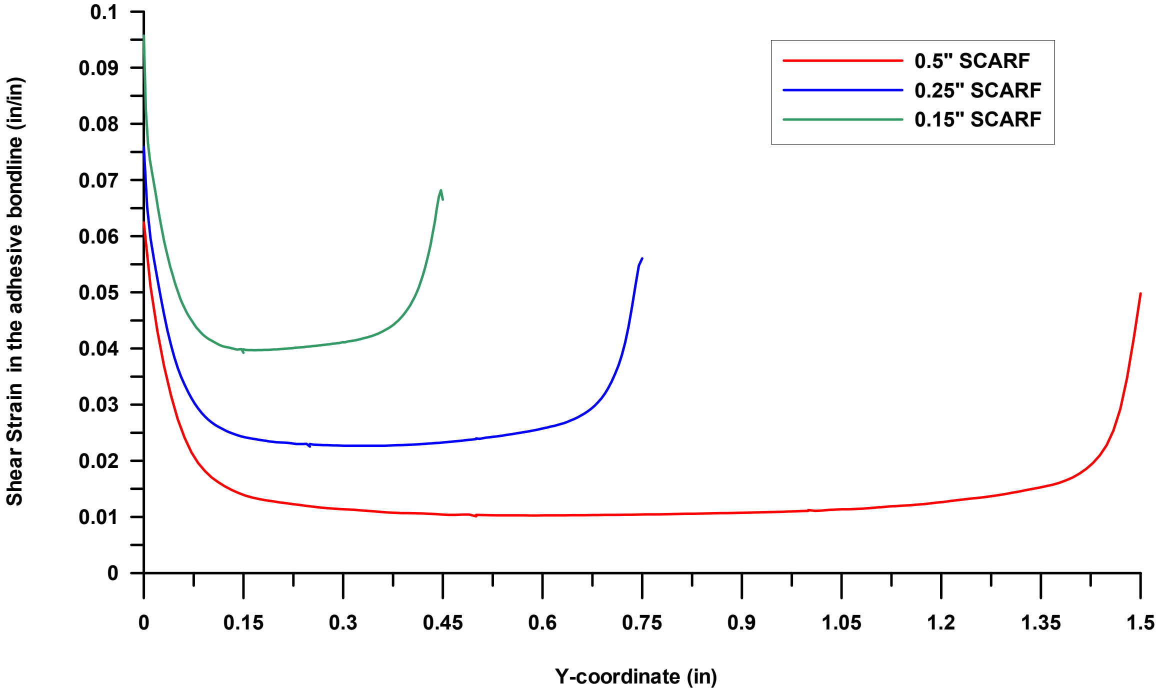

FIGURE 99. SHEAR STRAIN IN THE ADHESIVE BONDLINE FOR DIFFERENT SCARF REPAIRS ON THE 3/8-inch CORE SMALL FOUR-POINT BENDING BEAMS (PREPREG REPAIR)

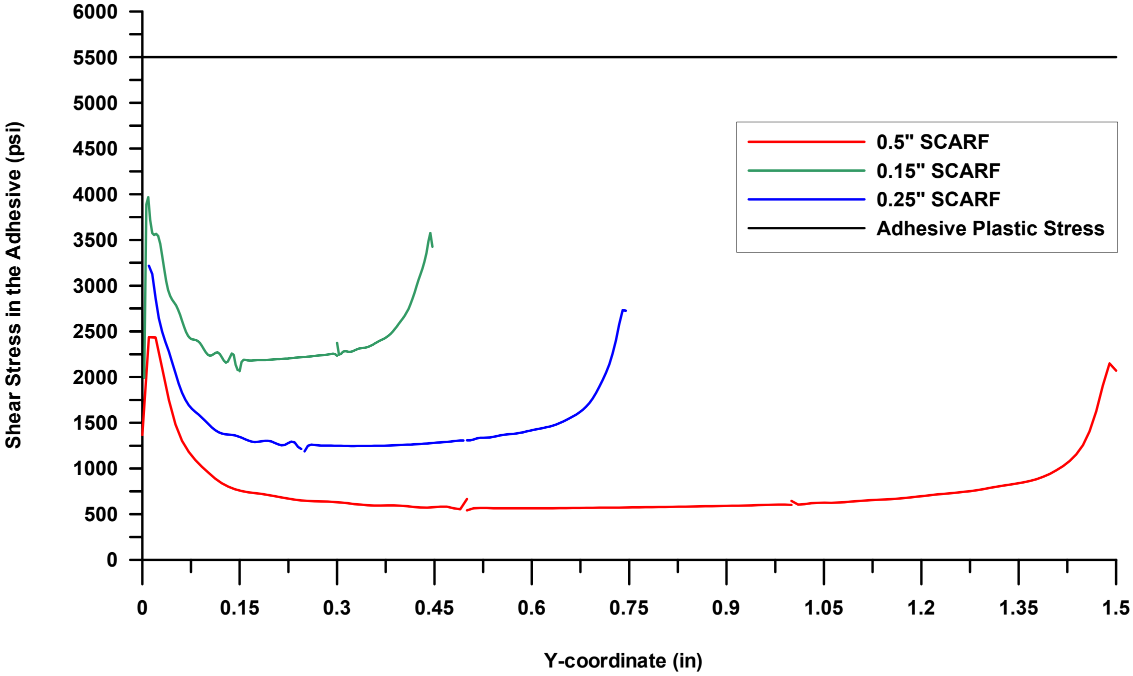

FIGURE 100. SHEAR STRESS IN THE ADHESIVE BONDLINE FOR DIFFERENT SCARF REPAIRS ON THE 3/8-inch CORE SMALL FOUR-POINT BENDING BEAMS (PREPREG REPAIR)

Figure 101 shows plots of strains in the repair predicted by SUBLAM for the 1/8-inch core small four-point bending beams repaired with a 250°F cure wet lay-up. These beams failed in the repair laminate. Strains plotted in figure 101 correspond to the deformation in the entire repair, not only in the scarf laminate region. However, for symmetry purposes, results from only half of the repair are shown. This figure also shows the ultimate strains for the repair laminate in compression. Strain data obtained from strain gages is also shown.

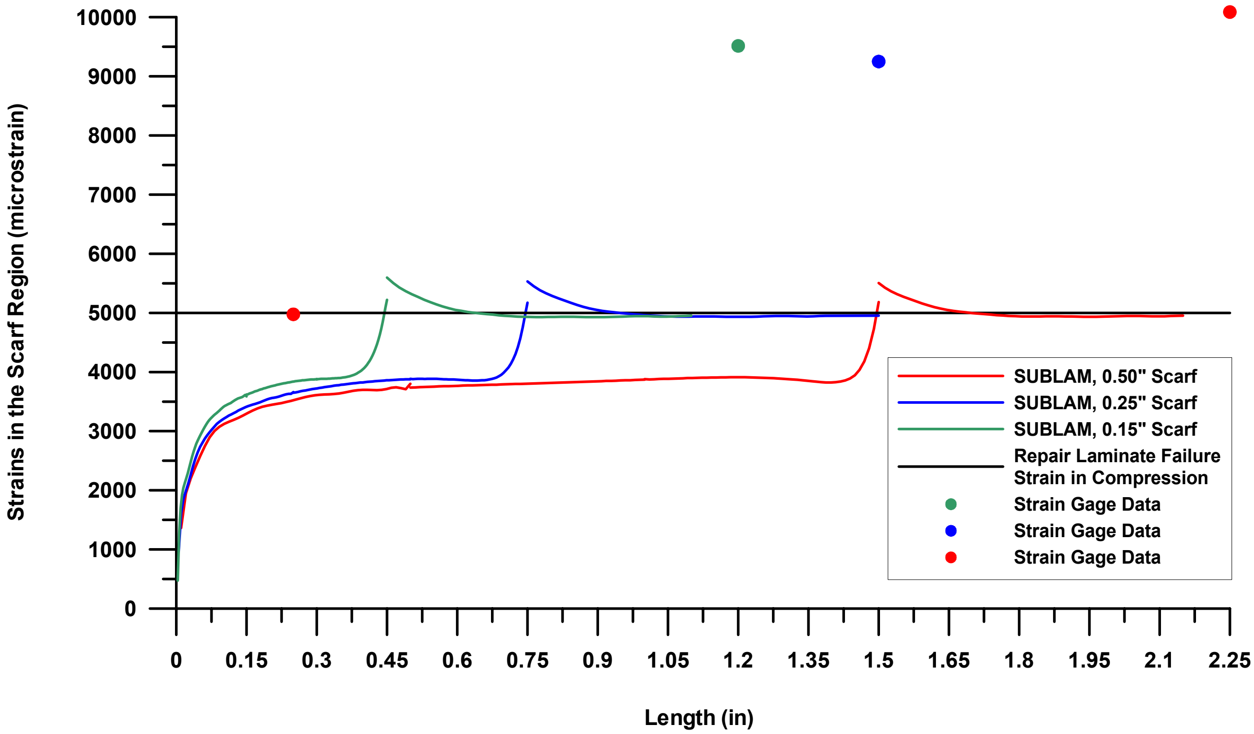

FIGURE 101. COMPARISON BETWEEN PREDICTED STRAINS FOR THE REPAIR IN COMPRESSION AND STRAINS AT FAILURE, OBTAINED EXPERIMENTALLY AND USING SUBLAM, FOR THE 1/8-inch CORE SMALL FOUR-POINT BENDING BEAMS (WET LAY-UP REPAIR)

Strain results yielded by the SUBLAM code were very conservative and lower than the ultimate repair laminate strain in compression. Strain results, obtained using SUBLAM, at the center of the repair patch matched the ultimate strain values for the repair laminate in compression.

As previously mentioned, failure of the 1/8-inch core small beams repaired with the wet lay-up system occurred in the repair patch and not in the adhesive; therefore, figures 102 and 103 are shown for verification purposes only. Figure 102 shows the shear strain distribution in the 0.15-, 0.25-, and 0.50-inch scarf overlaps considered. Figure 103 is a plot of the shear stresses in the bondline for all repair sizes considered. This figure demonstrates that at failure, the bondline peak stresses were still below the adhesive strength, obtained using ASTM D 5656 thick-adherend tests.

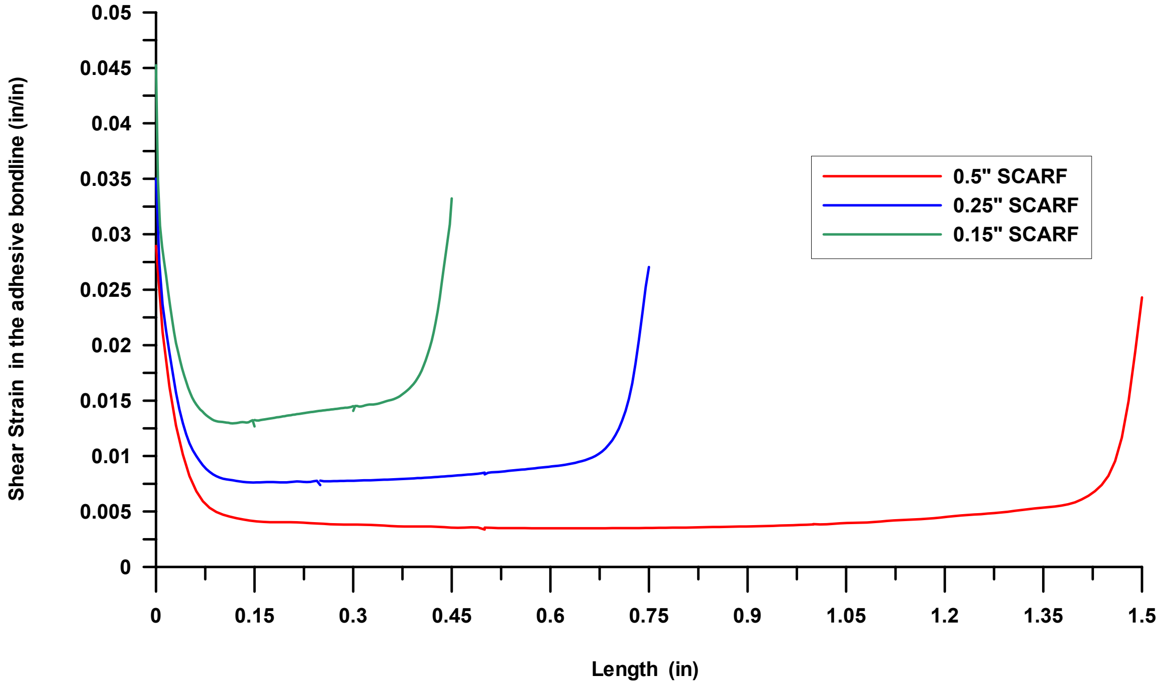

FIGURE 102. SHEAR STRAIN IN THE ADHESIVE BONDLINE FOR DIFFERENT SCARF REPAIRS CONSIDERED FOR THE 1/8-inch CORE SMALL FOUR-POINT BENDING BEAMS (WET LAY-UP REPAIR)

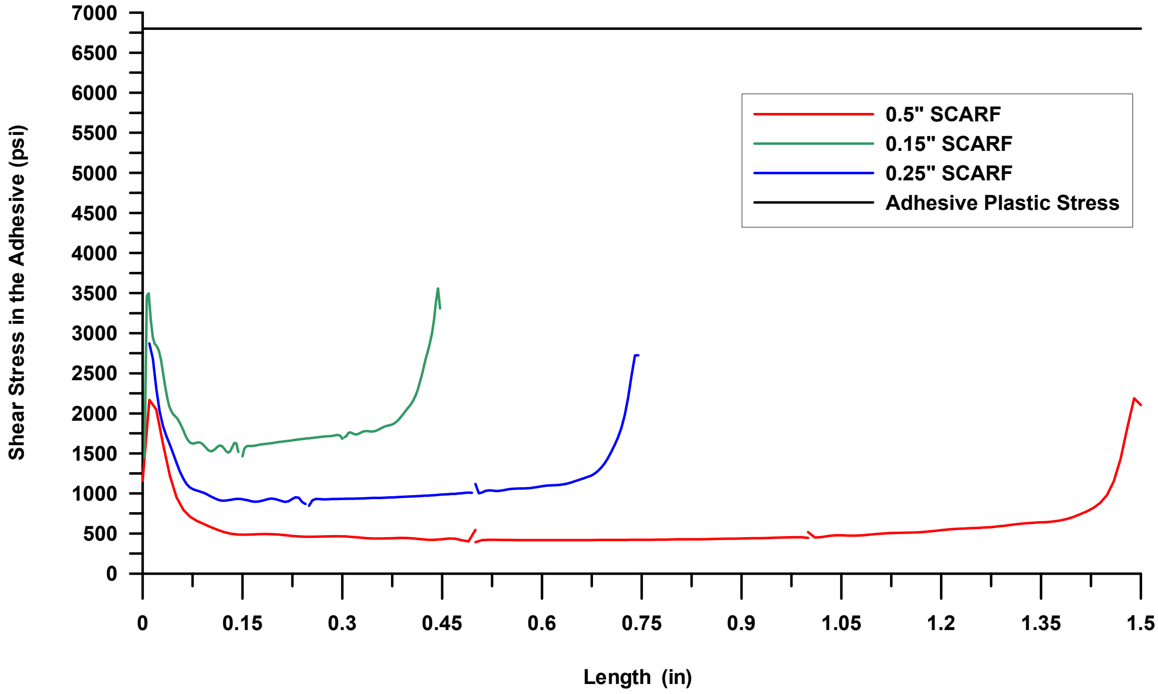

FIGURE 103. SHEAR STRESS IN THE ADHESIVE BONDLINE FOR DIFFERENT SCARF REPAIRS CONSIDERED FOR THE 1/8-inch CORE SMALL FOUR-POINT BENDING BEAMS (WET LAY-UP REPAIR)

Figure 104 shows the failure strains in the repair laminate predicted by the SUBLAM code for the 3/8-inch core small four-point bending beams repaired with the wet lay-up material system. Data is shown for the three scarf ratios considered. Also shown are the ultimate strain allowables of the repair laminate in compression and strain data, obtained experimentally using strain gages. Data obtained using SUBLAM was very conservative and was 25% lower than the ultimate strain of the repair laminate obtained analytically. For 0.15- and 0.25-inch scarf repairs, strains at the center of the patch were 11% higher than ultimate strains predicted analytically and 45% higher than strains predicted by SUBLAM.

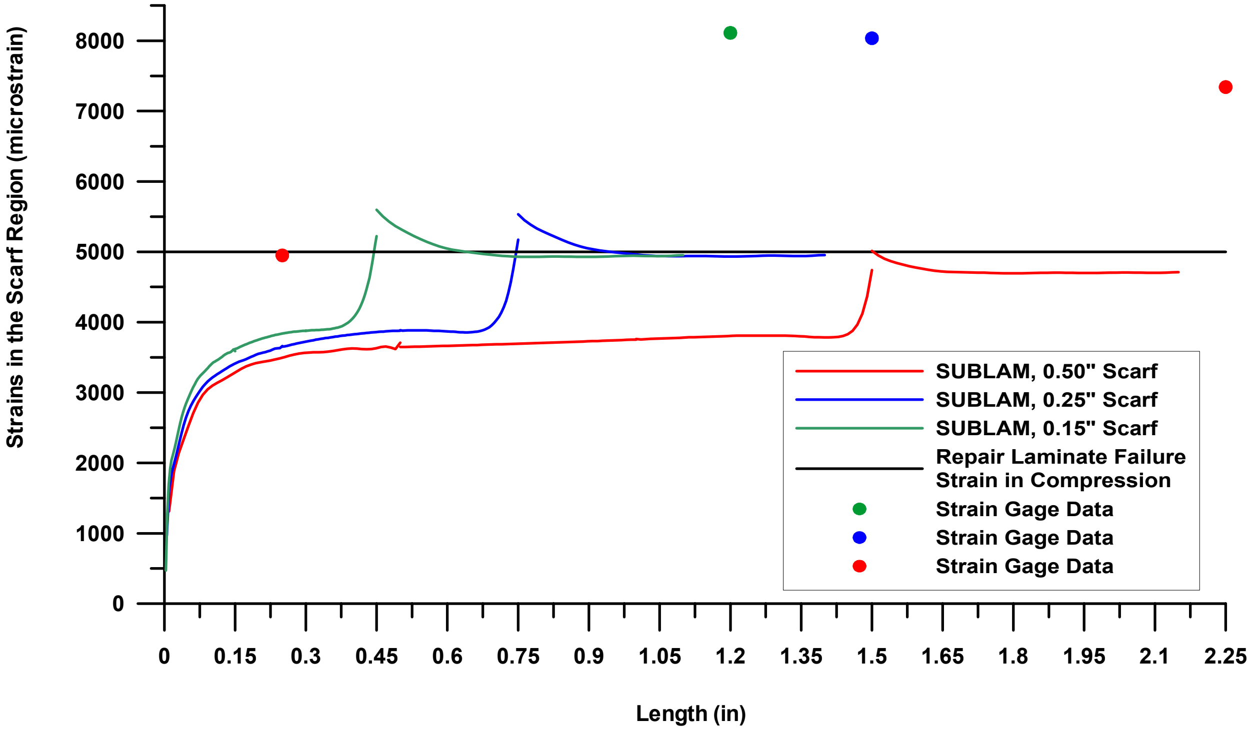

FIGURE 104. COMPARISON BETWEEN FAILURE STRAINS FOR THE REPAIR LAMINATE IN COMPRESSION AND STRAINS, RECORDED EXPERIMENTALLY, FOR THE 3/8-inch CORE SMALL FOUR-POINT BENDING BEAMS (WET LAY-UP REPAIR)

Figures 105 and 106 show shear strains and stresses in the bondline for three different scarf repairs. Figure 106 demonstrates that the failure could not have happened in the adhesive since shear stresses in the adhesive did not exceed the adhesive strength, obtained using ASTM D 5656 thick-adherend tests.

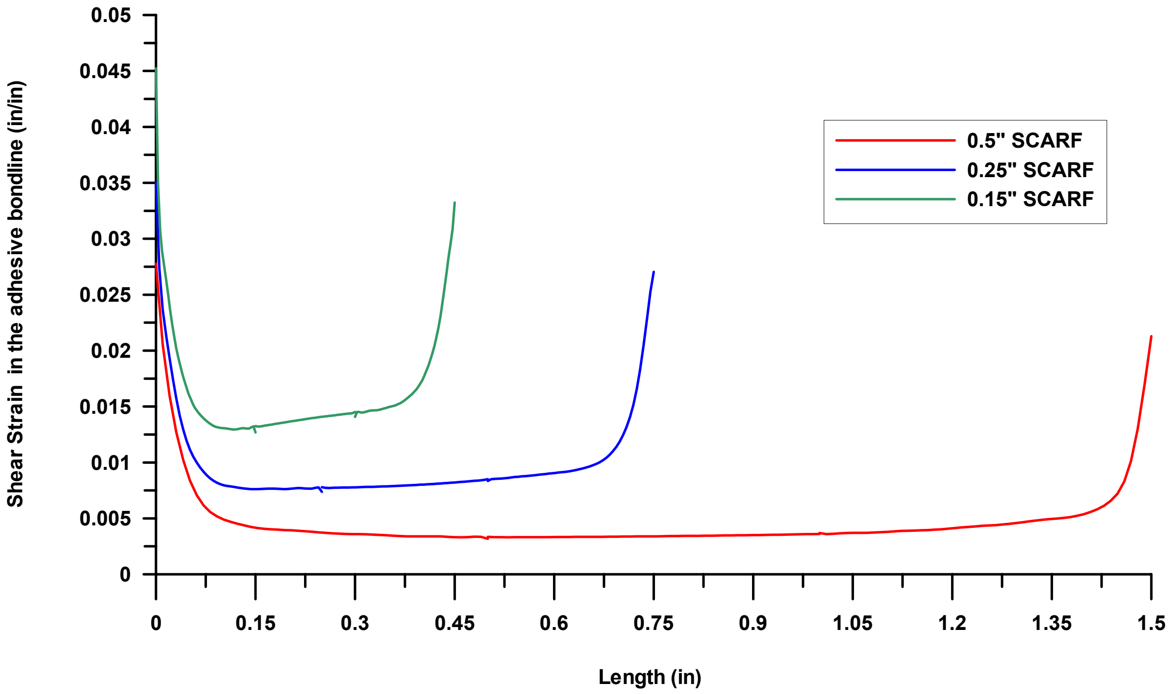

FIGURE 105. SHEAR STRAIN IN THE ADHESIVE BONDLINE FOR DIFFERENT SCARF REPAIRS ON THE 3/8-inch CORE SMALL FOUR-POINT BENDING BEAMS (WET LAY-UP REPAIR)

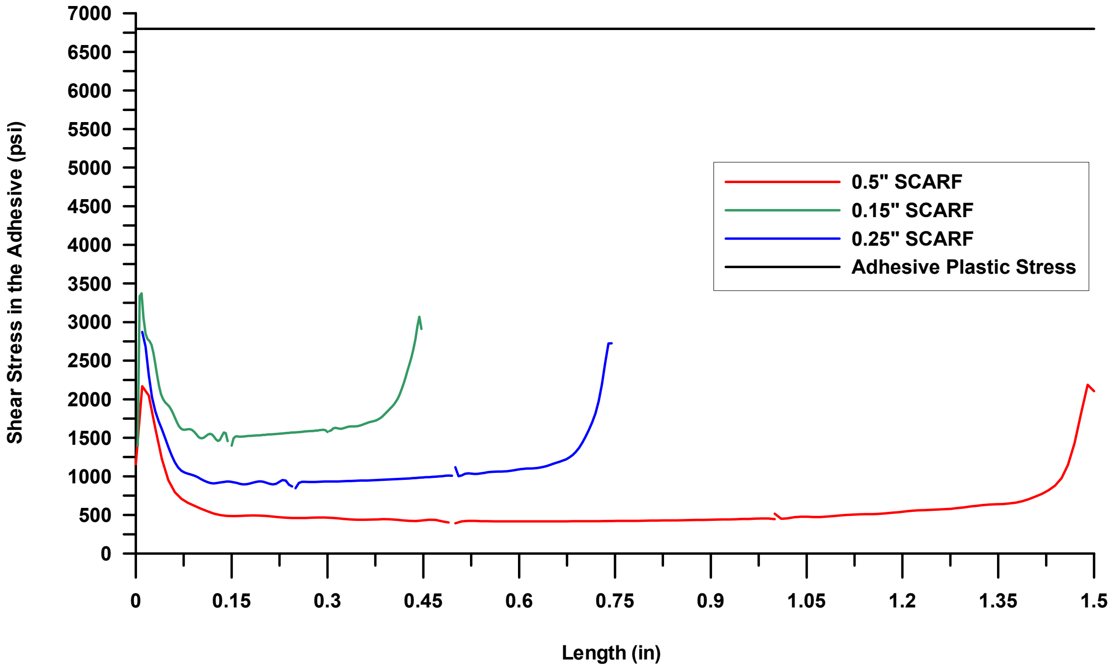

FIGURE 106. SHEAR STRESS IN THE ADHESIVE BONDLINE FOR DIFFERENT SCARF REPAIRS ON THE 3/8-inch CORE SMALL FOUR-POINT BENDING BEAMS (WET LAY-UP REPAIR)

5. CONCLUSIONS.

With the increasing usage of fiber-reinforced composites in aircraft structures, it has become necessary to establish reliable repair methods that will restore the structure's integrity. The purpose of this document was to investigate the effects of several bonded repair variables on the performance of sandwich structures.

The first task was to compare the performance of original equipment manufacturer versus field station repairs. The main goal was to compare two different repair methods, assess the repeatability of these repairs, and investigate the performance of different tools used in the field for nondestructive inspection. The second task was to evaluate the effects of different variables on the repair performance. Variables investigated included three different scarf overlaps, two different core cell sizes (1/8 and 3/8 inch), one- and two-dimensional repairs, three different loading modes, impact damage, and finally different repair materials and cure temperatures. The third task consisted of reviewing all the repair analytical models found in the literature and establishing a comparison between some of the model results and the experimental data.

For task one, all the repaired shear elements achieved at least 92% of the average pristine strength, regardless of the repair method used, except shear elements from one airline depot that seemed to have been poorly bonded. Furthermore, all the methods used for nondestructive inspection underestimated the size of the damage, with the manual tap hammer being the least accurate and the mechanical impedance analysis being the most accurate.

For task two, the core cell size had a major impact on the structural performance of a repaired sandwich structure. It was found that regardless of material or scarf overlap, the 1/8-inch core coupons performed better than the 3/8-inch core coupons. For the large four-point bending beams with a 1/8-inch core, there was no variation in strength and strain capacity as a function of increasing scarf overlap. However, damage in the taper repair area decreased the strength and strain capacity of the short overlap coupons.

For the undamaged large four-point bending beams with a 3/8-inch core, a decrease in strength and strain capacity was recorded for the 0.50-inch scarf repairs compared to the 0.15- and the 0.25-inch repairs. The damaged coupons exhibited the same trend with respect to scarf ratio. Damage in the taper repair area decreased the strength and strain capacity of these coupons.

For the small four-point bending beams, there was no change in strength or strain capacity as the scarf overlap was changed. This was found for both repair systems.

For 1/8-inch core unidirectional tension coupons repaired with Fibercote E765 carbon prepreg using the SIA 795-1 film adhesive system, results showed an increase in the strength and strain capacity as the repair scarf overlap was increased from 0.15 to 0.25 inch. Using a larger size repair did not provide an increase in the structural capability. For the 3/8-inch core coupons, data showed no structural improvement or deterioration as the scarf angle was increased.

For the 1/8- and 3/8-inch core unidirectional tension coupons repaired using Cytec BMS9-8, 3K-70-PW cloth with the EA9696 adhesive system, it was found that the 0.15-inch scarf repairs yielded the highest failure loads, whereas the 0.25- and 0.50-inch scarf repairs yielded almost identical average failure loads of approximately 12,000 lbf.

For the third task, laminate models were evaluated for coupons that failed in the facesheet, while adhesive models were used for coupons that failed in the adhesive. The Delta Design Spreadsheet applied to the 1/8-inch core large four-point bending coupons yielded very accurate failure loads with a percent error of less than 5%, while the Ten Percent Rule and the Commercial Aircraft Composite Repair Committee (CACRC)-improved solution overpredicted those values.

For the unidirectional tension coupons repaired with the prepreg material system, the Ten Percent Rule yielded the most accurate values for both core cell sizes evaluated. The CACRC-improved solution and the Delta Design Spreadsheet overpredicted the failure loads of the 3/8-inch core coupons by 14% and underpredicted the failure loads of the 1/8-inch coupons by 22%.

For the unidirectional tension coupons repaired with the wet lay-up material system, all laminate models overpredicted the strength with the CACRC-improved solution being the least accurate. For the small beams repaired with the wet lay-up system, the Delta Design Spreadsheet underpredicted the strength by, at most, 25%, while the Ten Percent Rule and the CACRC-improved solution overpredicted the strength of the beams by, at most, 20% and 38% respectively.

For the unidirectional tension coupons regardless of the repair system, failure strains predicted by SUBLAM compared to the experimental data and ultimate strains of the repair laminate material were conservative. These values reached at least the minimum strains obtained experimentally. SUBLAM results for the small beams were also very conservative but were far below experimental results.

For the coupons that failed in the bondline, adhesive models showed a positive strength margin with respect to laminate strength, which excludes the possibility of an adhesive failure. These coupons had a 3/8-inch core with a smaller bond interface area due to the large core cell size; therefore, the amount of peel stresses was higher, causing the failure to initiate in the adhesive.

This project demonstrated the influence of several factors on the performance of sandwich structure repairs. The most prominent conclusion that could be deduced from this study was the major impact that core properties, more specifically the core cell size, have on the performance of a sandwich structure with the same parent and repair materials. The results showed a superior strain and strength capacity for the 1/8-inch core coupons compared to the 3/8-inch core coupons, regardless of the repair size. The 1/8-inch core coupons offered a larger bond interface area than the 3/8-inch core coupons and, therefore, a higher strain capacity, assuming the same facesheets were used. It was also found that the 0.25-inch scarf overlap offered comparable results as the 0.50-inch scarf overlap; therefore, a smaller step overlap could be used to replace the widely used 0.50-inch step overlap.

Finally, since all the data obtained was based on static tests, fatigue tests must be performed in order to further corroborate static test results. Furthermore, all model results were a function of input data. Reliability of model predictions could be drastically improved by increasing the accuracy of the input data.

6. REFERENCES.

1. SAE International Commercial Aircraft Composite Repair Committee, *Design of Durable, Repairable and Maintainable Aircraft Composites*, Warrendale, Pa : Society of Automotive Engineers, 1997.

2. Cole, W.F., "Technical Justification of Repairs to Composite Laminates," *International Journal of Adhesion and Adhesives,* Vol. 19, 1999, pp. 107-120.

3. Hart-Smith, L.J., "An Engineer's Viewpoint on Design and Analysis of Aircraft Structural Joints," Douglas Paper MDC 91K0067, presented at *International Conference on Aircraft Damage and Repair*, Melbourne, Australia, 1991.

4. Baker, A.A., *Joining and Repair of Aircraft Composite Structures*, 1997.

5. Tomblin, J.S., Raju, K.S., Liew, J., and Smith, B.L., "Impact Damage Characterization and Damage Tolerance of Composite Sandwich Airframe Structures," FAA final report, DOT/FAA/AR-00/44, January 2001.

6. Aerospace Recommended Practice 5089, "Composite Repair NDT/NDI Handbook," SAE International.

7. Tomblin, J.S., Raju, K.S., Acosta, J.F., Smith, B.L., and Romine, N.A., "Impact Damage Characterization and Damage Tolerance of Composite Sandwich Airframe Structures–Phase II," FAA final report, DOT/FAA/AR-02/80, October 2002.

8. GOM Optical Measuring Techniques, "ARAMIS, Deformation Measurement System Using the Grating Method," 2001.

9. Welch, J.M., "Wichita Composite Structures Development," Proceedings of the *Forty-Fourth Composite Materials Handbook Coordination Group Meeting*, Miami, Florida, May 2002.

10. ASTM D 5656-01, "Standard Test Method for Thick-Adherend Metal Lap-Shear Joints for Determination of the Stress-Strain Behavior of Adhesives in Shear by Tension Loading."

11. Boyd, K.L. and Krishnan, S., "Evaluation of Aircraft Structural Repair/Analysis Codes," WL-TR-97-3052, November 1996.

12. Toru, I., Tadashi, T., and Shyunjiro, S., "Development of Scarf Joint Analysis Customized System (SJACS)," Proceedings of the *8th Japan-European Conference on Composite Materials*, pp. 1-8.

13. K.R. Loss and K.T. Kedward, "Modeling and Analysis of Peel and Shear Stresses in Adhesively Bonded Joints," *AIAA*, Paper 84-0913.

14. Hart-Smith, L.J., "Adhesive Bonded Scarf and Stepped Lap-Joints," NASA-CR-112237, January 1973.

15. Flanagan, Gerry, "A General Sublaminate Analysis Method for Determining Strain Energy Release Rates in Composites," Materials Science Corporation, Fort Washington, PA, 19034.

16. CACRC Repair Techniques, "Laminate Analysis Techniques," Rough Draft, May 2002.

17. Mallick, P.K., *Fiber-Reinforced Composites*, second edition, 1993.

18. Hart-Smith, L.J., "The Ten Percent Rule for Preliminary Sizing of Fibrous Composite Structures," McDonnell Douglas Paper MDC 97K0024, *Aerospace Materials*, Vol. 5, No. 2, August-October 1993, pp. 10-16.

19. Hart-Smith, L.J., "Expanding the Capabilities of the Ten Percent Rule for Predicting the Strength of Fibre-Polymer Composites," McDonnell Douglas Paper MDC 97K0012, *Composites Science and Technology*, 2002, pp. 1515-1544.

20. Reddy, M.N. and Sinha P.K., "Stresses in Adhesive Bonded Joints for Composites," *Fiber Science and Technology*, Vol. 8, 1975.

21. Sinha, P.K. and Reddy, M.N., "Thermal Analysis of Composite Bonded Joints," *Fiber Science and Technology*, Vol. 9, 1976, p. 153.

22. Grant, P.J., "Analysis of Adhesive Stresses in Bonded Joints," *Symposium on Joining in Fiber Reinforced Plastics*, Imperial College, 1978.

23. Baker, A.A. and Jones R., *Bonded Repair of Aircraft Structures*, 1988.

24. Byron Pipes, R. and Adkins, W., "Strength and Mechanics of Bonded Scarf Joints for Repair of Composite Materials," NASA-CR-169708 Final Report, May 1982.

25. Reinhart, J.T., *Engineered Materials Handbook*, Volume 3, Adhesives and Sealants, ASM International Handbook Committee, December 1990.

APPENDIX A—WET LAY-UP REPAIR PROCEDURE

1. *This step was essentially completed in Phase I of this program.* Determine the extent of the damage by tap testing per ARP 5089. Tap testing should be performed at least three times and the extent of the damage should be marked each time on the laminate. Take a photograph of the composite part, including a 6-inch scale for reference. Use digital photographs preferably, with moderate or low resolutions, to easily incorporate into e-reports.

2. Remove the damaged facesheet and the underlying core to a diameter of 4 inches and scarf sand per AIR 5367 section 5.1 using a 1/2-inch ±1/4-inch per ply overlap. Before removing the core, identify the core ribbon direction and mark the panel accordingly. Take a photograph. Start sanding with 120-grit abrasive paper and finish with 180-grit abrasive paper.

3. Clean per ARP 4916 Method 5, section 12.5, using isopropyl alcohol and cheesecloth or other wiping media that will not leave a residue. The wiping media is preferred not to leave in filament materials and shall contain no silicon, Teflon, or other well-known nonbond sizing or materials. AMS 3819 type 1 grade A wipers are recommended. No core cleaning is required.

4. Perform the water break-free test after cleaning, using ARP 4916 section 14.1.2.

5. Dry per ARP 4977 method 5 at 150° to 170°F for at least 2 hours. This will remove standing moisture that may have been introduced during the water break-free test, inspection, or shipping.

6. Restore core per ARP 4991 method 2, section 5.3.6. Use Epocast 52 A/B to bond core to existing skin and core. Insert the core plug into the hole in the panel such that the ribbon direction of the plug is correctly aligned with the ribbon direction of the existing core. Apply Epocast 52 A/B evenly in the core plug-existing core interface until it is entirely filled with material. Take a picture of the core plug that shows the ribbon direction with respect to the panel. Prepare vacuum bags on the damaged and undamaged sides of the panel centered on the repair area or envelope bag the entire panel. Apply vacuum on both sides of the panel and oven cure core plug to the following cure cycle, with vacuum applied: ramp up at 1-5°F per minute and hold at 270°F for 120 minutes, ramp down at 1°-10°F per minute. Remove vacuum bags and inspect core splice bondline. Another option would be to use a double-sided heat blanket to cure the core plug.

7. Inspect core-to-nondamaged facing using applicable NDI (per tap test). Additionally, visual inspection is possible by looking down through the core cells with a flashlight to see that the core is properly bonded to the existing skin.

8. Dress core splice bondline with the Epocast 52 A/B in areas that are not filled completely and let cure. Cure may be accelerated by using a standard heat gun applied to the area for 5-7 minutes to get the catalyst activated.

9. Mix the resin per ARP 5256. The mix ratio for the Epocast 52 A/B is as follows: to 100 parts by weight of Epocast 52-A, add 41 parts by weight of Epocast 52-B. Mix both components for several minutes until a homogeneous mixture is obtained. Note: only mix the amount that can be used within 40 minutes.

10 Impregnate the repair plies and apply per ARP 5319 section 3.2, using Epocast 52 A/B resin per AMS 2980/4 and TENEX HTA5131200TEXF3000 fiber per AMS 2980/3. Match the parent laminate ply orientations and add one ply in the dominant direction. The layup for the repair patch is as follows:

Ply 1: [0/90] – this ply goes against the core
Ply 2: [0/90]
Ply 3: [±45]
Ply 4: [0/90] – dominant direction – this is the extra ply

Use the Vertical Bleed Technique per ARP 5319 section 3.2. Please take a digital photograph after the lay-up of each ply.

11. Use the envelope bag method, vertical bleed per ARP 5143. Double-sided heat blanket or oven heating is acceptable. Surface bagging, vertical bleed is another option. In this case, a single-sided heat blanket is required. Please take a photograph of the complete bag and thermocouple placement.

12. Apply heat and cure per ARP 5144. Heat blanket or oven heating is acceptable. The following cure cycle is recommended: 1°-5°F/minute ramp up to 200° ±9°F, hold for 120 minutes, ramp down 1°-5°F/minute. Please take a photograph and keep the records of the cure and forward to Dr. John Tomblin at the following address:

Dr. John Tomblin
NIAR Composites Laboratory
1845 Fairmount
Wichita KS 67206-0093
Phone: (316) 978-5234
e-mail: John.Tomblin@wichita.edu

13. Reinspect by tap testing per ARP 5089. Provide your results with the panel shipment.

14. Package and ship specimens in the boxes in which the panels were sent to Dr. John Tomblin at the address specified in step 12.